Direct Pore Level Simulation of Heat Transfer in Open Cell Reticulated Porous Ceramics

zur Erlangung des akademischen Grades eines

DOKTORS DER INGENIEURWISSENSCHAFTEN
(Dr.-Ing.)

der Fakultät für Chemieingenieurwesen und Verfahrenstechnik des
Karlsruher Institut für Technologie (KIT)

genehmigte

DISSERTATION

von

M. Tech. Parthasarathy Pandi

aus Coimbatore/Indien

Referent:	Prof. Dr.-Ing. Nikolaos Zarzalis
Korreferent:	Prof. Dr.-Ing. Manfred Aigner
Tag der mündlichen Prüfung:	11.03.2016

Abstract

The phenomena of heat and mass transport in porous media have significant influence in wide range of engineering disciplines such as, solar energy, chemical, biological, material science, etc. The porous media are heterogeneous system consisting of solid matrix with several interconnected continuous void space (pores) filled with fluids. The project involved in studying the fluid transport, heat and mass transport inside various ceramic porous inserts by Direct Pore Level Simulations (DPLS). The geometric grid data required for the simulations are reconstructed from the computer tomographic scan images of the real porous media. The simulation results are used to study the influence of the structural properties of porous media on the fluid flow, heat transfer and mass transfer. The flow properties such as permeability and Dupuit-Forchheimer coefficient are obtained for different porous structures. The influence of tortuosity on the pressure drop is investigated. The effect of dispersion on mass transfer is evaluated by determining the axial mass dispersion coefficient. The use of the Peclet number to describe the relative importance of molecular diffusion and hydrodynamic dispersion in spreading the tracer fluid within porous structures is studied. The heat transfer properties such as heat conductivity and interface heat transfer coefficient are determined. A correlation for the heat transfer coefficients of the studied porous media is provided with the help of generalized Lévêque equation. Apart from DPLS, an in-house ray tracing code is used to identify the radiation properties such as extinction coefficient, absorption coefficient and the scattering phase function. Correlations to calculate the extinction coefficients in terms of the porous media structural parameters are provided.

Zusammenfassung

Wärme und Stofftransport in porösen Medien spielen in einem breiten Spektrum von technischen Anwendungsgebieten wie der Nutzung von Sonnenenergie, chemischer, biologischer und materialtechnischer Wissenschaft eine große Rolle. Poröse Medien sind heterogene Systeme, die aus einer festen Matrix mit vielen untereinander verbundenen Hohlräumen (Poren) bestehen in denen ein Fluid strömen kann. Gegenstand der Untersuchungen dieser Arbeit sind die Strömung und der Wärme- und Stofftransport in verschiedenen porösen, keramischen Medien durch direkte Simulation auf Porenebene (direct pore level simulation, DPLS). Die Geometriedaten und das CFD-Netz, das für solche Simulationen erforderlich ist, wurden durch Rekonstruktion aus computertomografisch erzeugten Bilddaten realer poröser Medien gewonnen. Die dabei erlangten Simulationsergebnisse werden dazu verwendet den Einfluss von Strukturparametern der porösen Medien auf Strömung sowie Wärme- und Stoffübertragung zu untersuchen. Strömungsparameter wie Permeabilität und Dupuit-Forchheimer-Koeffizient wurden für verschiedene poröse Strukturen bestimmt. Der Einfluss der Strömungstortuosität auf den Druckverlust wurde untersucht und als Ergebnis ein mathematischer Ausdruck für die Berechnung des Druckverlusts in porösen Medien erstellt. Die Auswirkung von Dispersion auf den Stoffübergang wurde in Form des axialen Stoffdispersionskoeffizienten bestimmt. Die Anwendbarkeit der Peclet Zahl zur Beschreibung der relativen Bedeutung der molekularen Diffusion und hydrodynamischer Dispersion für die Ausbreitung eines Tracerfluides innerhalb poröser Strukturen wurde untersucht. Größen zur Beschreibung der Wärmeübertragung, wie Wärmeleitfähigkeit und Wärmeübergangsko-

effizient wurden bestimmt. Eine Korrelation zwischen den Wärmeübergangskoefizienten der untersuchten porösen Medien wurde auf Basis der generalisierten Lévêque Gleichung formuliert. Abgesehen von den DPLS wurde ein hauseigenes Strahlverfolgungsprogramm verwendet um Strahlungseigenschaften wie den Extinktionskoeffizienten oder die Streuphasenfunktion zu bestimmen. Als Ergebnis werden Ausdrücke zur Bestimmung der Extinktionskoeffizienten als Funktion der Strukturparameter der porösen Materialien gezeigt.

Preface

This work was performed at the Engler-Bunte-Institute, Division for Combustion Technology (EBI-VBT) at the Karlsruhe Institute of Technology (KIT). I would like to express my sincere gratitude and thanks to Prof. Dr. -Ing. Nikolaos Zarzalis for providing this opportunity, excellent creative environment, encouragement, funding, international contacts and a strategic project planning that has enabled me to carry out this work. His steady trust and optimism is one of the main reasons for the successful completion of this work. I am also grateful for the numerous publications for conferences and journals to present the joint work, which enlarges my experiences substantially. I would like to thank the co-referee Prof. Dr. -Ing. Manfred Aigner, for his interest in my work.

I wish to thank the present and former members of EBI-VBT for their friendship, contributions and for providing an open and pleasant atmosphere at the institute. Especially I am very much grateful to the current leader of the theory group Dr. -Ing. Peter Habisreuther for his continuous support and enthusiastic involvement in this research. I like to extend my sincere thanks to the IT administrator Mr. Walter Pfeffinger for his professional help. I also like to thank all the administrative staff and secretaries for their support and kindness. The author gratefully acknowledge the financial support by the German Research Council (DFG) through the Research Unit FOR 583 "Solid Sponges-Application of Monolithic Network Structures in Process Engineering". Also the colleagues from the research initiative deserve my gratitude for many productive meetings and evenings.

Last but not least I want to thank my father Pandi, my mother Lakshmi, my brother Padmanabhan and my wife Archana for providing continuous support and freedom, which finally made this work possible.

Parthasarathy Pandi
Stuttgart
11.03.2016

Contents

Nomenclature

Roman	units	
A	m^2	area
A_o	m^2	outer surface area
c_e	-	cumulative probability distribution function of extinction of a continuous media
c_F	-	drag constant
c_p	J $kg^{-1}K^{-1}$	specific heat capacity
C_e	-	cumulative probability distribution function of extinction in local scale
d	m	diameter
d_h	m	hydraulic diameter
d_p	m	particle or strut diameter
d_{pore}	m	pore diameter
D	m^2 s^{-1}	dispersion tensor
D_e	m	equivalent diameter
D_L	m^2 s^{-1}	axial dispersion coefficient
D_m	m^2 s^{-1}	molecular diffusion coefficient
f	-	friction factor
f_a	-	absorption probability density function of a continuous media
f_e	-	extinction probability density function of a continuous media
f_{tube}	-	tube friction factor

Roman	units	
F	-	probability density function
F_a	-	absorption probability density function in local scale
F_e	-	extinction probability density function in local scale
h, h_{fs}, h_{sf}	W m^{-2} K^{-1}	heat transfer coefficient
k_1, k_2	W m^{-1} K^{-1}	thermal conductivity
k_{eff}	W m^{-1} K^{-1}	effective solid thermal conductivity
$k_{eff(2phase)}$	W m^{-1} K^{-1}	two phase effective thermal conductivity
k_f	W m^{-1} K^{-1}	fluid thermal conductivity
k_K	-	Kozeny constant
k_s	W m^{-1} K^{-1}	solid thermal conductivity
K	m^2	permeability
l_b	m	characteristic length associated with the pore space in the fluid-solid system
l_l	m	axial random mixing length scale
l_r	m	radial random mixing length scale
L	m	path length
L^+	-	normalized path length
$\dot{m}$	kg s^{-1}	mass flow rate
$\hat{n}$	-	normal vector
N_{ray}	-	number of rays
Nu	-	Nusselts number
p	N m^{-2}	pressure
p_a	-	probability of absorbtion of a continuous media
p_e	-	probability of extinction of a continuous media
P_a	-	probability of absorbtion in local scale
P_e	-	probability of extinction in local scale
Pe_L	-	Peclet number ($= ud/D_L$)
Pe_m	-	Peclet number ($= ud/D_m$)
Pe_p	-	Peclet number ($= ud_p/D_m$)
Pr	-	Prandtl number

Roman	units	
$\dot{Q}$	$m^3\ s^{-1}$	discharge
r	m	radius
R	$m^2\ K\ W^{-1}$	thermal resistance
Re_p	-	particle Reynolds number
S_v	m^{-1}	specific surface area
t	s	time
T	K	temperature
T_f	K	fluid temperature
T_s	K	solid temperature
u	$m\ s^{-1}$	internal bulk velocity $[= \dot{m}/A\rho]$
u_i	$m\ s^{-1}$	intrinsic velocity
u_s	$m\ s^{-1}$	superficial velocity
u'	$m\ s^{-1}$	velocity fluctuation
V	m^3	volume
V_f	m^3	void volume
V_s	m^3	strut volume
V_t	m^3	total volume
x	-	cartesian coordinate direction
y	-	cartesian coordinate direction
z	-	cartesian coordinate direction
$\overline{x_{sim}}$	m	mean distance
Y	$kg\ kg^{-1}$	mass fraction
$\overline{Y}$	$kg\ kg^{-1}$	mass flow averaged mass fraction

Greek	units	
α	-	hemispherical absorptance
α'	-	directional hemispherical absorptance
α_d	-	diffuse hemispherical absorptance
β	m^{-1}	equivalent extinction coefficient
β_x	m^{-1}	equivalent extinction coefficient in x direction
β_y	m^{-1}	equivalent extinction coefficient in y direction
β_z	m^{-1}	equivalent extinction coefficient in z direction

Greek	units	
δ	-	Dirac delta function
ε	-	porosity
θ_i	rad	angle of incidence
θ_r	rad	angle of reflection
κ	m^{-1}	absorption coefficient
μ	N s m^{-2}	dynamic viscosity
μ_i	-	cosine of incident angle
μ_r	-	cosine of reflection angle
μ_s	-	cosine of scattering angle
ρ	kg m^{-3}	fluid density
ρ'	-	hemispherical directional reflectance
ρ''	-	bidirectional reflectance
τ	-	tortuosity factor
τ_s	-	solid tortuosity factor
σ^2	-	variance
φ_i	rad	azimuth angles of incident
φ_r	rad	azimuth angles of reflection
Φ	-	scattering phase function

Abbreviations	
CFD	computational fluid dynamics
CT	computer tomography
DPLS	direct pore level simulation
IOOS	identical overlapping opaque spheres
IOTS	identical overlapping transparent spheres
LB	lattice Boltzmann
MRI	magnetic resonance imaging
NMR	nuclear magnetic resonance
OK	ordered Kelvin
PIM	porous inert media
PPI	pores per inch
REV	representative elementary volume
RMS	root mean square
RMSD	root mean square deviation

List of Figures

Chapter 1

Introduction

The phenomena of heat and mass transport in porous media have significant influence in wide range of disciplines such as chemical engineering, biological engineering, material science, etc. The porous media are heterogeneous system consisting of solid matrix with several interconnected continuous void space (pores) filled with fluids. Within the pores the conservation equations are valid and can be used to describe the heat and mass flow within it. The difficulty in describing the exact geometry of the bounding solid surfaces and the requirement of high computational capacity to solve the conservation equations within the pores gave rise to a macroscopic continuum approach which is used to describe the transport process within Porous Inert Media (PIM). The influence of the solid matrix on the transport process within the pores is described by effective transport properties. The accuracy in determining the effective transport properties of the porous media influences the overall accuracy of continuum approach.

Majority of studies on transport phenomena in porous media were performed considering packed bed kind of porous media. The emergence of Reticulated Porous Ceramics (RPC) as an alternative to the packed beds in various engineering applications, unfold the importance of studying the heat and mass transfer in these RPC structures. Typically, in engineering applications the porous domain is much larger than the pore size, and the conservation equations are solved using

continuum models [9, 68]. In the continuum models, the influence of the material and the structural properties on the transport phenomena is defined by the effective transport properties [9, 68]. In the case of engineering applications involving high temperature, such as porous burners, the accurate prediction of heat and species transport within porous inert media plays an important role in designing and optimization of such porous media combustors. The effective transport properties are determined either by using an approximate analytical approach or by experiments. The analytical approaches have a great deal of inaccuracy due to the geometric simplification, and the experimental measurements are tedious and prone to measurement uncertainties and errors.

A new method to analyze the flow in open-cell foams is given by the rise in computational speed, which makes it possible to calculate the heat and mass transport within these structures even with conventional CFD methods. This work involved studying the fluid transport and the heat transport inside various ceramic porous inserts by Direct Pore Level Simulations (DPLS). The geometric computational volumes required for the simulations are reconstructed from the computer tomographic scan images of the real porous media. The simulation results are used to study the influence of the structural properties and material properties of porous media on fluid flow and heat transfer.

1.1 Objectives

The main objective of this work is to calculate the effective transport properties of reticulated porous inert media by direct pore level simulations and correlate the properties to the structural parameters, such as porosity, pore density, specific surface area and pore diameter. The reticulated porous ceramics made of two different ceramic materials, namely, silicon infiltrated silicon carbide (SiSiC) and alumina (Al_2O_3) are studied. The above mentioned materials are predominately used in porous media combustors and in solar reactors. The ceramic sponges having different structural parameters are investigated.

X-Ray based Computed Tomographic (μ-CT) imaging and Magnetic Resonance Imaging (MRI) are used to generate the tomographic scan images of the SiSiC and Al_2O_3 RPC, respectively. The geometric

computational volumes required for the direct pore level simulations are reconstructed from the tomographic scan images of the above mentioned RPC. The flow properties such as permeability and drag coefficient are obtained for different porous structures, the heat transfer properties such as heat conductivity and interface heat transfer coefficient are determined. The effect of axial dispersion in flow is evaluated by determining the axial dispersion coefficients. Apart from DPLS, an in-house ray tracing code is used to identify the radiation properties such as extinction coefficient, absorption coefficient and the scattering phase function. The influence of the porous media's structure and material on the transport process within the RPC is investigated using the determined effective properties.

1.2 Outline

Chapter 2 provides a description about the volume imaging process that was used in this study to reconstruct computational volumes. The methods used to determine the sponge properties such as porosity, pore diameter and specific surface area of the sponges are discussed. Introduction to the method of volume averaging in porous media is given, and finally, the process of identifying the representative elementary volume size for a sponge is discussed.

In Chapter 3, a review of the pressure drop in porous media is documented. Discussion on the direct pore simulations to evaluate the pressure drop in each sponge considering air as the fluid medium is provided. Methodology used in determining the Ergun constants using the simulation results is discussed.

Chapter 4 deals with the axial dispersion in the ceramic sponges. Discussion about the use of the Peclet number to describe the relative importance of molecular diffusion and hydrodynamic dispersion in spreading the tracer fluid is provided.

In Chapter 5, information about the study on conduction and convective heat transport in the ceramic sponges is given. The methodology used in determining the heat transfer coefficient and effective conductivity of the sponges is described.

Chapter 6 provides insight into the methodology used in identifying the radiative properties of the ceramic sponges. The influence of sponge

properties on the effective radiative properties is discussed.

Finally, a conclusion regarding this study on heat and fluid flow in reticulated ceramic sponges is provided in Chapter 7.

Chapter 2

Morphology of reticulated porous ceramics

High porosity reticulated structures are widely used in many industrials applications such as solar reactors[45], radiant burners & combustors [32], solar receivers [42], gas filtering [107] etc. In literature, these structures are typically named as foams. But, as a foam is defined consisting of closed bubbles, its void phase is not continuous but dispersed (Reitzmann et al. [99]). Therefore, the explicit term sponge is used in the present work, having in focus particularly ceramic sponges. The reticulated sponge structures are associated with very high porosity, and thus provide comparatively less pressure drop in comparison to the packed beds, while still providing more mixing or dispersion compared to the honeycomb type structures. These structures have high specific surface area, and as both the fluid and the solid phase are continuous, these structures are being widely used in many heat transfer applications in recent years. The sponge manufacturing process has reached a level where it is now consistent enough that the reticulated structures are widely used in many industrial applications. The properties of these cellular structures can be modified to suit a wide range of new applications such as light weight construction, sound and heat insulation etc. In this study, alumina sponges made of 99% pure Al_2O_3 and SiSiC ceramic sponges are investigated. Photographs of alumina and SiSiC

sponge samples of pore densities 10 PPI and 20 PPI are shown in Figure 2.1.

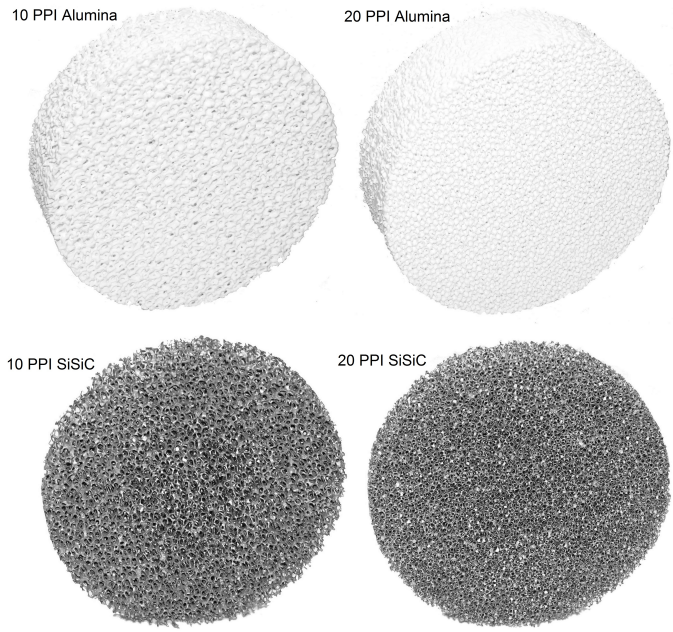

Figure 2.1: Photograph of alumina and SiSiC sponges of pore densities 10 and 20 PPI.

The alumina sponges of porosities between 75% to 85%, with pore densities 10, 20, 30 and 45 PPI are manufactured by Vesuvius Becker & Piscantor, Grossalmeroder Schmelztiegelwerke, Germany. The SiSiC sponges of 85% nominal porosity and pore densities of 10 and 20 PPI are manufactured by Erbicol SA, Switzerland. Both sponges are produced by the Schwartzwalder process, in which the reticulated polymers (Polyurethane) are coated with the suspension of ceramic and then the coated structure is sintered to remove the polymers [105]. After sintering the final sponge struts have inner cavities due to the polymer precursor. The presence of hollow cavities in the strut of a 10 PPI alumina sponge is shown in Figure 2.2. In the case of SiSiC sponge,

after sintering the sponge cavities are infiltrated with silicon so that the voids in the strut are filled. Apart from the real structures, theoretical Kelvin structures developed by Habisreuther et al. [52] containing cylindrical struts as shown in Figure 2.3 are also used in performing the pore level simulations. In the study of pressure drop, axial dispersion and effective conductivity in ceramic structures, the results from such theoretical structures are used as reference to compare them with that of the real structures.

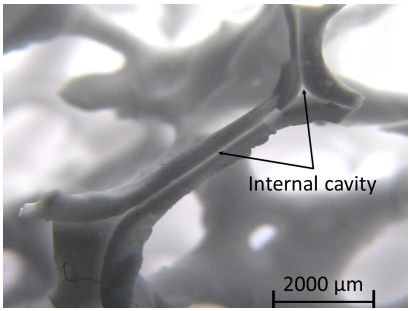

Figure 2.2: Microscopic view of a cut on the surface of 10 PPI alumina sponge to illustrate the presence of hollow cavities in the solid strut.

Evaluating the exact geometric properties of the sponges is of great importance in order to calculate and correlate the fluid flow and heat transfer in the sponges. Important geometric data includes the equivalent hydraulic diameter, pore diameter, specific surface area etc. In this study, volume imaging method is applied to determine the structural properties such as the specific surface area, pore diameter and porosity. The volume imaging method to determine such geocentric properties was used by various researchers in recent years [51, 85, 114]. X-ray absorption tomography is the most commonly used technique for three dimensional imaging and to determine the sponge structural properties [85, 114], while Grosse et al. [51] used magnetic resonance imaging (MRI) to characterise the ceramic sponges. In comparison to the X-ray absorption tomography, the MRI have limited resolution, although it still is an adequate method for three dimensional imaging of sponges [51].

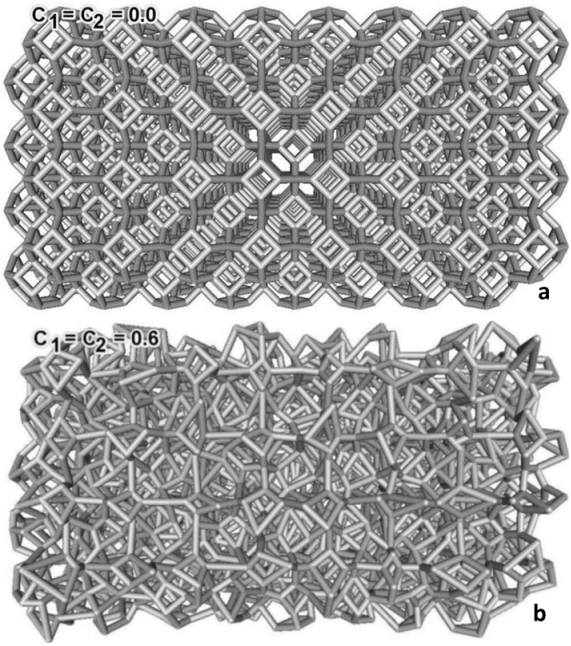

Figure 2.3: A view of ordered Kelvin structure (a) with randomization factors $C_1 = C_2 = 0$ and randomized Kelvin structure (b) with randomization factors $C_1 = C_2 = 0.6$.
Source: Habisreuther et al. [52]

In this work, the volume images of the alumina sponges are obtained using magnetic resonance imaging, and X-ray tomography is used in the case of SiSiC sponges. The MRI experiments were performed in the MRI-laboratory, Department of Chemical and Process Engineering at Karlsruhe institute of Technology. The image data acquisition were done with a Bruker Avance 200 SWB tomography. The MRI resolution depends on the sample size and on the number of voxels. In this case, 256×256×256 voxels were chosen in order to achieve reasonable acquisition time [51]. The resulting resolution was 86 μm for 10, 20, 30 PPI sponges, in which case the samples' size is 22×22×22 mm^3, and 50 μm for 45 PPI sponge of sample size 12.8×12.8×12.8 mm^3. The imaging process is explained in detail by Grosse et al. [51]. The X-ray

tomographic measurements were made in Department of Surface and Material Engineering at Aalen University. The imaging was done with phoenix v|tome|x s X-ray system of GE Sensing & Inspection Technologies. The resolutions of the X-ray imaging were set as 40 μm per voxel.

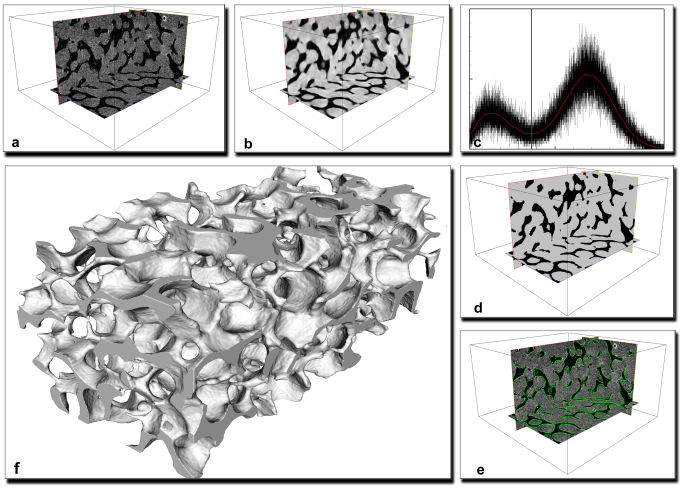

Figure 2.4: Reconstruction of triangulated iso-surface by means of digital image processing of a tomographic image: (a) raw tomographic image (b) median filtered image (c) gray scale value histogram(d) binarized image and (e) sponge surface (green).

Reconstruction of a solid surface is necessary in order to generate the discretized computational grid covering the void space and the solid strut volumes in the sponge. The solid surface was identified using the procedure shown in Figure 2.4, which results in a closed three-dimensional surface of the sponge discretized by triangular surfaces, as in Figure 2.4(f). A sample raw tomographic data is shown in Figure 2.4(a). The raw measurement data contains unwanted noise, the noise in the raw data has been reduced using a 3×3×3 median filter (Figure 2.4(b)). In order to make a distinction between the strut section and the void sections, a threshold value of the data had to be found to convert

the grayscale images into binary images representing the strut and void sections. The threshold values were chosen by locating local minima of the histogram curves of individual sponges as shown in Figure 2.4(c). Once the strut surface was identified using a threshold value, the binarization of the tomographic data was done. Finally, the surface data was exported to the commercially available computational grid generating software (ANSYS ICEM) to generate the required computational grids. The computational grids were produced requiring approximately 8 hours each on 2 Quad-core processors with 8 GB RAM. The resulting grids consisted of 4-6 million tetrahedral cells and approximately 0.8-1.1 million grid points.

2.1 Porous media characterization using tomography data

2.1.1 Porosity

Porosity ε of the porous media is the ratio of the empty void space V_f occupied in the media to the total volume V_t. Two types of porosities are generally defined for the sponge structures. The total porosity, in which case the void volume includes all kinds of void space, i.e., the macroscopic voids and the voids present in the struts after replication method. The other one being the open porosity, in which only the macroscopic void spaces are considered. In the case of SiSiC sponge the open and total porosities are nearly equal due to the infiltration of silicon after sintering process. The open porosities are more relevant in the study of fluid flow and heat transfer. In this study, only the open porosity is calculated. For the porous sponges used in this study, the void volumes were obtained from their respective computational grids by summation of all the tetrahedral volumes that occupy the void space. With the measured macroscopic void volume V_f, the porosities were calculated by dividing total empty space with the total volume of the porous mediums.

2.1.2 Pore diameter

Based on the detailed geometry of the samples, an estimation of the extents of single pores has been derived. The procedure starts with an estimation of points in the void phase that are assumed to be the pore centers. These points are determined by first calculating the Euclidean distance of every point in the void phase to the nearest surface point by application of the algorithm according to Saito and Toriwaki [104] and then searching local maxima in the 3-dimensional distance field. Twice of the local distance at these local maxima gives an estimation of a minimal pore diameter. The arithmetic average of these pore diameter values is considered as the pore diameter d_{pore} of the sponge. The pore size obtained for the sponge was used to find the pore density in terms of Pores Per Inch (PPI) using the relation $d_{pore} = 0.0508/PPI$ [53]. The measured pore diameters are tabulated in Table 2.1.

2.1.3 Specific surface area

Specific surface area S_v is the parameter that relates the strut outer surface area to the total volume of the sponge. In the case of fluid flow and heat transfer between the fluid and the strut, the specific surface area is an important dimensional parameter that can be used to compare such processes with that of other porous structure such as packed beds and honeycombs. It has been reported that the physisorption measurement of gases overestimate the surface area of the strut due to the presence of cavities in the solid struts [50]. The volume imaging method was used by Grosse et al. [50] to find the specific surface area of the sponges. In this study, after the sponge reconstruction, the surface area of the sponge is found by the summation of the triangular surface elements that defines the void and the strut boundary. The total surface area thus obtained is divided by the total volume of the sponge to determine the specific surface area (the total volume includes the void and the strut volume). In Table 2.1, the specific surface areas found using reconstructed sponges are provided for each sponge that is used in this study.

Table 2.1: Porosities, specific surface areas and pore diameters of sponges measured using volume image analysis

Sponge description	**Measured porosity [-]**	**Measured specific surface area [m^{-1}]**	**Measured pore diameter [m]**
Al_2O_3 10 PPI 80% porosity	0.82	577.5	0.00391
SiSiC 10 PPI 85% porosity	0.872	476.3	0.00451
Al_2O_3 20 PPI 75% porosity	0.769	1146.9	0.00201
Al_2O_3 20 PPI 80% porosity	0.82	900.9	0.00239
Al_2O_3 20 PPI 85% porosity	0.845	996.3	0.00209
SiSiC 20 PPI 85% porosity	0.875	647.2	0.00201
Al_2O_3 30 PPI 75% porosity	0.744	1336.8	0.00167
Al_2O_3 30 PPI 80% porosity	0.822	1264.9	0.00162
Al_2O_3 30 PPI 85% porosity	0.847	1214.6	0.00162
Al_2O_3 45 PPI 80% porosity	0.791	1610.1	0.00121

2.1.4 Representative elementary volume

2.1.4.1 Method of local volume averaging

The difficulty in describing accurately the geometry of the internal solid surface that bound the flow inside the porous media gave rise to the macroscopic approach of local volume averaging. This approach is similar to the continuum approach in fluid mechanics. In the contin-

uum approach, the problem of fluid motion is tackled with help of the statistically macroscopic approach instead of treating the problem at microscopic molecular level. The volume average method in porous media requires a much coarser level of treatment. This method involves in averaging the fluid continuum in the void spaces in the porous matrix. In the volume averaged method, the usual fluid continuum approach is considered microscopic. The elementary volume of study in the volume averaged method should be the smallest differential volume that results in statistically meaningful average properties.

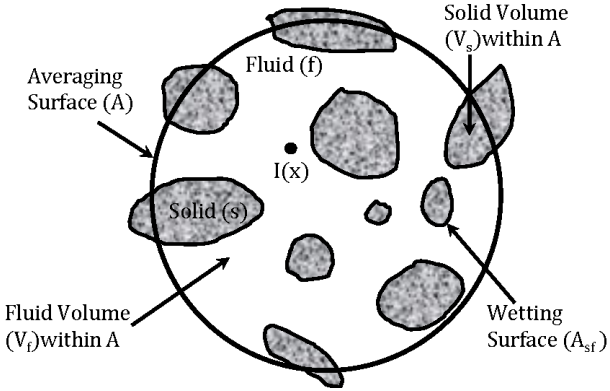

Figure 2.5: Schematic of representative elementary volume.

In a two phase system of volume V contained within the surface A as shown in Figure 2.5, let $I(x)$ be a volume element in the fluid phase. The volume V is occupied by both the fluid volume V_f and the solid volume V_s. The local porosity $\varepsilon(x)$ can be defined as:

$$\varepsilon(x) = \frac{1}{V} \int_V I(x) \mathrm{d}V \tag{2.1}$$

When the volume V is increased step by step, after some point any additional increase in the volume will not have an influence on the local properties such as porosity $\varepsilon(x)$. For this condition to be reached, the dimension L of the volume must be much larger than the pore diameter d_{pore} and must be smaller than the largest dimension of the

porous matrix L_{max}. This volume is termed as the Representative Elementary Volume (REV) of the porous matrix [9, 68]. The local volume average for any quantity ψ is defined as:

$$\bar{\psi} = \frac{1}{V} \int_V \psi \mathrm{d}V \tag{2.2}$$

If ψ is a fluid quantity,

$$\bar{\psi} = \frac{1}{V_f} \int_V \psi \mathrm{d}V \tag{2.3}$$

In order to solve the volume averaged transport equations, the effective transport properties of the sponges are required. The effective properties are usually found by conducting experiments with the real sponges. The increase in the computational speed and memory capacity provide a major breakthrough, now it is possible to calculate transport properties of the sponges with conventional computational fluid dynamics methods. The transport properties of the sponge depend on the transport properties of the individual sponge phases. If the geometries of the sponges are well defined in a pore scale, the direct pore level simulations (DPLS) can be performed to determine the effective transport properties. Many analytical approaches were used to determine the effective properties by simplifying the geometries, but such analysis are limited to the assumptions that were made in simplifying the structural geometry. The computational grids that are reconstructed using the tomographic scans provide the exact replicas of the sponges. The reconstructed computational grids are used in this study in determining the effective transport properties using DPLS.

2.1.4.2 Representative elementary volume of sponges

Before performing DPLS simulations within the reconstructed grids, it has to be examined whether each individual reconstructed grid geometry is larger than that of the representative elementary volume of the corresponding sponge. Representative elementary volume is the smallest possible volume of the sponge having specific properties as those of the whole reticulated structure. The REV is analogous to the minimum continuum volume defined in the case of a continuous fluid media.

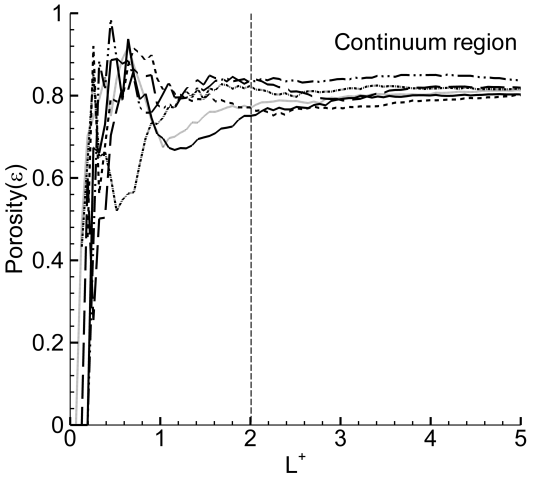

Figure 2.6: Variation in the porosity (ε) values with increase in normalized side length (L/d_{pore}), for six different locations within the 30 PPI 80% porosity Al_2O_3 porous structure.

Figure 2.6 describes the method used in identifying the REV of a 30 PPI 80% porosity Al_2O_3 sponge. For six different locations chosen within the sponge, the porosities were calculated with increase in side length L starting from 0, and were plotted against the normalized side length $(L^+ = L/d_{pore})$. As by the definition of the porosity, at a limiting case of $L = 0$, the porosity takes a value of 0 if the chosen starting point is on solid strut and takes a value of 1 if the point is on the fluid. From Figure 2.6, it can be seen that the fluctuations of the porosity value reduce as the side length increases, and from $L/d_{pore} = 2$, the fluctuations are within $\pm 7\%$ for all six chosen locations. The corresponding volume $\Delta V = 39$ mm^3 was taken as the representative elementary volume for 30 PPI 80% porosity Al_2O_3 sponge. This method was followed to determine the REV of all the porous mediums used in this study, and to check whether the sponge volumes are much larger than the minimum volumes (REVs), a condition that has to be satisfied to perform the direct pore level simulations.

Chapter 3

Fluid flow in reticulated ceramic sponges

Fluids flowing through porous media have an increased bulk flow resistance in comparison to fluids flowing through the ducts of similar dimension. The first measurement of the increase in resistance to the fluid flow in porous media was experimentally measured by Darcy [25]. For fluid flow within the porous media at low Reynolds numbers ($Re_p/(1-\varepsilon) < 10$, where $Re_p = \rho d_p u_s/\mu$ and d_p is the particle diameter), there is an increase in the stress resistance to fluid flow due to the increase in the solid surface area (wetting surface), where Re_p is calculated using the particle diameter as characteristic length. In Darcy's experiment, randomly packed isotropic porous bed made up of uniformly sized sand particles was used. The flow within the porous media was gravity driven, one dimensional steady flow. The schematic of Darcy's experiment is shown in Figure 3.1.

The experiment showed that the fluid discharge $\dot{Q}$ is a function of the flow area A, the difference in hydraulic head dh and the porous bed length dx.

$$\dot{Q} = -\kappa A \frac{\Delta h}{\Delta x} \tag{3.1}$$

where the proportionality constant κ in Eq. (3.1) is the hydraulic

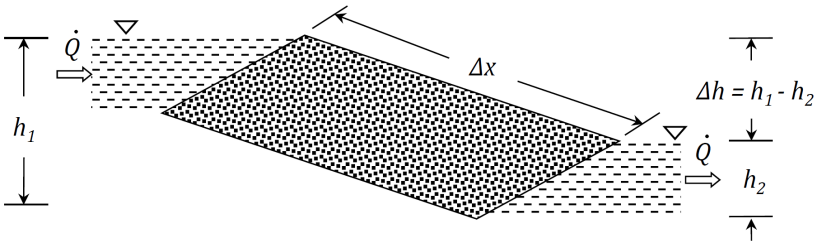

Figure 3.1: Schematic of Darcy's experiment on flow of water through sand.

conductivity with dimension [L/T].

The Darcy law can also be written in terms of the pressure gradient dp/dx and the superficial velocity u_s as in Eq. (3.2)]

$$\frac{\mathrm{d}p}{\mathrm{d}x} = -\frac{\mu}{K} u_s \tag{3.2}$$

where μ is the fluid dynamic viscosity and K is the permeability of the porous media with dimension [L^2]. The superficial velocity u_s is found by dividing the mass flow rate of the fluid $\dot{m}$ by total cross sectional area of the porous media channel A.

3.1 Low Reynolds number flows

Henry Darcy's experiments show that at very low velocities the pressure drop inside a porous domain is dependent on the geometry of the porous matrix. Permeability K is the measure of flow conductance of the porous matrix [68], i.e., permeability is the property of the porous matrix which measures its ability to allow fluid to flow through it. In the Darcy regime, the permeability describes the bulk hydrodynamic behavior of the fluid flow, it accounts for the influence of the structural properties of the porous media on the fluid flow. Due to the complex geometries of the porous structures, there are no universal correlations available for permeability in terms of porosity, wetting surface area, etc. A detailed review of the various models used in determining the permeability of simple porous structures was done by Kaviany [68].

3.1.1 Capillary models

These models are used for formulating the relationship between permeability and structural properties of simple porous matrix. The flow inside the porous structures is considered to be steady and fully developed. The Reynolds numbers in these models are very low so that the hydrodynamic entry length is assumed negligible. The models involve an application of Navier-Stokes equation to the fluid flow in small diameter channels. Based on the capillary model, for the flow that takes place inside an arrangement of parallel straight tubes of small diameters, the pressure drop is given by Hagen-Poiseuille equation

$$\frac{\mathrm{d}p}{\mathrm{d}x} = -\frac{128\mu}{n\pi d^4} u_s \tag{3.3}$$

where d is the channel diameter. From Eq. (3.3) the permeability can be identified as

$$K = \varepsilon d^2/32 \tag{3.4}$$

where $\varepsilon = n\pi d^2/4$. This is one of the simplest model for obtaining the permeability values, but mostly do not agree with porous matrix of complicated geometries.

3.1.2 Hydraulic radius model

In this model, the packed column is visualized as a bundle of tangled tubes of weird cross-sections [12]. The sphere packing is considered to be statistically uniform and so no frequent channelings occur, and the column diameter of the packed bed to be much larger than the particle diameter, so that the increase in local porosity and entrance effect is neglected [34]. The derivation outlined in Bird et al. [12] is as follows:

Friction factor f for packed bed column (analogues to the definition of friction factor for a flow through pipe) is

$$f = \frac{1}{4}\left(\frac{d_p}{L}\right)\left(\frac{\Delta p}{0.5\rho {u_i}^2}\right) \tag{3.5}$$

where $u_i = u_s/\varepsilon$ is the intrinsic velocity. The pressure drop through a

representative tube in a bundle is

$$\Delta p = \frac{1}{2}\rho {u_s}^2 \left(\frac{L}{r_h}\right) f_{tube} \tag{3.6}$$

from Eq. (3.5) and Eq. (3.6), the friction factor of packed bed is

$$f = \frac{1}{4\varepsilon^2}\left(\frac{d_p}{r_h}\right) f_{tube} \tag{3.7}$$

with hydraulic radius $r_h = d_p\varepsilon/6(1-\varepsilon)$, the friction factor for the packed beds is

$$f = \frac{3}{2}\left(\frac{1-\varepsilon}{\varepsilon^3}\right) f_{tube} \tag{3.8}$$

For laminar flows in tubes, the friction factor f_{tube} is $16/Re_h$, where Reynolds number $Re_h = 4r_h u_i \rho/\mu$. For tortuous paths and non-cylindrical surfaces, the friction factor value $16/Re_h$ of bundled tubes is replaced by $100/(3 \cdot Re_h)$, and the pressure drop through the packed beds is

$$\frac{\Delta p}{L} = 150\left(\frac{\mu u_s}{{d_p}^2}\right)\frac{1-\varepsilon^2}{\varepsilon^3} \tag{3.9}$$

Eq. (3.9) is knows as the Blake-Kozeny equation [13] and is valid for $Re_p/(1\text{-}\varepsilon) < 10$, where Re_p is the Reynolds number with particle diameter d_p as characteristic length. Carman [22] accounted for the increase in the average velocity due to the tortuous flow path within the channel and the coefficient 150 in Eq. (3.9) is replaced by 180. Eq. (3.10) is the Carman-Kozeny-Blake equation [22].

$$\frac{\Delta p}{L} = 180\left(\frac{\mu u_s}{{d_p}^2}\right)\frac{1-\varepsilon^2}{\varepsilon^3} \tag{3.10}$$

Then the permeability (K) is

$$K = \frac{\varepsilon^3 {d_p}^2}{180(1-\varepsilon)^2} \tag{3.11}$$

Eq. (3.11) is also written as

$$K = \frac{\varepsilon^3 {d_p}^2}{k_K(1-\varepsilon)^2} {S_{vs}}^2 \tag{3.12}$$

where $k_K = k_0\tau^2$ is the Kozeny constant and $S_{vs} = 6/d_p$ is the specific surface area based on the solid volume. For packed bed spheres the tortuosity τ is 1.4 [22, 34], k_0 is approximately equal to 2.5.

3.1.3 Drag models for isotropic structures

In these models the creeping flow over periodic structures of loosely packed sphere and cylinders are studied. The Navier-Stokes equation is solved for the flow over the objects and the drag created by the objects is compared with the Darcy flow resistance to obtain the permeability.

3.1.3.1 Creeping flow over cylinders

Happel and Brenner [56] analyzed the one dimensional parallel flow in an annulus bounded between a solid cylinder of diameter d and an outside cylinder of diameter $d+\delta$, the Kozeny constant k_K which can be substituted in Eq. (3.12) is found to be

$$k_K = \frac{2\varepsilon^3}{(1-\varepsilon)\left[2\ln\frac{1}{1-\varepsilon} - 3 + 4(1-\varepsilon) - (1-\varepsilon)^2\right]} \tag{3.13}$$

and for flow perpendicular to the cylinder axis, the Kozeny constant is

$$k_K = \frac{\frac{2\varepsilon^3}{(1-\varepsilon)}}{\frac{1}{(1-\varepsilon)} - \frac{1-(1-\varepsilon)^2}{1+(1-\varepsilon)^2}} \tag{3.14}$$

3.1.3.2 Numerical solution for flow over cylinder

Sahraoui and Kaviany [103] numerically solved the Navier-Stokes equation for flow over different arrangements of cylinders by applying the finite difference approximation. The authors gave the following correlation for permeability

$$\frac{K}{d^2} = 0.0606\frac{\pi}{4}\frac{\varepsilon^{5.1}}{1-\varepsilon};\ \text{for } 0.4 \le \varepsilon \le 0.8 \tag{3.15}$$

where d is the cylinder diameter.

3.2 High Reynolds number flows

Deviations from Darcy's law is observed by many experimentalists when the velocity is increased above stokes regime. There exists a non linear relationship between the pressure gradient and the flow velocity at higher Reynolds number ($Re_p > 1$) [92]. The reason is due to the contribution of the inertial term to the flow resistance along with the viscous term. In order to account for the inertial resistance, the Darcy equation (Eq. (3.2)) is modified as

$$\frac{\mathrm{d}p}{\mathrm{d}x} = -\frac{\mu}{K}u_s - c_F K^{-0.5}\rho {u_s}^2 \tag{3.16}$$

where c_F is the form drag constant. Eq. (3.16) is also written as

$$\frac{\mathrm{d}p}{\mathrm{d}x} = -\frac{\mu}{K_1}u_s - \frac{\rho}{K_2}{u_s}^2 \tag{3.17}$$

where K_1 and K_2 are generally named as permeability coefficients. The last term in Eq. (3.16) and Eq. (3.17) is called the Forchheimer term, and the equations are generally referred as the Forchheimer equation. A detailed theoretical derivation of the volume averaged momentum equation with the Forchheimer correction by the application of spatial averaging theorem to the Navier-stokes equation along with the closure problem is given by Whitaker [119]. Ward [117] considered c_F to be a constant value of 0.55 for isothermal saturated porous media. For randomly packed bed spheres, considering the influence of bounding walls on the inertial drag, Beavers et al. [10] provided a correlation for c_F as

$$c_F = 0.55\left(1 - 5.5\frac{d}{D_e}\right) \tag{3.18}$$

where d is the diameter of the sphere and D_e is the equivalent diameter of the packed bed

$$D_e = \frac{2wh}{w+h} \tag{3.19}$$

where w is the width of the bed and h is the height. Similar to the method used in section 3.1.2 to derive the Carman-Kozeny-Blake equation, the friction factor Eq. (3.8) can be considered for high Reynolds number flows ($Re_p/(1-\varepsilon) > 1000$) [12]. The friction factor is independent of the Reynolds number (similar to turbulent flows) and is function of only the roughness of the tubes. f_{tube} is considered as a constant and a value of $7/12$ is taken as an acceptable value [12]. Substituting $f_{tube} = 7/12$ in Eq. (3.8) provides

$$f = \frac{7}{8}\left(\frac{1-\varepsilon}{\varepsilon^3}\right) \tag{3.20}$$

Substituting Eq. (3.20) in Eq. (3.5) results in Eq. (3.21), which is the Burke-Plummer equation [18].

$$\frac{\Delta p}{L} = \frac{7}{4}\left(\frac{\rho {u_s}^2}{d_p}\right)\frac{1-\varepsilon}{\varepsilon^3} \tag{3.21}$$

For transition flows, i.e., $10 < Re_p/(1\text{-}\varepsilon) < 1000$, the pressure drop equations Eq. (3.9) and Eq. (3.21) are superposed, which results in the Ergun equation Eq. (3.22) [40].

$$\frac{\Delta p}{L} = 150\left(\frac{\mu u_s}{{d_p}^2}\right)\frac{1-\varepsilon^2}{\varepsilon^3} + 1.75\left(\frac{\rho {u_s}^2}{d_p}\right)\frac{1-\varepsilon}{\varepsilon^3} \tag{3.22}$$

Macdonald et al. [83] modified the friction factor proposed by Ergun [40] as

$$f = \frac{\mathrm{d}p/\mathrm{d}x}{\rho u_s^2} d_p \frac{\varepsilon^3}{1-\varepsilon} = \frac{180(1-\varepsilon)}{Re} + 1.8 \tag{3.23}$$

Eq. (3.23) along with the Carman-Kozeny permeability relation (Eq. (3.11)) is used to obtain an equation for c_F as [68]

$$c_F = 1.8\frac{1-\varepsilon}{\varepsilon^3}\frac{1}{d}K^{0.5} \tag{3.24}$$

3.3 Pressure drop in open cell sponges

Most of the studies to describe the pressure drop within reticulated porous media were based on the Ergun equation (Eq. (3.22)) [79, 90,

91, 100]. Richardson et al. [100] used the hydraulic diameter model to calculate the specific surface area based on solid volume by replacing the hydraulic diameter of packed beds by the pore diameter of the reticulated structures. As the method of replacing hydraulic diameter of packed beds with open cell pore diameter is physically not correct, the authors calculated new constants for the Ergun equation by an empirical fit, introducing a dependency on the pore diameter and porosity of the reticulated porous structure. Moreira et al. [91] compared the Forchheimer equation and the Ergun equation to establish a relation between the porosity of the porous media to the permeability coefficients K_1 and K_2 in Eq. (3.17), and the experimental pressure drop results were used to empirically fit the porosity dependent permeability coefficients to the pore diameter. Dukhan et al. [35] used a similar procedure to the correlate permeability coefficients in terms of porosity and specific surface area. The authors replaced the particle diameter in the Ergun equation with the reciprocal of specific surface area.

Garrido et al. [47] correlated the permeability coefficients in terms of pore diameter and porosity to match their measurements. A cubic cell model is used by Lacroix et al. [74] to find a relation between the strut diameter of the reticulated porous media to the particle diameter of a packed bed having same specific surface area and porosity. The particle diameter obtained from the strut diameter is used in the Ergun equation without modifying the Ergun constants, and no empirical correlation is used. As mentioned by the authors themselves, the model may not be physical meaningful as it is not possible to obtain a packed bed composed of spherical particles with high porosities as that of reticulated structures. Du Plessis [33] correlated their experimental data using a quadratic polynomial, the pre-factors were modeled with the tortuosity. Du Plessis and Woudberg [34] specify in their publication that the Ergun equation is only applicable to Newtonian flow through packed beds in the porosity range of approximately 0.35-0.5.

Edouard et al. [38] listed a wide range of correlations reported in the literature and made a comparison with their experimental data. They concluded that no model is able to correctly predict the pressure drop, and that the standard deviations between the experimental and the theoretical values even reach 100%. The authors also reported that the approach proposed by Du Plessis [33] and Lacroix et al. [74] gave

a reasonable estimate of pressure drop, with most of the experimental data in literature lying within ±30% error.

Dietrich et al. [29] used their experimental pressure drop measurements of various reticulated ceramics (similar to the ones used in this study) to model the two Ergun constants for the Ergun equation. The authors reported that the constants turned out to be independent of material, void fraction and pore density. In a recent publication, Dietrich [28] made a comprehensive comparison of a wide range of experimental data with the general correlation provided in [29]. The correlation is able to predict the non-dimensional pressure drop (Hagen number) within an error range of ±40% for a wide range of Reynolds number $(0.1 - 10^5)$.

With the help of direct pore level simulations one can obtain a correlation based on new insight in the internal flow field, as it is the basic cause of the pressure drop. In this study, the pressure drop correlation is derived from the basic definition of the friction factor for packed beds, the friction factor is defined as [12, 29, 40]

$$f = \frac{\Delta p}{\Delta x}\frac{\varepsilon^2 d_h}{\rho u_s^2} = \zeta/Re + \eta \tag{3.25}$$

And with $Re = u_s \cdot d_h/\varepsilon \cdot \nu$ and $d_h = \frac{4\varepsilon}{S_v}$ the pressure drop is written as

$$\frac{\Delta p}{\Delta x} = \zeta \cdot \frac{\mu {S_v}^2}{\varepsilon^3} u_s + \eta \cdot \frac{\rho S_v}{\varepsilon^3} {u_s}^2 \tag{3.26}$$

where S_v is the specific surface area based on total porous matrix volume. Eq. (3.26) is similar to the Forchheimer equation Eq. (3.16). Comparing Eq. (3.16) and Eq. (3.26) one obtains $\zeta = \varepsilon^3/{S_v}^2 K$ and $\eta = \varepsilon^3 c_F/S_v K^{0.5}$. Direct pore level simulations are used to determine the permeability coefficients values and the constants ζ and η.

3.3.1 Determination of K and c_F

3.3.1.1 Numerical setup and procedure

Assuming air to be a Newtonian fluid having a constant density and with the requirement of steady flow, the governing equations of mass

and momentum conservation are written using Einstein's summation rule as follows:

$$\frac{\partial}{\partial x_j}(\rho u_j) = 0 \tag{3.27}$$

$$\frac{\partial}{\partial x_j}(\rho u_j u_k) = -\frac{\partial p}{\partial x_k} + \frac{\partial}{\partial x_j}\left(\mu \frac{\partial u_k}{\partial x_j}\right) \tag{3.28}$$

where x_j and u_j denote the spatial coordinate and velocity in j-direction, p is the static pressure and μ stands for the dynamic viscosity of air. The fluid flowing within the porous matrices is assumed to be a Newtonian fluid having a constant density and with the requirement of steady flow. Besides the underlying assumptions of the Navier-Stokes equations, no simplifications are necessary. Within the limits of the numerical truncation error (i.e., mesh refinement) and the accuracy of geometrical representation (i.e., statistical variations), direct pore level simulation approaches the exact solution. The boundary conditions at the inlet and outlet were specified using constant gas velocity at inlet and static pressure together with zero gradient condition for the velocity at the outlet.

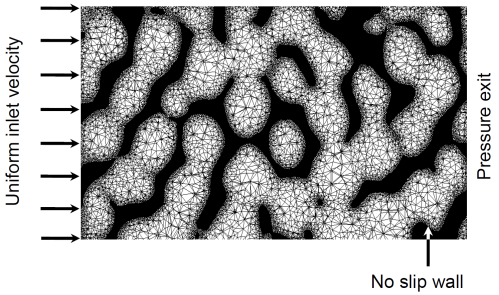

Figure 3.2: Schematic of boundary conditions imposed in DPLS pressure drop calculations.

The domain surfaces perpendicular to the flow direction were given with translational periodic boundary conditions. The structure surfaces are modelled using wall boundary conditions. The flow domains were described based on the reconstructed surfaces of the real probes

as mentioned in Chapter 2. ANSYS CFX commercial CFD software is used to solve the governing equations. ANSYS CFX employs the finite volume method of a cell-centered storage arrangement. A hybrid interpolation scheme is used for the finite volume flux calculations. The schematic of the employed boundary conditions is shown in Figure 3.2. The flow is presumed to be laminar, and so no turbulence model has been used. Considering the extreme spatial resolution (1-4 million grid points for approximately 18000 mm^3, i.e., more than 50 points / mm^3) the simulation could be regarded as a direct numerical simulation.

3.3.1.2 Results

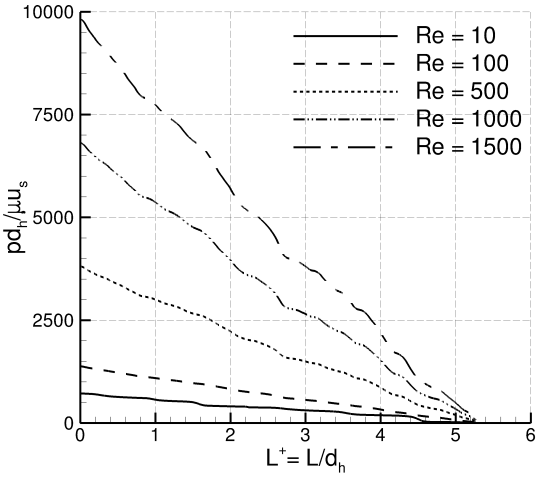

Figure 3.3: Nondimensionalized average pressures along the flow direction in 20 PPI 80% porosity alumina sponge at different Reynolds numbers.

The simulations were carried out for Reynolds numbers ranging from 10 to 1500. The Reynolds numbers ($Re = \rho d_h u_s/\mu$) are calculated using the hydraulic diameter ($d_h = 4\varepsilon/S_v$) as the characteristic length. The nondimensionalized pressures along the normalized length in 20 PPI 80% porosity alumina sponge at different Reynolds numbers are plotted in Figure 3.3.

It can be seen that the pressure drops decrease with decrease in the Reynolds number and tend towards narrowing the difference between the curves. For very low Reynolds numbers, the curves will fall down to a single curve representing the Darcy regime. The pressure drop with respect to superficial flow velocity of 80% porosity alumina structures with different pore density is plotted in Figure 3.4. Shown in Figure 3.5 are the pressure drops of alumina structures with pore density of 30 PPI and varying porosities. As expected, it is observed from Figure 3.4 and from Figure 3.5 that the pressure drops increase with the increase in the pore density, and they decrease with increase in porosity, and also the pressure drop values are second order polynomial with respect to velocity. In order to determine the permeability and the drag constant in Eq. (3.16) from the DPLS results, quadratic fitting of data points is done.

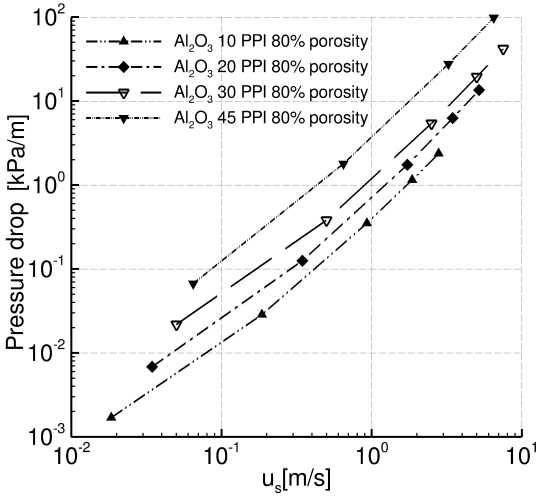

Figure 3.4: Pressure drop per unit length versus superficial air velocity for alumina sponge with different pore density and 80% porosity.

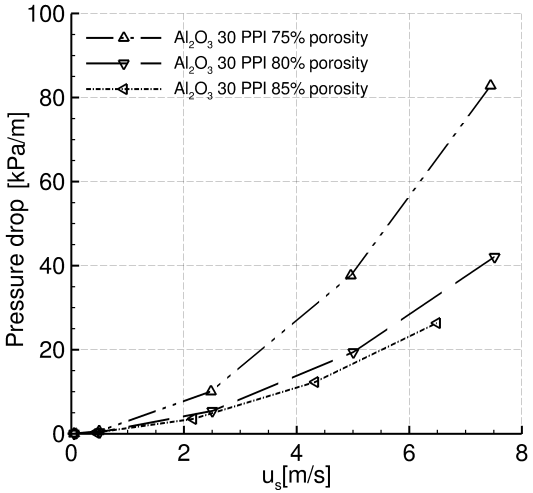

Figure 3.5: Nondimensionalized average pressures along the flow direction in 20 PPI 80% porosity alumina sponge at different Reynolds numbers.

Table 3.1 contains the permeability coefficients that are determined for the investigated structures. The values of constants ζ and η in Eq. (3.26) are calculated using K and c_F. The values of ζ and η are independent of the geometric and material properties of reticulated porous media, and the calculated ζ and η values of different porous matrices have a standard deviation of 1.56 and 0.15, respectively. The mean values ($\overline{\zeta} = 8.1$ and $\overline{\eta} = 0.31$) are obtained by calculating the arithmetic average of the values that are determined for the studied structures. Eq. (3.26) is used to calculate the pressure drop for the porous structures with the mean values of ζ and η. The maximum relative error with reference to the DPLS pressure drop was 45% for 45 PPI Al_2O_3 80% porosity structure, and the error values for all other samples are well within 37%.

Table 3.1: Permeability and friction factor of different sponges determined using DPLS.

Pore density (PPI)	**Nominal porosity(%)**	**Permeability K (m^2)**	**Drag constant c_F (-)**
10 (Al_2O_3)	80	2.17E-07	0.101
20 (Al_2O_3)	75	4.60E-08	0.170
	80	1.02E-07	0.123
	85	8.21E-08	0.116
30 (Al_2O_3)	75	3.38E-08	0.224
	80	4.58E-08	0.123
	85	5.42E-08	0.101
45 (Al_2O_3)	80	2.18E-08	0.368
20 (SiSiC)	85	1.78E-07	0.096
10 (SiSiC)	85	2.37E-07	0.103

Comparing Eq. (3.26) to the pressure drop correlation Eq. (3.29) by Dietrich et al. [29], it can be noticed that the constants in the correlation by Dietrich et al. [29] are A =16ζ and B =4η, which results in Eq. (3.30) for mean values of ζ and η.

$$\frac{\Delta p}{\Delta x} = A \cdot \frac{\mu}{\varepsilon {d_h}^2} u_s + B \cdot \frac{\rho}{\varepsilon^2 d_h} {u_s}^2; Hg = A \cdot Re + B \cdot Re^2 \quad (3.29)$$

$$\frac{\Delta p}{\Delta x} = 129.6 \cdot \frac{\mu}{\varepsilon {d_h}^2} u_s + 1.24 \cdot \frac{\rho}{\varepsilon^2 d_h} {u_s}^2 \quad (3.30)$$

where $Hg = (\Delta p/\Delta x)({d_h}^3/\rho\nu^2)$ is the Hagen number. The values of A and B reported by Dietrich et al. are A = 110, B =1.45. The authors [29] calculated the values of A and B by minimizing the Root Mean Square Deviation (RMSD),

$$RMSD = 10^{RMSD(ELOG)} - 1; ELOG = log(Hg_{calc}) - log(Hg_{exp}) \quad (3.31)$$

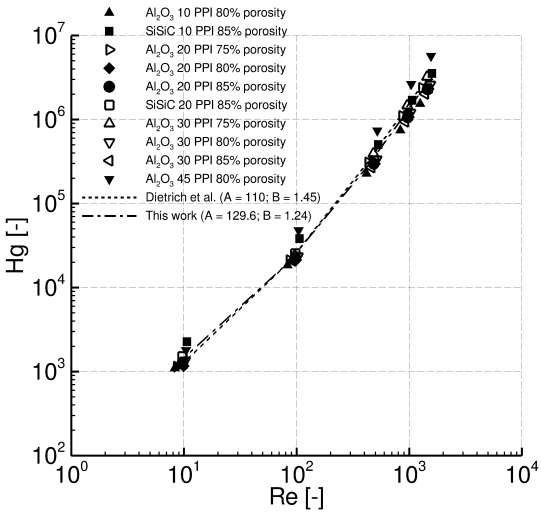

Figure 3.6: Hagen number versus Reynolds number of sponges of different pore density and porosities.

Figure 3.6 shows the Hagen numbers as a function of Reynolds numbers for different sponges. As reported by Dietrich et al. [29], it is seen that the relation between the Hagen number and the Reynolds number form a single line, denoting the similarity in the geometric structures of the ceramic sponges. The Hagen number based on the correlation suggested by Dietrich et al. [29] and the Hagen numbers found using constant A = 129.6 and B = 1.24 are also plotted in Figure 3.6. Both the correlations match the Hagen number data rather well. Dietrich [28] reported that the correlation for Hagen number Eq. (3.29) satisfies a vast amount of experimental results in the literature, and the RMSD value is within 40%. The Eq. (3.29) when compared to the DPLS results has a RMSD of 30.5%, which is well within the RMSD of 40% reported by Dietrich [28] for the available literature data. But the constants A = 129.6 and B = 1.24 provide a lesser RMSD of 26% for the DPLS results. When the friction factors are calculated using Eq. (3.25) with A = 110 and B =1.45, the maximum relative error is 57% with respect to DPLS results, and with A = 129.6 and B = 1.24 the maximum relative error is 45%, though the values of A and B in this

study are calculated using the arithmetic mean values of ζ and η, the mean values also provide the least RMSD. Thus it is concluded that, though the general pressure drop correlation provided by Dietrich et al. [29] provides an acceptable correlation for pressure drop values, a slightly modified value of A = 129.6 and B = 1.24 represents better the simulated pressure drop values.

Figure 3.7, Figure 3.8 and Figure 3.9 show the comparison of the friction factors calculated using Eq. (3.25) (with $\zeta = 8.1$, $\eta = 0.31$) to the DPLS friction factors. As mentioned before, the calculated friction factor of the 45 PPI Al_2O_3 80% porosity matrix has the maximum deviation in comparison to the DPLS friction factor.

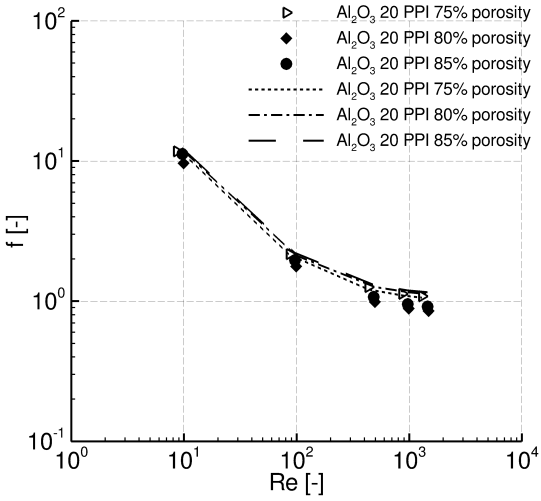

Figure 3.7: Comparison between correlated and DPLS friction factors (shown in lines and symbols, respectively) for 20 PPI sponge.

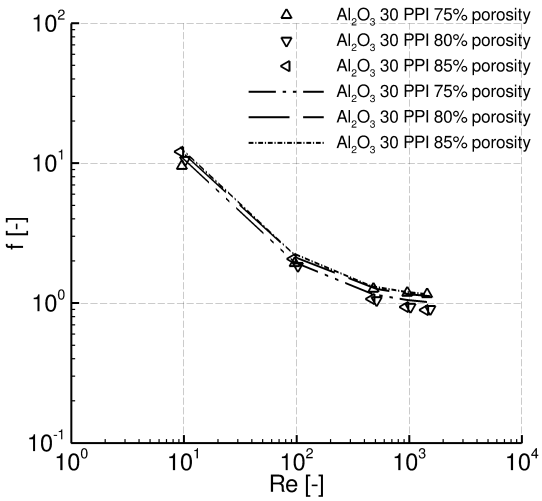

Figure 3.8: Comparison between correlated and DPLS friction factors (shown in lines and symbols, respectively) for 30 PPI sponge.

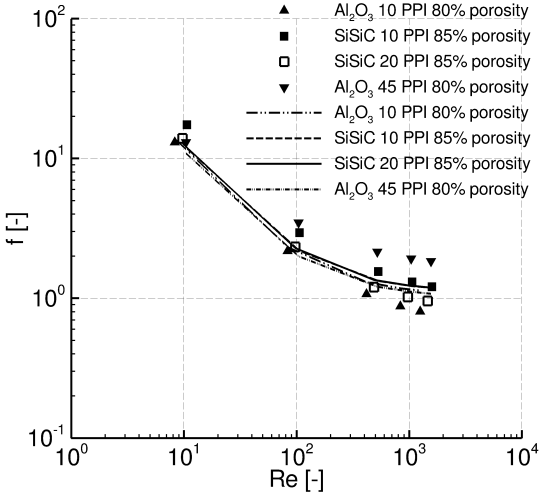

Figure 3.9: Comparison between correlated and DPLS friction factors (shown in lines and symbols, respectively).

In a DPLS study made by Habisreuther et al. [52] to replicate the pressure drop of real porous structure with Kelvin structure, the authors noticed that the pressure drop of randomized Kelvin structure with same porosity, pore density and specific surface area as that of the real porous matrix had a very low pressure drop in comparison to the real 45 PPI Al_2O_3 80% porosity matrix. In order to achieve a pressure drop close to that of real structures, the authors had to randomly close the pore windows of the randomized Kelvin structure to increase the flow tortuosity, maintaining same porosity, pore density and specific surface area. The manufacturing of high pore density reticulated porous structures (such as 45 PPI) using replication methods are generally associated with presence of closed pores [98], which makes the flow to take a relatively longer flow path and the form (inertial) drag increases due to the increase in flow obstruction caused by the presence of closed pores.

In order to study the influence of flow tortuosity on the pressure drop, the tortuosities of the different structures used in this study are calculated using the approach used by Habisreuther et al. [52]. Numerical tracking of the path taken by almost mass free particles, that are used to mark the flow path through the porous matrix. The integration of the particle path results in the increased path length L_p. The tortuosity is calculated from its definition ($\tau = Lp/L$). Lagrangian particle tracking (LPT) method is used to track the particle in the Eulerian fluid phase flow. The particle displacement is calculated using forward Euler integration of the particle velocity over time step δ_t. The algorithm is a standard in most flow solvers. Only the drag force of the fluid on the particle was considered. The coefficient of drag is calculated using Schiller-Naumann drag model [106], with 0.44 as the limiting value in the inertial regime. The Particle diameter is taken close to zero (10 nm) with density (2000 kg/m^3) to minimize the slip velocity between the particle trajectory and the flow due to particle inertia, so that the particle velocity reaches flow velocity. Around 30000 particles are analyzed in each simulation. Habisreuther et al. [52] reported that the randomized Kelvin structure in absence of closed pores has a flow tortuosity of 1.08, which is taken as a reference value in this study. As the value of 1.08 denotes a porous matrix without closed pores, in presence of closed pores the flow tortuosity is expected to increase. The mean

Table 3.2: Constants ζ and η and flow tortuosity of different sponges determined using DPLS.

Pore density (PPI)	**Nominal porosity(%)**	ζ **(-)**	η **(-)**	τ **(-)**
10 (Al_2O_3)	80	7.6	0.20	1.08
20 (Al_2O_3)	75	7.5	0.31	1.14
	80	6.6	0.23	1.08
	85	7.4	0.25	1.06
30 (Al_2O_3)	75	6.8	0.37	1.11
	80	7.5	0.25	1.06
	85	7.5	0.23	1.06
45 (Al_2O_3)	80	8.7	0.76	1.31
20 (SiSiC)	85	8.9	0.23	1.08
10 (SiSiC)	85	12.3	0.29	1.12

tortuosity τ values of the sponges are tabulated in Table 3.2. It can be noticed from Table 3.2, that the increase in η value can be related to the increase in flow tortuosity. The constant η of 45 PPI Al_2O_3 80% porosity matrix is much higher than the average value of all other structures, which also has the highest tortuosity value. A high value of η denotes an increase in the form drag term, the second term in Eq. (3.26). In order to accommodate the effect of tortuosity, Eq. (3.25) and Eq. (3.26) is modified as,

$$f = \frac{\Delta p}{\Delta x}\frac{\varepsilon^2 d_h}{\rho u_s^2} = \zeta/Re + \frac{\tau}{\tau'}\eta \tag{3.32}$$

$$\frac{\Delta p}{\Delta x} = \zeta \cdot \frac{\mu {S_v}^2}{\varepsilon^3} u_s + \frac{\tau}{\tau'}\eta \cdot \frac{\rho S_v}{\varepsilon^3} {u_s}^2 \tag{3.33}$$

where, $\tau' = 1.08$ is the tortuosity value of a randomized Kelvin structure without closed pores. The maximum relative error for friction factor of the sponges in comparison to the DPLS friction factor reduced from 44% to 38%, and the RMSD error of the Hagen number correlation (Eq. (3.29)) with A = 129.6 and B = 1.24 reduced to 21.5%. It is

observed from Table 3.2 that the SiSiC structures have the highest ζ value among the studied structures and have larger deviations from the mean value. The ζ values in Eq. (3.25) denotes the friction drag, higher values of ζ denotes higher friction for same surface area. In the case of DPLS simulations, the reconstructed domain surfaces are smoothened out and are incapable of capturing the true micro surface roughness of the material, and thus the increase in the ζ value cannot be related to the material, but may be to the strut cross-section and node geometries, which effect the velocity boundary layers, and so, the frictional drag. However, at velocities much above Darcy regime, the effect of frictional drag term in Eq. (3.26), in comparison to the form drag is less pronounced. It is thus concluded that the strut cross-section profile may have a considerable effect when the Reynolds number is near to the Darcy regime and the general correlation Eq. (3.30) may under predict the pressure drop within the reticulated porous structures.

Chapter 4

Axial dispersion in ceramic sponges

The process of diffusion is mixing of one type of fluid molecules (tracer) into a continuum of other fluid molecules. Similarly, thermal diffusion is the transfer of internal energy by molecular diffusion and collisions of particles due to the temperature gradient. Diffusion occurs by random motion of the tracer (or high energy) molecules into the fluid due to the presence of tracer concentration gradient (or temperature gradient). Diffusion is a molecular level mixing process, where the fluid molecules are having random Brownian motion. The term dispersion is similar to that of diffusion, but it happens in a macroscopic level, where the mixing of tracer molecules with the fluid molecules is enhanced by the fluid flow. Dispersion can be viewed as convection induced spreading or mixing [113]. One of the earliest studies of hydrodynamic dispersion was by Taylor [110]. Taylor studied the mixing of a tracer fluid in a fully developed flow through a circular tube. Figure 4.1 shows the schematic of the study by Taylor. A tracer solution is injected at plane A, and the concentration moves downstream due to the flow. The velocity field is fully developed and is given by Hagen-Poiseuille equation (Eq. (4.1)).

$$u = 2\overline{u}\left(1 - \frac{r^2}{R^2}\right) \tag{4.1}$$

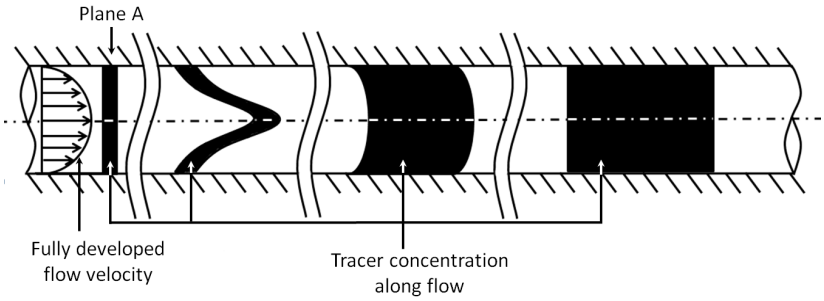

Figure 4.1: Mixing and spreading of tracer in a tube caused by fluid flow.

In presence of molecular diffusion, the concentration Y equation is given by

$$\frac{1}{D_m}\frac{\partial Y}{\partial t} + \frac{1}{D_m}u\frac{\partial Y}{\partial x} = \left(\frac{\partial^2 Y}{\partial r^2} + \frac{1}{r}\frac{\partial Y}{\partial r} + \frac{\partial^2 Y}{\partial x^2}\right) \tag{4.2}$$

For simplicity, Taylor assumed the molecular diffusion coefficient to be independent of concentration Y, and in his experiments the term $\frac{\partial^2 Y}{\partial x^2}$ is much less than $\frac{1}{r}\frac{\partial Y}{\partial r} + \frac{\partial^2 Y}{\partial r^2}$. Using the above condition, Eq. (4.2) becomes

$$\frac{1}{D_m}\frac{\partial Y}{\partial t} + \frac{1}{D_m}u\frac{\partial Y}{\partial x} = \left(\frac{\partial^2 Y}{\partial r^2} + \frac{1}{r}\frac{\partial Y}{\partial r}\right) \tag{4.3}$$

The molecular diffusion in the axial direction is neglected and he considered the convection across a plane which moves at a constant speed $\overline{u}$. The axial coordinate is transformed according to $x' = x - \overline{u}t$. The transformation is done so that the variable x' corresponds to an observer moving with the fluid. Since the mean velocity $\overline{u}$ across the plane for which x' is constant is zero, the transfer of Y across such planes depends only on the variation of Y in the radial direction. Using chain rule, Eq. (4.3) is transformed as

$$\frac{1}{D_m}\left(\frac{\partial Y}{\partial t}\right)_{x'} + \frac{1}{D_m}[u - \overline{u}]\frac{\partial Y}{\partial x'} = \left(\frac{\partial^2 Y}{\partial r^2} + \frac{1}{r}\frac{\partial Y}{\partial r}\right) \tag{4.4}$$

Substituting Eq. (4.1) in Eq. (4.4)

$$\frac{1}{D_m}\left(\frac{\partial Y}{\partial t}\right)_{x'} + \frac{1}{D_m} 2\overline{u}\left(\frac{1}{2} - \frac{r^2}{R^2}\right)\frac{\partial Y}{\partial x'} = \left(\frac{\partial^2 Y}{\partial r^2} + \frac{1}{r}\frac{\partial Y}{\partial r}\right) \quad (4.5)$$

As the observer moves along with the fluid, for large elapsed times the solute concentration does not change with the time and there exists an asymptotic behavior ($\frac{\partial Y}{\partial t} \to 0$), Eq. (4.5) becomes

$$\frac{1}{D_m} 2\overline{u}\left(\frac{1}{2} - \frac{r^2}{R^2}\right)\frac{\partial Y}{\partial x'} = \left(\frac{\partial^2 Y}{\partial r^2} + \frac{1}{r}\frac{\partial Y}{\partial r}\right) \quad (4.6)$$

As the observer moves along with the fluid, after large elapsed times the axial concentration gradient will become independent of radial position, as a consequence

$$\frac{\partial Y}{\partial x'} \cong \frac{\partial \overline{Y}}{\partial x'} \quad (4.7)$$

Using the above approximation, Eq. (4.6) is written as

$$\frac{1}{D_m} 2\overline{u}\left(\frac{1}{2} - \frac{r^2}{R^2}\right)\frac{\partial \overline{Y}}{\partial x'} = \left(\frac{\partial^2 Y}{\partial r^2} + \frac{1}{r}\frac{\partial Y}{\partial r}\right) \quad (4.8)$$

As $\frac{\partial \overline{Y}}{\partial x'}$ is independent of r, Eq. (4.8) is rearranged and integrated with respect to r

$$\begin{aligned} r\frac{\mathrm{d}Y}{\mathrm{d}r} &= \frac{\overline{u}}{D_m}\frac{\partial \overline{Y}}{\partial x'}\int_0^r \left[1 - 2\left(\frac{r}{R}\right)^2\right] r\mathrm{d}r \\ &= \frac{\overline{u}}{D_m}\frac{\partial \overline{Y}}{\partial x'}\left(\frac{r^2}{2} - \frac{2}{4}\frac{r^4}{R^2}\right) + C_1 \end{aligned} \quad (4.9)$$

Due to the symmetry of the flow, $\frac{\partial Y}{\partial r}(r = 0, x') = 0$, and therefore the integration constant C_1 equals zero. Eq. (4.9) is divided by r on both sides, and a second integration with respect to r gives

$$Y = \frac{R^2\overline{u}}{4D_m}\frac{\partial \overline{Y}}{\partial x'}\left(\frac{r^2}{R^2} - \frac{1}{2}\frac{r^4}{R^4}\right) + C_2 \quad (4.10)$$

The constant C_2 is independent of r and evaluated using the average axial concentration $\overline{Y}$ given by

$$\begin{aligned}\overline{Y}(x',t) &= \frac{1}{\pi R^2}\int_0^R Y(r,x',t)2\pi r\mathrm{d}r \\ &= \frac{1}{\pi R^2}\int_0^R \left[\frac{R^2\overline{u}}{4D_m}\frac{\partial\overline{Y}}{\partial x'}\left(\frac{r^2}{R^2}-\frac{1}{2}\frac{r^4}{R^4}\right)+C_2\right]2\pi r\mathrm{d}r\end{aligned} \tag{4.11}$$

Let z = r/R

$$\begin{aligned}\overline{Y}(x',t) &= C_2 + \frac{2R^2\overline{u}}{4D_m}\frac{\partial\overline{Y}}{\partial x'}\int_0^1\left(z^3-\frac{z^5}{2}\right)\mathrm{d}z \\ &= C_2 + \left[\frac{z^4}{4}-\frac{x^6}{12}\right]_0^1\frac{2R^2\overline{u}}{4D_m}\frac{\partial\overline{Y}}{\partial x'}\end{aligned} \tag{4.12}$$

Solving for C_2 yields

$$C_2 = \overline{Y} - \frac{R^2\overline{u}}{12D_m}\frac{\partial\overline{Y}}{\partial x'} \tag{4.13}$$

Subsituting Eq. (4.13) in Eq. (4.10) gives

$$Y = \overline{Y} + \frac{R^2\overline{u}}{4D_m}\frac{\partial\overline{Y}}{\partial x'}\left[-\frac{1}{3}+\frac{r^2}{R}-\frac{1}{2}\frac{r^4}{R^4}\right] \tag{4.14}$$

Finally, to arrive at the Taylor dispersion coefficient D_L, Eq. (4.4) is multiplied by the differential cross-sectional area $2\pi r\mathrm{d}r$ and carry out integration over the pipe radius R

$$\begin{aligned}&\frac{1}{\pi R^2}\left[\int_0^R\frac{1}{D_m}\left(\frac{\partial Y}{\partial t}\right)_{x'}2\pi r\mathrm{d}r + \int_0^R\frac{1}{D_m}2\overline{u}\left(\frac{1}{2}-\frac{r^2}{R^2}\right)\frac{\partial Y}{\partial x'}2\pi r\mathrm{d}r\right] \\ &\qquad = \frac{1}{\pi R^2}\left[\int_0^R\frac{\partial^2 Y}{\partial r^2}2\pi r\mathrm{d}r + \int_0^R\frac{1}{r}\frac{\partial Y}{\partial r}2\pi r\mathrm{d}r\right]\end{aligned} \tag{4.15}$$

Changing the order of differentiation and integrating the first term and

recalling Eq. (4.11) yields

$$\left(\frac{\partial \overline{Y}}{\partial t}\right)_{x'} + 2\overline{u}\int_0^1 \left(\frac{1}{2} - \frac{r^2}{R^2}\right)\frac{\partial Y}{\partial x'}\frac{r}{D}\mathrm{d}\left(\frac{r}{R}\right) = \frac{2}{R^2}D_m\int_0^R \mathrm{d}\left(\frac{r\partial \overline{Y}}{\partial r}\right) \tag{4.16}$$

At the pipe wall, i.e., at r = R

$$\frac{\partial \overline{Y}}{\partial r} = 0 \tag{4.17}$$

Integrating the right hand side in Eq. (4.16) along with the above boundary condition gives

$$D_m\int_0^R \mathrm{d}\left(r\frac{\partial \overline{Y}}{\partial r}\right) = D_m\left[r\frac{\partial \overline{Y}}{\partial r}\bigg|_R - r\frac{\partial \overline{Y}}{\partial r}\bigg|_0\right] = 0 \tag{4.18}$$

Further, differentiating Eq. (4.14) with respect to x' and substituting it into the second term on the left hand side of Eq. (4.16) gives

$$\left(\frac{\partial \overline{Y}}{\partial t}\right)_{x'} + 2\overline{u}\int_0^1 \left(\frac{1}{2} - \frac{r^2}{R^2}\right)\left[\frac{\partial Y}{\partial x'} + \frac{R^2\overline{u}}{4D_m}\frac{\partial^2 \overline{Y}}{\partial x'^2}\left(\frac{1}{3} + \frac{r^2}{R} - \frac{1}{2}\left(\frac{r^4}{R^4}\right)\right)\right]\frac{r}{R}\mathrm{d}\left(\frac{r\partial \overline{Y}}{\partial r}\right) = 0 \tag{4.19}$$

Integrating between 0 and 1 yields

$$\left(\frac{\partial \overline{Y}}{\partial t}\right)_{x'} = \frac{1}{48}\frac{\overline{u}^2R^2}{D_m}\frac{\partial^2 \overline{Y}}{\partial x'^2} \tag{4.20}$$

Changing the variable x' back to x gives

$$\left(\frac{\partial \overline{Y}}{\partial t}\right)_{x} = D_L\frac{\partial^2 \overline{Y}}{\partial x^2} \tag{4.21}$$

where, $D_L = \frac{R^2\overline{u}^2}{48D_m}$ is the axial dispersion coefficient, which can be written in terms of molecular Peclet number $Pe_m = 2R\overline{u}/D_m$ as

$$D_L = \frac{D_m}{192}Pe_m^2 \tag{4.22}$$

4.1 Axial dispersion in open cell ceramics

Solid sponges made of ceramic, metal or polymeric material are highly porous, monolithic materials with excellent mixing properties. Their open-cell structure consists of stiff, interconnected struts building a continuous network. Because of the high volumetric porosity, such structures exhibit a relatively small pressure loss and provide good mixing properties and thus are an interesting material for chemical process engineering purpose. Additionally, sponges made of ceramics, depending on the bulk material bear temperatures up to 1700 K and can be utilized in porous burners in order to enhance the volumetric heat release by enhancing the thermal and mass transport processes. Dispersion can be described considering a fluid flow in such a porous medium, where a fraction of the fluid is labelled as tracer. The tracer mixes with the unlabelled fluid through a non-steady, irreversible process known as hydrodynamic dispersion. The theory of dispersion for porous media from its historical development is presented by Bear [9] and several relevant theoretical predictions are given by Koch & Brady [69]. As described by Boon et al. [16] hydrodynamic dispersion is analogous to the turbulent diffusion phenomenon, where the porous matrix plays the role of eddies in dispersing the flow. A macroscopic description of the phenomenon was derived by Carbonell & Whitaker [21] from the convection-diffusion equation by volume averaging in a porous medium:

$$\phi \frac{\partial^2 Y}{\partial t} + \nabla \cdot (\phi \mathbf{u} Y) = \nabla \cdot (\phi D \cdot \nabla Y) \tag{4.23}$$

where Y is the tracer concentration, ϕ is the fluid volume fraction, $\mathbf{u}$ is the fluid velocity within the pores, and D is the hydrodynamic (macroscopic) dispersion tensor. The relative importance of molecular diffusion and hydrodynamic dispersion for spreading the tracer is described by the Peclet number, $Pe_m = ud/D_m$, where u is the fluid velocity within the pores, d denotes a characteristic length of the porous medium, and D_m is the relevant coefficient of molecular diffusion. For increasing Peclet numbers, the influence of hydrodynamic dispersion too increase. The phenomenon of hydrodynamic dispersion has been investigated by many researchers in the past, Maier et al. [84] give a good overview over these investigations together with more recent investigations that have been conducted using new experimental meth-

ods (e.g., pulsed-gradient spin echo NMR) and new numerical methods like the Lattice Boltzmann (LB) methods on the pore level. Delgado [27] in his recent review analyses vast data on dispersion in porous media that are available in literature and formulates simple correlations for the prediction of longitudinal and transversal dispersion coefficients for gaseous and liquid flow. For relatively high Pe_m numbers (>60), the longitudinal component D_L of the macroscopic dispersion tensor D has been found to asymptotically approach a linear function of Pe_m. Instead of using the most common representation of dispersion coefficients that show the dependence of the ratio D_L/D_m as a function of Pe_m, Delgado [27] uses the definition of a macroscopic Peclet number in longitudinal direction $Pe_L = ud/D_L$ in order to better resolve the data found in the literature. For gaseous flow in porous media at high Pe_m numbers, an asymptotic value of $Pe_L = 2$ can represent the data for beds with spherical elements in good accordance. Despite the vast amount of the data available in the literature, dispersion coefficients for highly porous media like sponge structures are scarce. This is due to the fact that the dispersion is subject to the internal structure of the porous media and therefore cannot be described without taking this structure into account. In addition, such data usually is not available from the suppliers of the commercially available ceramic sponges. Thus, the present work aims in calculating the effective axial dispersion coefficients of various sponge structures.

4.1.1 Numerical setup

Assuming air to be a Newtonian fluid having a constant density and with the requirement of unsteady flow, the governing equations of mass and momentum conservation is written using Einstein's summation rule as follows:

$$\frac{\partial \rho}{\partial t} + \frac{\partial}{\partial x_j}(\rho u_j) = 0 \tag{4.24}$$

$$\frac{\partial}{\partial t}(\rho u_k) + \frac{\partial}{\partial x_j}(\rho u_j u_k) = -\frac{\partial p}{\partial x_k} + \frac{\partial}{\partial x_j}\left(\mu \frac{\partial u_k}{\partial x_j}\right) \tag{4.25}$$

The equations are similar to Eq. (3.27) and Eq. (3.28), respectively, but are for instationary flow. The boundary conditions at the inlet and outlet are specified using constant gas velocity at the inlet and static pressure together with zero gradient condition for the velocity at the outlet. The domain surfaces perpendicular to the flow direction are given with translational periodic boundary conditions. The structure surfaces are modelled using wall boundary conditions.

4.1.2 Numerical procedure

The starting point is the simulation of the stationary flow of air through the void phase of sponges. Using the converged stationary solution as a starting condition, a transient calculation is performed, where the incoming fluid is suddenly changed from air to tracer air having same properties as that of air and with molecular diffusion coefficient $D_m = 1.3 \times 10^{-5} \mathrm{m}^2/\mathrm{s}$. The tracer air is then transported by convection and diffusion through the sponge structure. In order to calculate an effective dispersion coefficient from CFD simulation, the instantaneous three-dimensional mixture fields are reduced into one-dimensional ones using mass flow average over N cross-sectional planes perpendicular to the main flow direction:

$$\overline{Y(x_k,t)} = \frac{\sum_{i=1}^{M} (Y_i(t) \cdot \rho u_i A_i(x_k))}{\sum_{i=1}^{M} \rho u_i A_i(x_k)} \tag{4.26}$$

$\overline{Y(x_k,t)}$ denotes the mass flow averaged tracer mass fraction at the k-th cross-sectional plane at position x_k and for the time t, $\rho u_i A_i(x_k)$ stands for the mass flow in the plane with the i-th grid cell, M is the number of grid cells and $Y_i(t)$ is the tracer mass fraction value in the i-th grid cell at time t. The result of this procedure yields the progress

of the one-dimensional dispersion field in time. Figure 4.2 shows the positions of surfaces with constant mass fraction of tracer $Y = 0.5$.

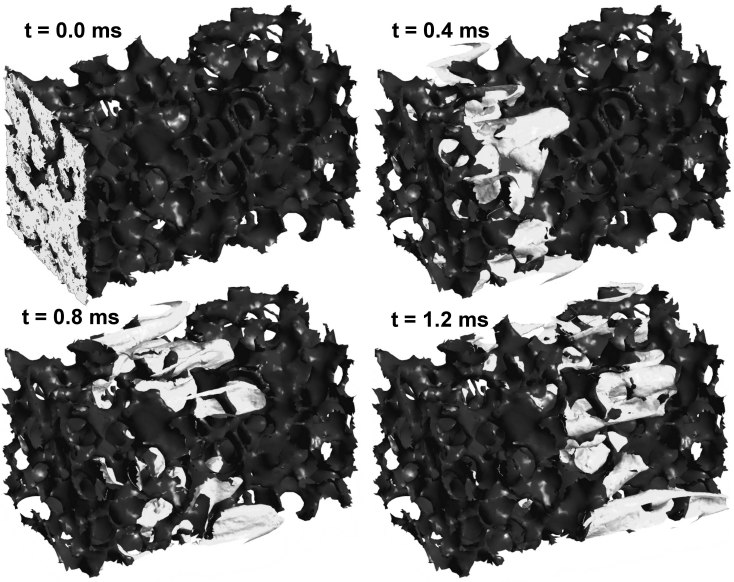

Figure 4.2: Four instantaneous positions of surfaces with constant mass fraction of tracer $Y = 0.5$ (light grey) propagating through a sponge structure (dark grey).

Following an approach similar to the one of Maier et al. [84] the dispersion coefficient is evaluated from the time history of the mass fraction profiles of a tracer species which is introduced into the flow through the porous media. In contrast to a similar method used in [54] and more recently in [94], in the present work, the longitudinal dispersion coefficient was evaluated using a sudden concentration jump at the inlet of the flow system.

As seen previously, the transient one dimensional transport of concentration jump by advection and diffusion is analytically described in a frame of reference moving with the mean flow velocity ($x' = x - u \cdot t$)

by Fick's law with the differential equation:

$$\frac{\partial \overline{Y}}{\partial t} = D_L \frac{\partial^2 \overline{Y}}{\partial x'^2} \tag{4.27}$$

where Y is the tracer concentration and D_L denotes the dispersion coefficient. The analytical solution of this differential equation is well known and can be found in standard text books [93].

$$\overline{Y} = 1 - erf\left(\frac{x'}{2\sqrt{D_L \cdot t}}\right) \tag{4.28}$$

As an example the calculated mass fraction profiles for the dispersion in a 20 PPI SiSiC 85% porosity sponge with this time behavior are shown in Figure 4.3.

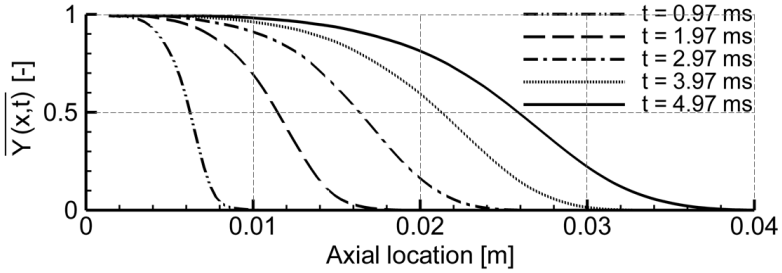

Figure 4.3: Instantaneous mass fraction profiles at five time steps.

In order to evaluate the effective dispersion coefficient, it is more convenient to analyze the gradient of the concentration profiles $\partial Y/\partial x$:

$$\frac{\partial \overline{Y}}{\partial x} = -\frac{2}{2\sqrt{\pi \cdot D_L \cdot t}} exp\left(-\frac{x'^2}{4tD_L}\right) \tag{4.29}$$

Assuming that the simulated concentration gradient is of Gaussian type, the dispersion coefficient is evaluated fitting the width of the gradient curve of the analytical solution to the one of the simulation results, which is approximated using a central difference scheme:

$$\frac{\partial \overline{Y(x,t)}}{\partial x} = \frac{\overline{Y(x_{k+1},t)} - \overline{Y(x_{k-1},t)}}{x_{k+1} - x_{k-1}} \tag{4.30}$$

In Figure 4.4 three selected instances of the mass fraction gradient is displayed for the dispersion in a 20 PPI SiSiC 85% porosity sponge.

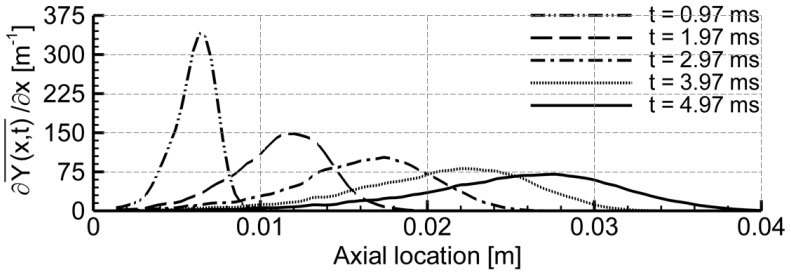

Figure 4.4: Instantaneous mass fraction gradient profiles at five time steps.

In order to fit the analytic solution gradient to the simulated gradient the variance $\sigma^2 = 2tD_L$, i.e., the width of the Gaussian function Eq. (4.29) has to be adjusted to the second moment σ^2_{sim} of the simulated gradient which leads to:

$$D_L(t) = \frac{\sigma^2_{sim}(t)}{2t} \tag{4.31}$$

A presumption of Eq. (4.31) is that there exists an infinite domain around the initial concentration jump which, for practical reasons, cannot be realized and is violated especially near the inlet boundary condition of the numerical simulation in short period of time after the initial time step. Therefore, it is more accurate to evaluate the average longitudinal dispersion coefficient $D_L(t)$ by comparing two values of the variance in time t and $t+\Delta t$: $\Delta\sigma^2_{sim}(t)\Delta t$. This yields the longitudinal dispersion coefficient to be equal to:

$$D_L(t) = 0.5\frac{\Delta\sigma^2_{sim}(t)}{\Delta t} \tag{4.32}$$

For the calculation of the time dependent variances $\sigma^2_{sim}(t)$ the first and second moments of the concentration gradient profiles have to be evaluated:

$$\overline{x_{sim}(t)} = \sum_{k=1}^{N}\left(\frac{\partial\overline{Y(x_k,t)}}{\partial x}\cdot x_k(t)\cdot\frac{x_{k+1}(t)-x_{k-1}(t)}{2}\right) \tag{4.33}$$

$$\sigma^2_{sim}(t) = \sum_{k=1}^{N} \left(\frac{\partial \overline{Y(x_k,t)}}{\partial x} \cdot (x_k(t) - \overline{x_{sim}(t)})^2 \cdot \frac{x_{k+1}(t) - x_{k-1}(t)}{2} \right) \tag{4.34}$$

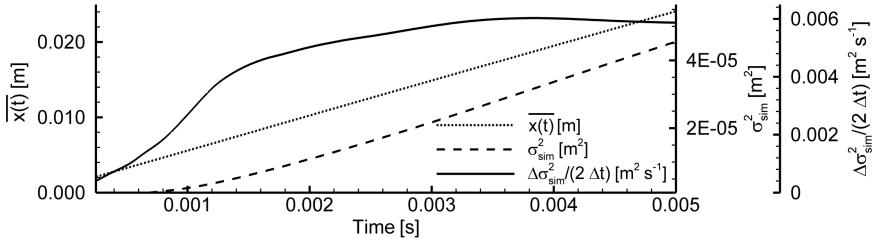

Figure 4.5: Time evolution of first and second moment (mean: dotted line and variance: dashed line) of the mass fraction gradients and resulting dispersion coefficient (solid line).

As an example, Figure 4.5 shows the first and second moment ($\overline{x_{sim}(t)}$ and $\sigma^2_{sim}(t)$) for the 20 PPI SiSiC 85% porosity structure as well as the resulting longitudinal dispersion coefficient $D_L(t)$ as a function of time. It is observed that after a short period of time (ca. 3 ms) an almost constant value is obtained. In order to compare the dispersion of the different structures, one dispersion coefficient of the time evolution has to be selected. In the present work, the maximum value of the curve (0.00603 m^2 s^{-1} for the shown example) was chosen.

4.1.3 Results and discussion

Very few studies were carried out in determining the axial dispersion coefficient of highly porous solid sponge structures [63]. In this study the simulations were carried for various sponge structures of different porosity, pore density (PPI) and material. Taylor [110] examined the effect of column length from the exact analytical solution of the convection-diffusion equation for a laminar flow in a capillary tube. The constraint above which the axial dispersion is independent of column length is given by Eq. (4.35),

$$\theta = D_m \cdot t/R^2 >> 0.14 \tag{4.35}$$

where R is the tube radius, θ is a dimensionless time and D_m is the molecular diffusivity. Carbonell and Whitaker [21] reported that for any porous medium, the dispersion coefficient reaches a constant value if the constraint Eq. (4.36) is satisfied:

$$\theta = D_m \cdot t/l_b^2 >> 1 \tag{4.36}$$

where l_b is the characteristic length associated with the pore space in the fluid-solid system. Han et al. [55] showed that for a packed bed of uniform particle size, the axial dispersion coefficient is independent of the column length, if the dimensionless time θ is equal or above 0.3.

$$\theta = \left(\frac{L}{d_p}\right) \frac{1}{Pe_p} \left(\frac{1-\varepsilon}{\varepsilon}\right) \geq 0.3 \tag{4.37}$$

where L is the distance from inlet, d_p the particle diameter, Pe_p is the Peclet number with particle diameter as the characteristic length and ε is the porosity. There is no such specific creation found in literature for highly porous sponge structures. In this study, we used a similar approach reported in [55] to find the dimensionless time θ. The dimensionless time θ, above which the axial dispersion coefficient becomes constant is dependent on the porous medium structure. θ is different for different sponge structure used in this study. In Figure 4.6 the normalized axial dispersion coefficient $D_L/D_{L\infty}$ of a SiSiC 20 PPI 85 % porosity sponge at $Pe_m = 893$ is plotted against the dimensionless time θ, where the d_p here is the strut diameter. It is observed for this sponge structure, the axial dispersion values attain a constant value above $\theta = 0.012$, which is considerably less than the value reported in [55] for a packed bed of uniform particle size.

In a packed bed, the dependence of the packing particle shape on the axial dispersion was studied by several investigators. It was reported that the axial dispersion is dependent on the packing particle shape even with similar particle size. This dependency on packing particle shape in packed beds indicates that there may be a considerable difference in the axial dispersion in the sponges in comparison to the packed bed.

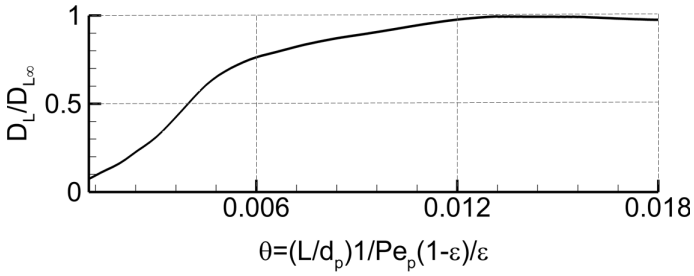

Figure 4.6: Axial dispersion coefficient dependence on θ.

In Figure 4.7 the ratio of numerically determined axial dispersion coefficient to the molecular diffusion results obtained in this study are plotted versus the molecular Peclet number, to allow the comparison with the literature data avaliable for gas dispersion in packed beds. The pore diameter is considered as the characteristic length in calculating Peclet number.

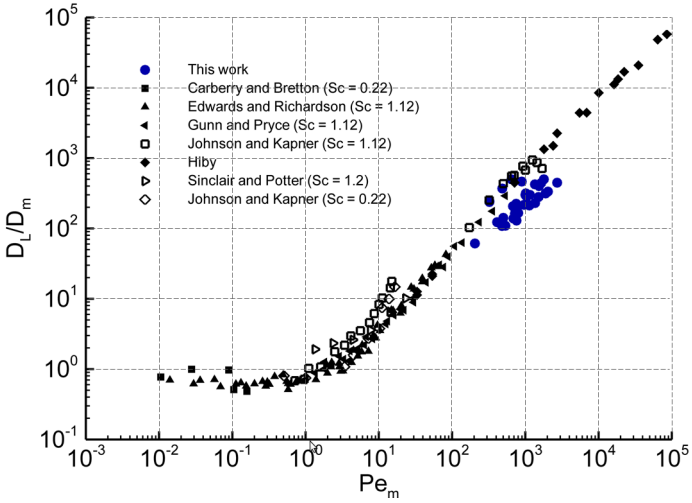

Figure 4.7: Comparison of axial dispersion of gaseous flow in sponge structures to packed beds (plotted literature data are taken from Delgado [26]).

The average pore diameter and the pore density of the sponge are characterized using the tomography data as described in Chapter 2. The D_L/D_m ratio of the sponge structures follow the linearly increasing trend that is widely reported for that of packed beds, but the ratio values are smaller than that of packed beds. Shown in Figure 4.8 are the normalized axial dispersion values for the various sponges used in this study. Similar to the packed beds, the axial dispersion values of sponge structures increase linearly with increase in molecular Peclet number. Taylor's [110] analysis indicates that the process of axial dispersion is a consequence of lateral mixing in shear flow, and Prausnitz [97] explained that in porous structures, the radial mixing is result of lateral movement of the fluid element when it encounters a solid structure in its flow path. In order to avoid the solid obstacle the fluid is forced to take a long roundabout route. During the process the fluid element gets into the region having different axial velocity, so that the axial dispersion is regarded as a result of the radial mixing and also the lateral velocity gradient.

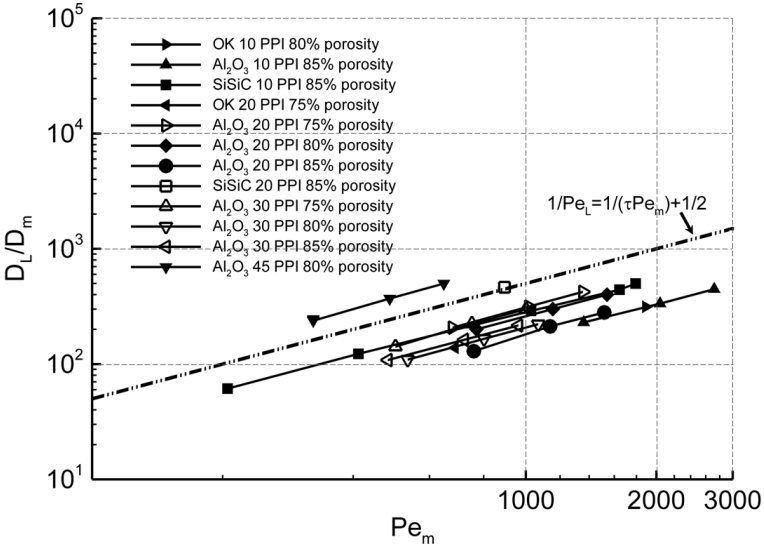

Figure 4.8: Axial dispersion of gaseous flow in sponge structures.

In the case of sponge structures, the magnitude of lateral movement of the fluid element is less compared to that of packed bed structure due to small strut diameter, and so less axial dispersion is found in sponge structures. At low Peclet number, the mechanism of dispersion in a porous structure is mainly dominated by molecular diffusion. Numerous studies on packed beds indicate that at very low Peclet number the contribution of axial mixing is reduced by the tortuous path taken by the fluid element [26, 27, 39, 41, 59, 95], the axial dispersion is related to molecular diffusivity by Eq. (4.38), where τ is the flow tortuosity.

$$D_L = D_m/\tau \tag{4.38}$$

At high Peclet numbers, there is an augmentation of axial dispersion as explained in previous paragraph. Many studies have concluded that for the gas dispersion in packed beds the axial Peclet number of packed beds reaches an asymptotic value of 2 at high Peclet number [5, 39, 97]. In the intermediate region the axial dispersion coefficient is described as the sum of molecular diffusion and random mixing [39].

$$D_L = D_m/\tau + 0.5ud_p \tag{4.39}$$

In Table 4.1 the normalized axial dispersion coefficient values of various sponges at different Peclet number are shown. It is observed that for Ordered Kelvin (OK) structures having similar structural properties (pore density, porosity and specify surface area) as that of alumina (Al_2O_3) sponge, the axial dispersion values are different. The reason for this difference may be due to the fact that the axial flow paths taken by the fluid flowing in the sponges are different and also the spatial velocities.

Table 4.1: The axial dispersion coefficient values of different sponge structures.

Structure name	**Pe_m [-]**	**Pore density [PPI]**	**Real porosity [-]**	**Measured specific surface area [m^{-1}]**	**Nominal pore diameter [m]**	**D_L/D_m**
OK 10 PPI 80% porosity	1891	10	0.823	577.5	0.00508	315.3
Al_2O_3 10 PPI 80% porosity	1360	10	0.82	577.5	0.00508	230.7
	2040	10	0.82	577.5	0.00508	334.6
	2720	10	0.82	577.5	0.00508	446.9
SiSiC 10 PPI 85% porosity	1792	10	0.872	476.3	0.00508	500
OK 20 PPI 75% porosity	686	20	0.769	1144.8	0.00254	138.4
Al_2O_3 20 PPI 75% porosity	677	20	0.769	1146.9	0.00254	207.6
	1015	20	0.769	1146.9	0.00254	315.3
	1354	20	0.769	1146.9	0.00254	423.0
Al_2O_3 20 PPI 80% porosity	769	20	0.82	900.9	0.00254	200
	1154	20	0.82	900.9	0.00254	300
	1538	20	0.82	900.9	0.00254	400
Al_2O_3 20 PPI 85% porosity	758	20	0.845	996.3	0.00254	129.2
	1137	20	0.845	996.3	0.00254	212.3
	1517	20	0.845	996.3	0.00254	280.7
SiSiC 20 PPI 85% porosity	893	20	0.875	647.2	0.00254	461.5

Al_2O_3 30	500	30	0.744	1336.8	0.00169	138.4
PPI 75%	751	30	0.744	1336.8	0.00169	224.6
porosity	1001	30	0.744	1336.8	0.00169	300
Al_2O_3 30	533	30	0.822	1264.9	0.00169	107.6
PPI 80%	800	30	0.822	1264.9	0.00169	169.2
porosity	1068	30	0.822	1264.9	0.00169	223.0
Al_2O_3 30	480	30	0.847	1214.6	0.00169	107.6
PPI 85%	720	30	0.847	1214.6	0.00169	161.5
porosity	961	30	0.847	1214.6	0.00169	215.3
Al_2O_3 45	323	45	0.791	1610.1	0.00113	238.4
PPI 80%	485	45	0.791	1610.1	0.00113	369.2
porosity	647	45	0.791	1610.1	0.00113	500

In Figure 4.9 the axial Peclet number of the simulations done in this study is depicted against the molecular Peclet number and is compared with the various literature results of packed beds (for packed beds the particle diameter is used as characteristic length in calculating the Peclet number). It is observed that the axial Peclet number of the sponge is much higher than the value of 2, the value that is widely reported for packed beds. The reason can be understood by utilizing the mixing-length model proposed by Prausnitz[97] for a packed bed of spheres.

A detailed explanation of the method used in development of the mixing length model is found in [97]. According to the model the axial dispersion coefficient is linearly proportional to the radial random mixing scale l_r, the axial scale of random mixing l_l and the lateral velocity gradient.

$$D_L = l_r l_l \left[\frac{\partial \mathbf{u}}{\partial r}\right] \tag{4.40}$$

For packed bed structures the author reported that the lateral velocity gradient is approximately equal to the ratio of intrinsic pore velocity to the pore diameter. The lateral random mixing scale and the axial random mixing scale were approximated to $\frac{1}{4}d_p$ and $\frac{7}{4}d_p$. Substituting the values, the author was able to arrive at a conclusion that at high Peclet number the axial Peclet number has an approximate value of 2.

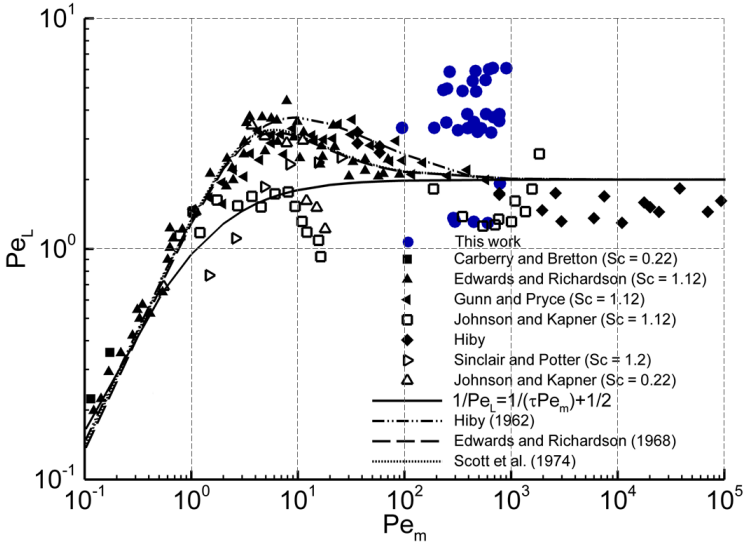

Figure 4.9: Comparison between axial Peclet number of gaseous flow in sponge structure and the correlation presented in literature for packed beds (plotted literature data are taken from Delgado [26]).

In the case of turbulent flows in general, the turbulent eddies create velocity fluctuations with respect to time. Shown in Figure 4.10 are the examples for the longitudinal u_x and the vertical u_y velocities at a point within a turbulent flow. The velocities u_x and u_y vary with respect to time, but in the case where the flow is steady and laminar the time averaged velocities $\overline{u_x}$ and $\overline{u_y}$ equals u_x and u_y, respectively for all time. For turbulent flow, the velocities consists of both mean and turbulent component and by Reynolds' decomposition

$$u_x(t) = \overline{u_x} + u'_x(t) \tag{4.41}$$

$$u_y(t) = \overline{u_y} + u'_y(t) \tag{4.42}$$

The presence of turbulence in flow creates fluctuations in concentration Y too. Similar to the Reynolds' decomposition of the velocity field, the concentration can also be decomposed into temporal mean and

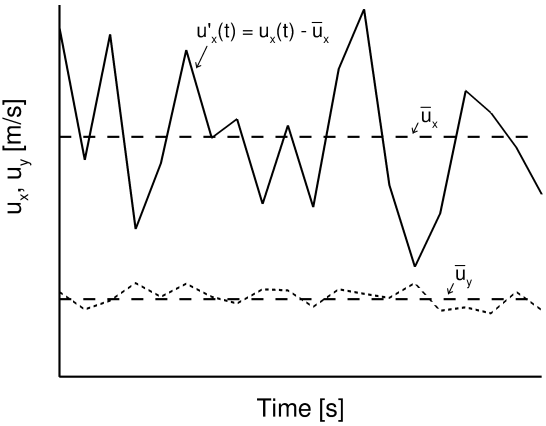

Figure 4.10: Velocities measured at a point in an imaginary turbulent flow.

turbulent fluctuations around the mean

$$Y(t) = \overline{Y} + Y'(t) \tag{4.43}$$

In the case of one-dimensional mass transport equation

$$\frac{\partial Y}{\partial t} + \frac{\partial (u_x Y)}{\partial x} = \frac{\partial}{\partial x} D_m \frac{\partial Y}{\partial x} \tag{4.44}$$

Substituting Eq. (4.43) in Eq. (4.44) gives

$$\frac{\partial (\overline{Y} + Y')}{\partial t} + \frac{\partial (\overline{u_x} + u_x')(\overline{Y} + Y')}{\partial x} = \frac{\partial}{\partial x} D_m \frac{\partial (\overline{Y} + Y')}{\partial x} \tag{4.45}$$

Time averaging each term in Eq. (4.45) gives

$$\frac{\partial \overline{Y}}{\partial t} + \frac{\partial (\overline{u_x}\overline{Y} + \overline{u_x' Y'})}{\partial x} = \frac{\partial}{\partial x} D_m \frac{\partial (\overline{Y} + Y')}{\partial x} \tag{4.46}$$

where by definition, for any transport variable a, $\overline{a'} = 0$ and $\overline{\overline{a}} = \overline{a}$.

The term $\overline{u_x' Y'}$ represents the net mass flux due to turbulent advection. In order to calculate the turbulent flux, fully calculated turbulent field is required, which is computationally intensive and complex.

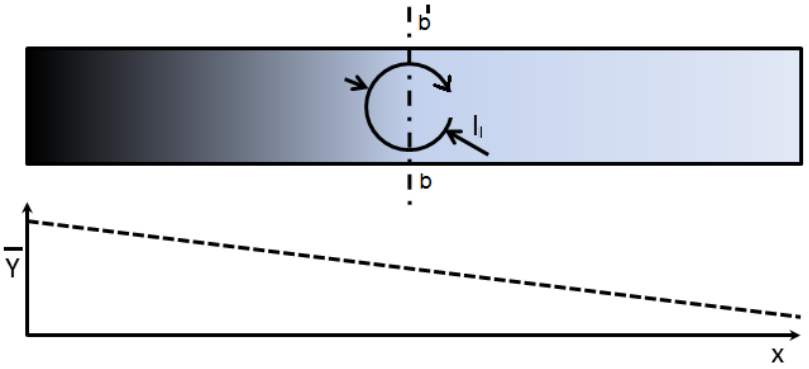

Figure 4.11: Mean concentration along flow.

Generally, a mixing length model is used as an alternative to calculate turbulent flux in terms of mean velocity and concentration, which are easily known. A mixing length model assumes the turbulent motions to be characterized by the length scales of the eddies. Shown in Figure 4.11 is a long narrow tube with linear concentration gradient $\frac{\partial(\overline{Y})}{\partial x} < 0$. There is no mean flow in the tube, i.e., $\overline{u_x} = 0$, considering that the transport is achieved by a single eddy with length scale l_l. At the locations at the top of the eddy, the eddy carries the fluid of higher concentration from left to right. At location $b-b'$, $Y' > 0$ when $u'_x > 0$. Likewise, at locations where $u'_x < 0, Y' < 0$.

The magnitude of the concentration fluctuations is of the scale, $|Y'| \sim l_l \frac{\partial(\overline{Y})}{\partial x}$. The sign of the fluctuation of the concentration depends on the sign of the concentration gradient and also on the sign of the velocity fluctuation. Considering Figure 4.11, for which $\frac{\partial(\overline{Y})}{\partial x}$ is negative, the part of the eddy for which the u'_x is negative produces negative Y' and vice versa. In a case where the concentration gradient is positive, positive u'_x produces negative Y' and negative u'_x produces positive Y'. In general, when $\frac{\partial(\overline{Y})}{\partial x}$ and u'_x have same sign, Y' has an opposite sign of the both, and when $\frac{\partial(\overline{Y})}{\partial x}$ and u'_x have opposite sign, $Y' > 0$. Thus, the sign of Y' is opposite to that of the sign of $u'_x \frac{\partial(\overline{Y})}{\partial x}$. Thus the turbulent

advection generated by an isolated velocity fluctuation u'_x is written as

$$u'_x Y' = -u'_x l_l \frac{\partial \overline{Y}}{\partial x} \tag{4.47}$$

Averaging over a number of random fluctuations associated with many eddies within the system gives

$$\overline{u'_x Y'} = -u'_{x,RMS} l_l \frac{\partial \overline{Y}}{\partial x} \tag{4.48}$$

Eq. (4.48) provides an information that the turbulent flux behaves as a Fickian diffusion. The flux is proportional to the mean concentration gradient, and has an opposite sign. Thus the turbulent diffusion coefficient is modeled as a additional diffusion term

$$D_L = u'_{x,RMS} l_l \tag{4.49}$$

$$\overline{u'_x Y'} = -D_L \frac{\partial \overline{Y}}{\partial x} \tag{4.50}$$

Similarly for other lateral directions, $D_y = u'_y l_y$ and $D_z = u'_z l_z$. The turbulent flux can be modeled as an additional diffusion term

$$\frac{\partial \overline{Y}}{\partial t} + \frac{\partial (\overline{u_x}\overline{Y})}{\partial x} = \frac{\partial}{\partial x}(D_m + D_L)\frac{\partial \overline{Y}}{\partial x} \tag{4.51}$$

In general the turbulent diffusivity D_L is much larger than molecular diffusivity and the latter can be ignored, thus

$$\frac{\partial \overline{Y}}{\partial t} + \frac{\partial (\overline{u_x}\overline{Y})}{\partial x} = \frac{\partial}{\partial x} D_L \frac{\partial \overline{Y}}{\partial x} \tag{4.52}$$

In this study, the flow within the porous matrix is laminar, but the increase in the dispersion can be viewed analogous to that of turbulent flows, where the spatial velocity fluctuation in the case of flow within the porous matrix causes the enhancement in the mass dispersion. In order to find the axial mixing length scale of the sponges, the spatial velocity fluctuations of the flow through sponges are determined. The arithmetic average of the RMS value of the velocity fluctuations in each axial plane is taken as the velocity fluctuation value of the sponge. In

Figure 4.12 the axial and lateral velocity fluctuations are plotted along the axial length for 20 PPI Al_2O_3 75% porosity sponge. By substituting the dispersion coefficient values and the axial velocity fluctuation values in Eq. (4.49), the axial mixing length of the sponges used in this study were determined. From Table 4.2 it is observed that the axial mixing length scales for the sponges are much less compared to the length scale reported in [97], thus sponges have lower dispersion coefficient compared to the packed bed structures.

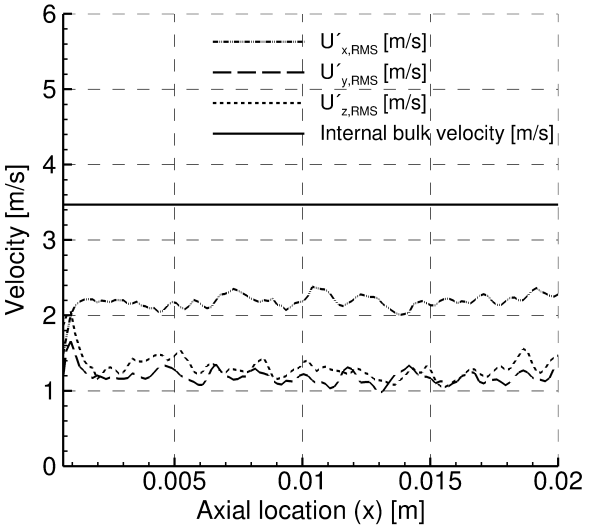

Figure 4.12: Spatial velocity fluctuations of the flow through the 20 PPI 75% porosity Al_2O_3 sponge.

Instead of using the pore diameter as the characteristic length of the sponge in calculating the Peclet number, it is proposed to use the axial mixing length as characteristic length. In Figure 4.13 the axial Peclet number and the molecular Peclet number are calculated using the axial mixing length as the characteristic length, most of the axial Peclet numbers of the sponges lie in a very narrow band. From Figure 4.13 and Table 4.2, it is observed that the axial Peclet number for various sponges used in this study have a value very close to the value

of 2. This justifies our proposal of using the axial mixing length scale as the characteristic length. The axial mixing length scale of most of the sponges used in this study lies within the range $0.27d_{pore}/\varepsilon$ to $0.4d_{pore}/\varepsilon$. Linear fitting of the data for axial mixing length versus pore diameter and specific surface area was done, and the best fit is provided by

$$l_l = d = 0.63 d_{pore}^{-0.54} S_v^{-1.4} \tag{4.53}$$

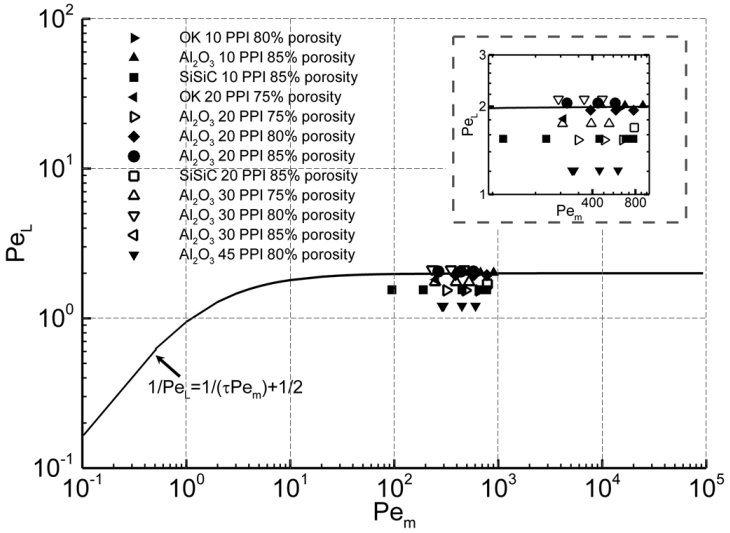

Figure 4.13: Modified axial Peclet number plotted versus modified molecular Peclet number of gaseous flow in sponge (using axial mixing length scale as characteristic length), a magnified view shown in dashed box.

Table 4.2: Axial velocity fluctuation, mixing length scale, modified axial and molecular Peclet numbers (using axial mixing length scale as characteristic length).

Structure name	**Pe_m [-]**	**Internal bulk velocity [m/s]**	**Axial velocity fluctuation [m/s]**	**Mixing length scale [m]**	**Pe_L [-]**
OK 10 PPI 80% porosity	621	4.8	2.46	1.67E-03	2.0
Al_2O_3 10 PPI 80% porosity	465	3.4	1.72	1.74E-03	2.0
	670	5.2	2.61	1.67E-03	2.0
	893	6.9	3.48	1.67E-03	2.0
SiSiC 10 PPI 85% porosity	774	4.5	2.96	2.20E-03	1.5
OK 20 PPI 75% porosity	251	3.5	1.94	9.29E-04	1.8
Al_2O_3 20 PPI 75% porosity	319	3.4	2.26	1.20E-03	1.5
	479	5.2	3.42	1.20E-03	1.5
	640	6.9	4.58	1.20E-03	1.5
Al_2O_3 20 PPI 80% porosity	388	3.9	2.03	1.28E-03	1.9
	581	5.9	3.05	1.28E-03	1.9
	773	7.8	4.07	1.28E-03	1.9
Al_2O_3 20 PPI 85% porosity	265	3.8	1.89	8.89E-04	2.0
	416	5.8	2.97	9.29E-04	1.9
	549	7.7	3.97	9.19E-04	1.9

SiSiC 20 PPI 85% porosity	781	4.5	2.70	2.22E-03	1.7
Al_2O_3 30 PPI 75% porosity	372	3.8	2.21	8.16E-04	1.8
	588	5.7	3.48	8.39E-04	1.7
	745	7.7	4.68	8.34E-04	1.7
Al_2O_3 30 PPI 80% porosity	438	4.1	1.94	7.22E-04	2.1
	658	6.1	2.91	7.56E-04	2.1
	877	8.2	3.89	7.46E-04	2.1
Al_2O_3 30 PPI 85% porosity	228	3.7	1.74	8.03E-04	2.1
	342	5.5	2.61	8.04E-04	2.1
	456	7.3	3.49	8.03E-04	2.1
Al_2O_3 45 PPI 80% porosity	288	3.7	3.08	1.01E-03	1.2
	438	5.5	4.70	1.02E-03	1.2
	584	7.4	6.38	1.02E-03	1.2

The Al_2O_3 sponge with 45 PPI pore density has a considerable deviation from this value, when the sponge structure was examined, we found considerable number of closed pores which leads to flow stagnation points, which in turn alters the flow path and the flow velocity. This structural defect mostly observed in high pore density sponges can be attributed to the reduction in their axial Peclet number. An almost identical value of axial Peclet number, i.e., u/u'_x, implies that all the sponges used in this study have the same magnitude of velocity fluctuation for a given internal bulk velocity, irrespective of the structural parameters. The axial dispersion of a gas flow within a sponge for a given bulk velocity is a function of axial mixing length scale, which in turn is a function of the pore diameter and porosity of the sponge. In order to justify this, a comparison is made between 10 PPI 80% porosity ordered Kelvin structure [52] and corresponding alumina sponge. For a similar molecular Peclet number, the axial dispersion coefficients also have nearly the same value. The u/u'_x is the same for both sponges, the axial dispersion coefficient values are also nearly the same and so the axial mixing length scales do have the same value. As the porosities of the sponges are the same, the axial mixing length

scales are only a function of pore diameter. But in the case of the 20 PPI 75% porosity ordered Kelvin structure and corresponding alumina sponge, the comparison cannot be made as the u/u'_x of the real sponge deviated considerably from 2. This may be due to the presence of structural irregularities, such as wide dispersed values of the pore diameter, presence of closed pore, and variations in strut and node sizes. In this sponge, the presence of large number of pores larger than the nominal pore diameter causes a noticeable change on the flow velocities.

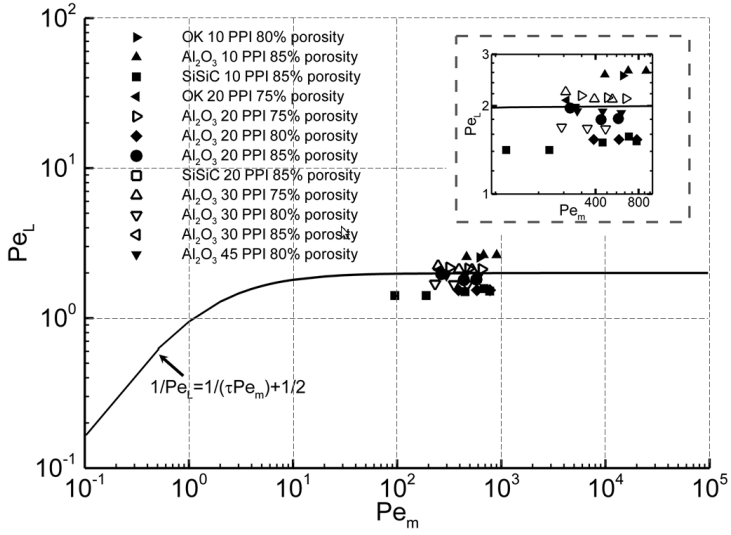

Figure 4.14: Modified axial Peclet number plotted versus modified molecular Peclet number of gaseous flow in sponge (using characteristic length given by Eq. (4.54)), a magnified view shown in dashed box.

In order to relate the axial Peclet number of the sponge with that of the packed bed (for which $Pe_L = 2$), we also provide a characteristic length d for the sponge as a function of pore diameter and tortuosity to calculate the axial Peclet number ($Pe_L = ud/D_L$), by performing a linear fit.

$$d = d_{pore} \times (-4.4 + 4.5\tau) \tag{4.54}$$

The method used in determining the tortuosity of the sponges is described in section 3.3. Shown in Figure 4.14 are the modified Peclet number of sponge structures in comparison to the correlation found in literature for packed beds structures [27]. Tortuosity is not an easy parameter to acquire, so the use of axial mixing length as characteristic length is preferable, especially as modern tomographic methods can be used in measuring flow velocities within the sponge.

Chapter 5

Convective and conduction heat transfer coefficient

In the case of single phase fluid flow through a porous structure, the assumption of local thermal equilibrium is not valid in all engineering applications [2, 3, 88]. For example, in the application of porous media in combustors, there is a significant amount of heat release in the fluid phase, in this case, the local solid and fluid volumes will not be in thermal equilibrium, and when accompanied with interstitial fluid flow within the porous matrix with significantly different thermal properties than that of solid phase, the local change in temperature between the two phases will not be the same. In order to calculate the heat flow in such applications, two energy equations are required to calculate the heat flow in the solid and fluid phases respectively.

Effective heat transport properties of the solid and the fluid phases are required to solve the two energy equations. The solid and the fluid phase energy equations are coupled by convection heat transfer between the two phases with the use of an interfacial convective heat transfer coefficient [68]. In order to obtain an accurate result for the heat transfer in the 2-phase model, apart from the interfacial convective heat transfer coefficient, there is also requirement of effective conductivity for the solid phase and for the fluid phase.

Wakao and Kaguei [116] provide an elaborate description about the

developments in the 2-phase model or 2-equation model. The energy equations of the fluid and the solid phase for a 1D flow through a porous channel are

$$\frac{\partial \overline{T}_f}{\partial t} + \overline{u}\frac{\partial \overline{T}_f}{\partial x} = \frac{1}{\varepsilon}\left(\frac{\overline{k}_f}{(\rho c_p)_f} + D_L\right)\frac{\partial^2 \overline{T}_f}{\partial x^2} + \frac{h_{sf}A_{sf}}{\varepsilon V(\rho c_p)_f}\left(\overline{T}_s - \overline{T}_f\right) \quad (5.1)$$

$$\frac{\partial \overline{T}_s}{\partial t} = \frac{k_{eff}}{(1-\varepsilon)(\rho c_p)_s}\frac{\partial^2 \overline{T}_s}{\partial x^2} - \frac{h_{sf}A_{sf}}{(1-\varepsilon)V(\rho c_p)_s}\left(\overline{T}_s - \overline{T}_f\right) \quad (5.2)$$

where k_{eff} is the effective thermal conductivity of the solid phase (Ref: Section 5.2), D_L is the axial dispersion coefficient (Ref: Chapter 4), h_{sf} the interfacial heat transfer coefficient and A_0 the contact surface area.

5.1 Heat transfer coefficients for open cell ceramics

The two most reliable correlation for convective Nusselt number for packed beds are given by Wakao and Kaguei [116] and Whitaker [118]. Using experimental results from various sources, Wakao and Kaguei [116] provide a correlation for the convective Nusselt number for packed bed of spherical particles as

$$Nu = \frac{h_{sf}d_p}{k_f} = 2 + 1.1Re^{0.6}Pr^{0.33} \quad (5.3)$$

where $Re = u_s d_p/\nu$. Whitaker [118] provided an empirical correlation for packed beds as

$$Nu = 2 + (0.4Re_d^{0.5} + 0.2Re_d^{0.66})Pr^{0.4} \quad (5.4)$$

where $Re_d = \frac{u_s d_h}{\nu(1-\varepsilon)}$, $Nu = \frac{h_{sf}d_p}{k_f}\frac{\varepsilon}{(1-\varepsilon)}$ and $d_h = \frac{6(1-\varepsilon)V}{(A_0}$.

Numerous studies were carried out to determine the interfacial heat transfer coefficient, and in turn to find convective Nusselt number correlations for reticulated porous materials. One of the early experimental measurements of interfacial heat transfer coefficient of ceramic sponges

is done by Younis and Viskanta [121]. The authors studied alumina sponges of pore densities from 10 PPI to 66 PPI of porosity 85% and a cordierite sponge of pore density 20 PPI and porosity 85%. The volumetric heat transfer coefficients between the foam and a stream of air are determined using a single-blow transient technique, in which the flowing fluid was preheated to a set temperature and was made to flow through the sponge sample which was initially maintained at room temperature. The thermocouples installed in the sponge sample were used to record the temperature rise with respect to temperature. The experimental heat transfer coefficients were used to correlate the Nusselt number in terms of the Reynolds number ($Nu = CRe^m$). The authors noticed that with increase in pore diameter the parameters m and C increase and decrease respectively. A least square fitting is done to provide a Nusselt number correlation as

$$Nu = 0.819[1 - 7.33(d/L)]Re^{0.36[1+15.5(d/L)]} \tag{5.5}$$

The correlation is valid under the conditions, 0.005<d/L<0.136 and 5.1 <Re< 564, where d is the pore diameter and L is the length of the porous ceramic. The authors also mention that the heat transfer results of the alumina and cordierite sponge vary considerably, and a separate Nusselt number correlation is provided for cordierite sponge ($Nu = 2.43Re^{0.42}, 65 < Re < 457$). Calmidi and Mahajan [20] studied the convection in high porosity aluminum metal sponges of different pore densities and porosities using air as fluid medium. The Nusselt number is obtained as a function of pore velocity based Reynolds number ($Nu = CRe^{0.5}Pr^{0.37}, Re < 130$). The empirical constant $C = 0.52$ is determined by matching the semi empirical volume-averaged numerical study with the experimental data from the study and also from the literature. Dietrich [31] reported that heat loss assumption by Calmidi and Mahajan between the heated and unheated sections of the porous media in the experiments is not valid. Hwang et al. [64] experimentally studied the high Reynolds number (1900<Re<7800) convective heat transfer in a duct inserted with aluminum sponges of high porosities (0.7, 0.8 and 0.95). The interfacial heat transfer coefficients in the aluminum sponge are determined using a transient single-blow technique with a thermal non-equilibrium two-equation model. Different empirical correlations for the Nusselt number are reported in terms of

pore Reynolds number for different porosities. The authors provide no general correlations that match their experimental data for different sponge porosity.

Ricardson et al. [101] determined the radial convective heat transfer coefficient for 30 PPI alumina sponge of 0.82% porosity. In the experiments, air was passed into a quartz tube containing heated porous sponge, the wall temperature, the inlet and outlet air temperature were measured. The 1D energy equation was solved to match the measured parameters to obtain the radial heat transfer coefficient. The energy balance for a 1D element of the porous bed for any axial position Z is given by

$$d_t G \frac{\mathrm{d}(C_p T)}{\mathrm{d}Z} = h_e[T_w(Z) - T(Z)] \tag{5.6}$$

where d_t is the radius of the reactor, G the gas velocity in kg/m^2/s, C_p the mean specific heat capacity, h_e the average radial heat transfer coefficient, $T_w(Z)$ the wall temperature, and $T(Z)$ the mean bed temperature. The boundary conditions are, $T = T_{in}$ at $Z = 0$ and $T = T_{out}$ at $Z = L$. To calculate the outlet temperature of the first element, $T_1(Z)$, $T_0(Z)$ were set to T_{in} and transformed Eq. (5.6) as

$$d_t G[C_{p,1}T_1(Z) - C_{p,0}T_0(Z)] = h_e[T_w(Z) - 0.5T_1(Z) + T_0(Z)]\Delta Z \tag{5.7}$$

By assuming the value of h_e, Eq. (5.7) was solved, the procedure is repeated for the next element by substituting $T_1(Z)$ for $T_0(Z)$, and the whole procedure is repeated until the final outlet temperature of the bed equal to that of experiment is obtained. To include the effect of radiation in the porous domain, the Nusselt number correlation is given as, $Nu = 2.49 \times 10^{-8} \varepsilon T^3 + 12.6Re$. The size of the porous sponge used in this study is 1.27 cm in diameter and 2.54 cm in length, which may not be enough to neglect the boundary effects.

There are numerous other correlations found in the literature [60, 67, 77, 82, 111, 112, 123]. Most of the Nusselt number correlations provided are for specific sponge and for very low Reynolds numbers. Due to the above reason, the data and the correlations provided are not reliable and cannot be used for calculating the heat transfer in different sponges and for high Reynolds numbers. A comprehensive study of convective heat transfer in various ceramic sponge of different

material, pore density and porosities was done by Dietrich [31]. The sponges made up of alumina, OBSic, Mullit were studied. The Reynolds number of the flow ranges from 50 to 1500. The author developed a universal correlation to predict the heat transfer in different sponges with acceptable accuracy. The approach was based on the well know Generalized Lévêque Equation (GLE) by Martin [86]

$$Nu/Pr^{1/3} = 0.404(2x_f Hgd_h/L)^{1/3} \tag{5.8}$$

where x_f is the frictional fraction of the total pressure drop and L is the length that represent the average distance between two eddy delaminations. Eq. (5.8) is a generalized form of the classical Lévêque heat transfer for a developing thermal boundary layer in a fully developed laminar flow in tubes [78]. The GLE was proposed for packed beds and heat exchangers. The advantage of GLE is that it helps in correlating the Nusselt number in terms of non-dimensional pressure drop (Hagen number). The pressure drop measurements in the sponges are relatively simple, and the GLE helps in calculating the Nusselt number using the pressure drop results. Dietrich [31] conducted transient experiments. The schematic of the experimental set-up is shown in Figure 5.1. In the experiments, the hot fluid (air) was made to pass over the sponges that are initially maintained at room temperature. The fluid and solid temperatures were measured with respect to time.

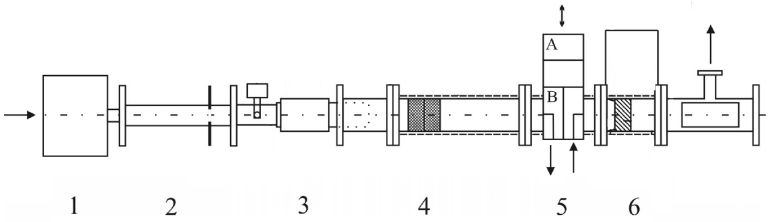

Figure 5.1: The schematic of the experimental set-up: 1-blower, 2-orifice measuring section, 3-heater, 4-flow straighter, 5-valve, 6-sponge sample test section
Source: Dietrich [31]

The inlet solid and fluid temperatures were provided as a boundary condition to one dimensional 2-phase model energy equations. The exit

fluid temperature of the simulation was made to match the experimental results to determine the heat transfer coefficient of the sponge. The author provides a general correlation for ceramic sponges based on the Hagen number as

$$Nu = 0.45Hg^{1/3} \cdot Pr^{1/3} \cdot C_{Re} \cdot C_{geo} \tag{5.9}$$

The author also provides another correlation in terms of the Reynolds number, where the exponent for the Reynolds number is derived from the relation by comparing the Nusselt number dependency on Hagen number ($Nu \sim Hg^{1/3}$) with the Reynolds number dependency on Hagen number ($Re \sim Hg^{1/2}$).

$$Nu = 0.57Re^{2/3} \cdot Pr^{1/3} \cdot C_{Re} \cdot C_{geo} \tag{5.10}$$

Both the correlations are able to predict the Nusselt number within an error range of $\pm 40\%$. The terms C_{Re} and C_{geo} in Eq. (5.9) and Eq. (5.10) are the correction factors. The correction factor C_{Re} was proposed by Martin [86] for calculating heat transfer in an arrangement of inline bundle of tubes. As the GLE over predicted the heat transfer at low Reynolds number, Martin [86] reported that the length L which is equal to the longitudinal pitch for an inline tube bundle arrangement, is not enough to catch the periodically repeating boundary layers in the case of inline bundles. Hence, the length L was modified as $L = pitch/C_{Re}^3$, so that, at very low Reynolds number the length L increases as a function of Re, and for very high Reynolds number it remains same as that of the longitudinal pitch. The use of such correction factor was not required for staggered tube arrangements [86]. The use of the correction factor in Eq. (5.9) and Eq. (5.10) may not be appropriate as the flow inside a reticulated sponge as the matrix structure is not similar to that of flow in an inline bundle of tubes, but resembles more a staggered tube arrangement, in which case the C_{Re} becomes irrelevant. The use of geometric correction C_{geo} is to find an alternative for the d_h/L term in Eq. (5.8), but has no physical justification, and the purpose to use such geometric correction C_{geo} in the study was to unify the heat transfer data collected in the work. In the present study, direct pore simulations are carried out to determine the interfacial heat transfer coefficient h. An attempt is made to find a new correlation for the Nusselt number in terms of the Hagen number based on GLE.

Though the Lévêque equation is developed for the entry region of a tube, it has been proven suitable for the prediction of heat and mass transfer coefficients in packed beds and in the cross corrugated channels of heat exchangers [48, 86]. The GLE's usage is aided by the fact that the thermal and viscous boundary layers are periodically interrupted during the flow through the packed beds and cross corrugated heat exchangers, where the length L represents the average length of the flow path or the average distance between two eddy delimitations [48]. As the axial mixing length l_l is an analogy to the concept of mean free path in thermodynamics, it represents the average length of the flow path before it gets interrupted by a strut or a vortex. It makes physical sense to replace L in Eq. (5.8) by l_l, where l_l is the axial mixing length (4.1). The validity of such a correlation is studied by comparing the correlated Nusselt numbers with that of the Nusselt numbers determined using DPLS simulations.

5.1.1 Numerical setup

Assuming the fluid to be Newtonian fluid having constant densities, the steady flow governing equations of energy conservation is written using Einstein's summation rule as follows:

$$\frac{\partial}{\partial x_j}(\rho c_p u_j T) = \frac{\partial}{\partial x_j}\left(k_f \frac{\partial T}{\partial x_j}\right) \tag{5.11}$$

where x_j and u_j denote the spatial coordinate and velocity in j-direction, T is the fluid temperature, c_p is the fluid specific heat and k_f stands for the conductivity of the fluid. While the mass and momentum conservation equations are given by Eq. (3.27) and Eq. (3.28), respectively. The boundary conditions at the inlet and outlet are specified using constant gas velocity and temperature at the inlet and static pressure together with zero gradient condition for the velocity at the outlet. The domain surfaces perpendicular to the flow direction are given with translational periodic boundary conditions. The structure surfaces were modelled as walls with fixed temperature T_w and no slip boundary conditions. Viscous dissipation is neglected. The schematic of the employed boundary conditions is shown in Figure 5.2.

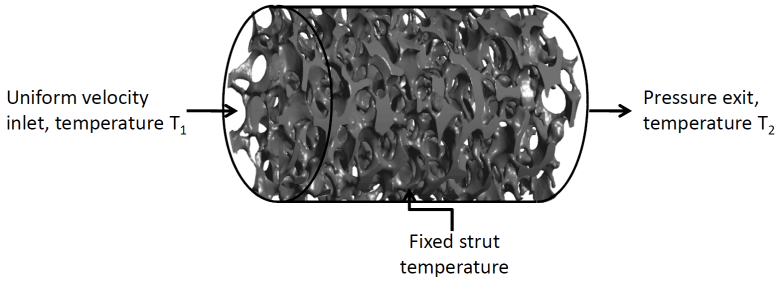

Figure 5.2: Schematic of boundary conditions employed in DPLS of steady state heat convection in porous inert media.

5.1.2 Numerical procedure

In the simulations the solid wall surfaces are fixed at a constant temperature T_w, with the temperature being higher than that of the incoming fluid. The heat from the solid surfaces is then transported by convection and diffusion. In order to calculate an interfacial heat transfer coefficient from a CFD simulation, the three-dimensional temperature fields are reduced into one-dimensional ones using mass flow average over N cross-sectional planes perpendicular to the main flow direction:

$$\overline{T(x_k)} = \frac{\sum_{i=1}^{M} (T_i \cdot \rho u_i A_i(x_k))}{\sum_{i=1}^{M} \rho u_i A_i(x_k)} \tag{5.12}$$

$\overline{T(x_k)}$ denotes the mass flow averaged temperature at the k-th cross-sectional plane at position x_k, $\rho u_i A_i(x_k)$ stands for the mass flow in the plane with the i-th grid cell, M is the number of grid cells and T_i is the temperature value in the i-th grid cell.

5.1.2.1 Determination of interfacial heat transfer coefficient

The simulations were carried for Reynolds numbers 10, 100, 500, 1000 and 1500. The Reynolds numbers ($Re = \rho d_h u_s / \mu$) are calculated using

the hydraulic diameter ($d_h = 4\varepsilon/S_v$) as the characteristics length. The fluid properties used in the simulations are that of air (Pr = 0.7), salt water (Pr = 2) and water (Pr = 6).

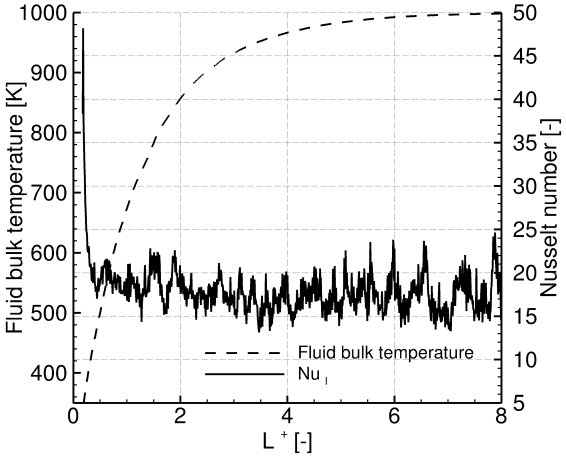

Figure 5.3: The local Nusselt number and fluid bulk temperature as a function of normalized axial length, calculated using DPLS at Re = 500 and Pr = 0.7.

The local heat transfer coefficient in between the axial locations x_k and $x_k + \Delta x_k$ is given as:

$$h_l(x_k) = \frac{\int_{x_k}^{x_k+\Delta x_k} \dot{q}'' \mathrm{d}A_{sf}}{A_{sf}\Delta T_{lm}} \tag{5.13}$$

where $\Delta T_{lm} = \frac{\Delta T_{x_k} - \Delta T_{x_k+\Delta x_k}}{ln\left(\Delta T_{x_k}/\Delta T_{x_k+\Delta x_k}\right)}$ is the log mean temperature difference, while $\Delta T_{x_k} = T_w - \overline{T}(x_k)$. In Figure 5.3 the local Nusselt number $Nu_l = \frac{h_l d_h}{k_f}$ and fluid bulk temperature of a 20 PPI 75% porosity alumina sponge are plotted against the normalized axial distance $L^+ = L/d_{pore}$. The plot is for a simulation with air as fluid medium. It is seen that, except in the locations near to the entrance, the Nusselt number values are nearly constant along the axial direction. The

slight fluctuations in the Nusselt number values are due to the statistical random nature of the porous media. Neglecting the peak values near the entrance, the arithmetic average of the Nusselt numbers along axial locations is taken as the average Nusselt number Nu of the porous media.

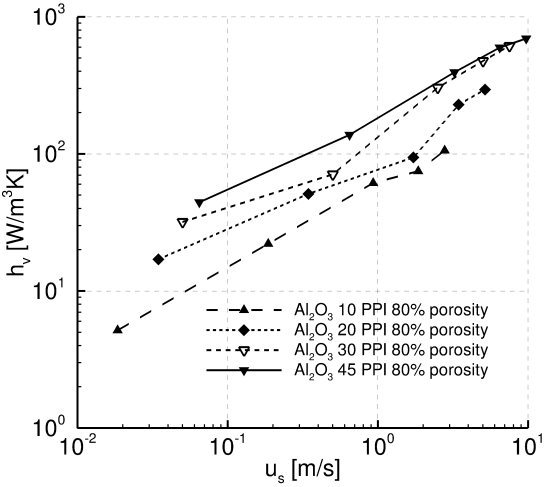

Figure 5.4: DPLS determined volumetric heat transfer coefficients against the superficial velocity for different alumina sponges with different pore density and with same porosity (Pr = 0.7).

In Figure 5.4, plotted are the volumetric heat transfer coefficients versus superficial velocity for alumina sponges of 80% porosity having different pore densities calculated using air as fluid medium. It is seen that the volumetric heat transfer coefficients increase with increase in pore density. The same tendency is reported by Younis et al. [121] and Dietrich [31]. It is discussed in [121], that the increase in pore densities decrease the pore diameter, which in turn increase the specific surface area of the sponge, given that the porosities remain the same. It becomes obvious that the increase in the specific surface area increase the volumetric heat transfer coefficient. It denotes that the 45 PPI sponge will transfer more heat to the flowing fluid in comparison to the 10 PPI sponge, given that the volumes remain the same.

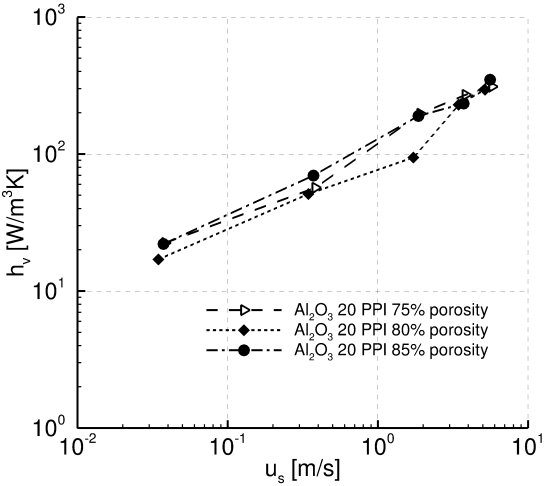

Figure 5.5: DPLS determined volumetric heat transfer coefficients against the superficial velocity for 20 PPI alumina sponges with different porosities (Pr = 0.7).

Plotted in Figure 5.5 are the volumetric heat transfer coefficients of 20 PPI sponges having different porosities. It can be noticed that the influence of porosity on the heat transfer coefficients is not quantifiable and it is a similar conclusion that is reported in literature [31, 48, 121]. Shown in Figure 5.6 is the comparison of numerically calculated interfacial heat transfer coefficients with the experimental interfacial heat transfer coefficients [31] for similar sponges as the ones used in this study. The results' trend and values make a reasonable comparison with those of the experiments.

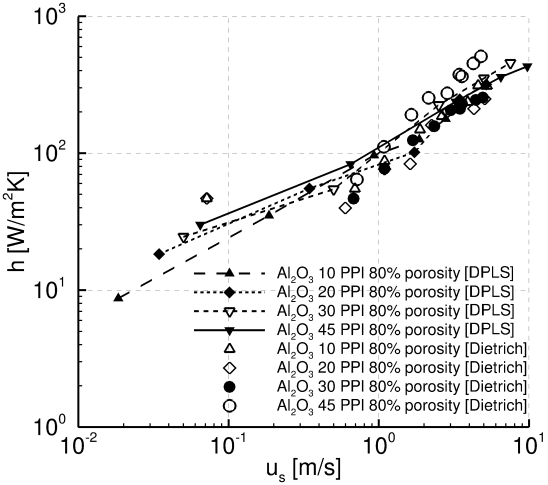

Figure 5.6: Comparison of DPLS determined heat transfer coefficients with that of experiments (Pr = 0.7).

In Figure 5.7, the interfacial heat transfer coefficients h of various sponges used in this study are plotted against the superficial flow velocity u_s. It is seen that the material and the structural properties of the sponges have little or no considerable impact on the heat transfer coefficient. This is similar to the observations that are found in the literature[31, 48].

In Figure 5.8, are the Nusselt numbers of the sponges to the corresponding Hagen number. The plot contains values for the simulations with fluids having three different Prandtl numbers (Pr = 0.7, 2 and 6). Though the results are scattered, through an arithmetic regression of all the data, it is found that the results have nearly a linear trend with respect to $Hg^{1/3}$ (the actual exponent for Hg obtained through regression being 0.34). The goodness of the fit is found using R-squared value, which is about $R^2 = 0.97$. However, due to scattered data, nearly 18% of the data are above the relative error of 35% and the maximum being 59%. Even for packed beds the Nusselt number correlation in terms of the Hagen number has errors around 38% [49], so for sponges, given their structural complexity and manufacturing difficulty in replicating

similar structures, having error range within 38% will be acceptable.

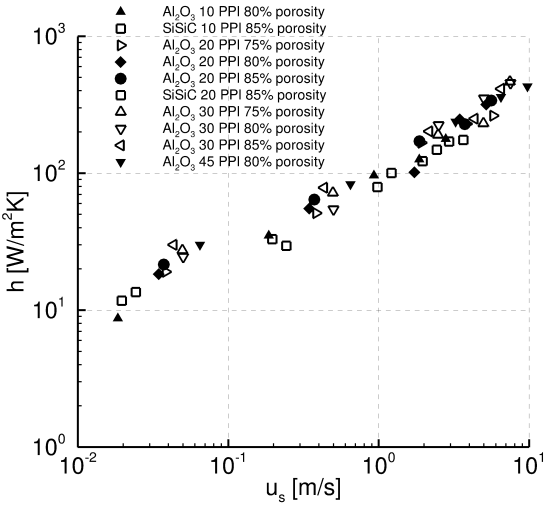

Figure 5.7: Comparison of the DPLS determined heat transfer coefficients for alumina and SiSiC sponges (Pr = 0.7).

In order to correlate the Nusselt number to the Hagen number, the generalized Lévêque equation is used in this study. For the packed beds and periodically repeating structures, Martin [86] proposed correlations for L in Eq. (5.8) in terms of porosity and hydraulic diameter. But in the case of reticulated structures, the length L has not yet been defined in the literature [48]. As there is no correlation available for L for reticulated structures, Dietrich [31] and Garrido [48] used correction factors to correlate their heat transfer coefficients and mass transfer coefficients to the pressure drop. As discussed earlier, the length L represents the average distance between the two eddy boundaries for a flow within the sponges, or the length of the flow without interruption. In this study, L is replaced by l_l, as it represents the average length of the flow path before it gets interrupted by a strut.

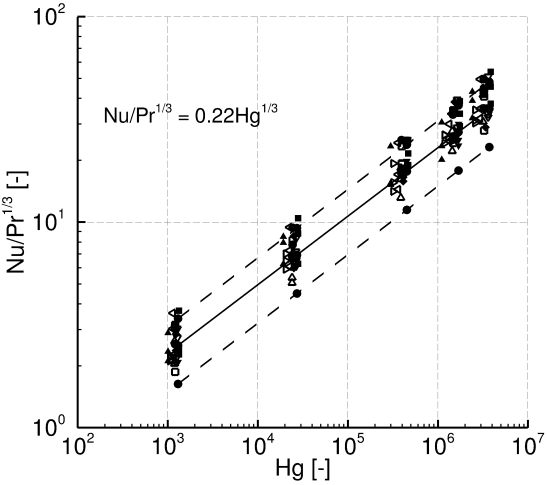

Figure 5.8: Lévêque analogy for all sponge structures used in this study, dashed lines indicate ±35% error band (fluid Prandlt numbers Pr = 0.2, 2 and 6.).

In Figure 5.9, the new correlation (Eq. (5.14)) values are plotted against the Hagen number. It can be seen that the new correlation was able to bring down the error values within a range of ±35%, which is much better than the error range of ±40% for a GLE based general correlation found in the literature for ceramic sponges [31]. Though the correlation (Eq. (5.14)) works better for the DPLS values, the use of such correlation requires the knowledge of axial mixing length values of the sponge, which is nearly impossible to find using simple experiments. Here in this study, a relation between the axial mixing length and the structural properties such as pore diameter and specific surface area is provided (Eq. (4.53)), but again the relation is specific to the sponges used in this study.

$$Nu = 0.17(Prd_h/L_dHg)^{1/3}, \text{where } L_d = l_l \tag{5.14}$$

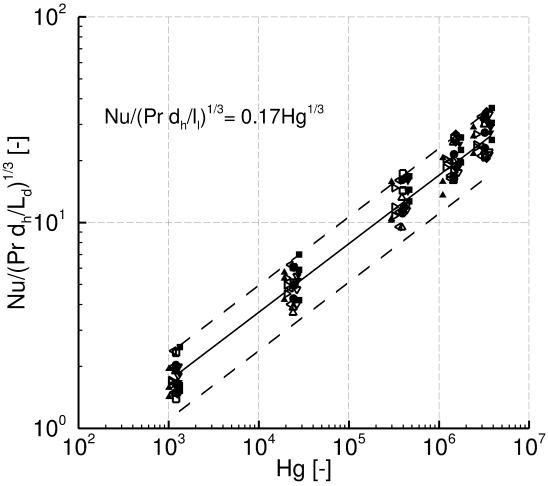

Figure 5.9: Lévêque analogy for all sponge structures used in this study, dashed lines indicate ±35% error band (fluid Prandlt numbers Pr = 0.2, 2 and 6.), with $dh/L = dh/l_l$

5.2 Effective thermal conductivity

Numerous theoretical and experimental studies have been carried out to determine the effective thermal conductivity of porous media [36, 66, 68, 113]. The studies provide a number of empirical, semi-empirical and theoretical models to calculate the effective conductivity of the porous media, and are applicable to specific material, structure and temperature range. Fu et al. [43] grouped the thermal conductivity models into the following groups: 1. pure stagnant conductance 2. Stagnant thermal conductance with thermal dispersion (convection) 3. Stagnant conduction with radiation, and finally, 4. Stagnant conduction, radiation and convection. In most of the literature, the pure stagnant conduction is studied, and the effect of radiation and local dispersion near the strut walls are usually accounted separately. In the case of thermal equilibrium between the fluid and the solid struts or particles, there are many macroscopic 2-phase effective conductivity models that exist. There are two main approach followed by several groups in de-

veloping the models to determine the effective conductivity [73], the macroscopic 2-phase approach and the micro structural approach. In the case of packed bed of spherical particles the macroscopic approach is widely used and the microscopic structural analysis is used in the study of reticulated porous structures. The simplest models in the case of the macroscopic approach are the parallel and the series models [68],

$$k_{eff(2phase)} = \varepsilon_1 k_1 + (1 - \varepsilon_1) k_2 \tag{5.15}$$

$$k_{eff(2phase)} = \frac{1}{\varepsilon_1 / k_1 + (1 - \varepsilon_1)/k_2} \tag{5.16}$$

In the first case, the fluid and the solid are assumed to be parallel to the heat flow, and in the second case they are assumed perpendicular to the heat flow. In the case of the parallel model, most of the heat flows straight through the high conductivity regions thus forming the upper bound for the thermal conductivity in porous media, and in the case of the series model, the heat flow cannot avoid the low conductivity region, thus forming the lower bound. Maxwell-Eucken [87] developed models for non continuous media and thus tightening the upper and lower bound for porous media.

$$k_{eff(2phase)} = k_1 \frac{2k_1 + k_2 - 2(k_1 - k_2)\varepsilon_2}{2k_1 + k_2 + (k_1 - k_2)\varepsilon_2} \tag{5.17}$$

$$k_{eff(2phase)} = k_2 \frac{2k_2 + k_1 - 2(k_2 - k_1)(1 - \varepsilon_2)}{2k_2 + k_1 + (k_2 - k_1)(1 - \varepsilon_2)} \tag{5.18}$$

Eq. (5.17) is suitable for media in which the conductivity of the continuous phase is higher than that of the dispersed phase. Eq. (5.18) is more suitable for media in which the continuous phase is lower than that of the discontinuous phase (packed beds). Landauer [75] derived an equation for effective conductivity for a matrix of random mixtures of two materials based on effective medium theory (EMT). This model is suitable when one component has higher thermal conductivity compared to the other, and the components are randomly distributed. Krischer [70] recommended a model based on the weighted harmonic mean of the serial and the parallel models for the effective thermal conductivity of heterogeneous materials, which is given by,

$$k_{eff(2phase)} = \frac{1}{(e/k_{series}) + (1 - e)/k_{parallel}} \tag{5.19}$$

where e is the empirical weighting parameter for the weighted harmonic mean model and is specified for each material and porosity. In the case of the micro structural analysis, the unit cell approach has been widely used. Due to the periodical nature of the porous media, the unit cell approach is considered to be valid. In the unit cell approach, the resistance to heat flow through solid struts, particles and fluid are analyzed individually, and are used to calculate the effective thermal conductivity based on serial or parallel models. Hsu et al. [61] studied a unit cell made of inline touching cubes, the authors proposed a one dimensional model for effective thermal conductivity. The model has a good agreement with the experimental values of packed beds. Fu et al. [43] developed two representative unit cell models, one with a cubic unit cell and other with a hallow sphere in a cube to predict the stagnant effective thermal conductivity of cellular ceramics using the thermal-circuit method. Both the models provide a reasonable prediction of the effective conductivity. The authors reported that the models are not critically assessed for intermediate and for high temperatures. Calmidi and Mahajan [19] experimentally investigated highly porous metal sponges with air and water as fluid medium. They proposed a theoretical model based on a two dimensional array of hexagonal structure of the metal sponge matrix with square lump nodes. The model matches well with their experimental results for a ratio of cross-section area of strut to intersection area of 0.09. Bhattacharya et al. [11] extended the model by Calmidi and Mahajan [19], replacing square nodes with circular nodes obtained an area ratio of 0.19. The model predicts the effective conductivity well for aluminum metal sponges, but overestimates the values for other sponges. Edouard [37] used a pentagonal dodecahedron structural model to study the effective conductivity of reticulated sponge. The author assumes either slim or fat description of the strut depending upon the sponge porosity, i.e., slim for sponge with porosities less than 90%, and fat for sponge with porosities more than 90%. The author compared the model results with that of experimental results of sponges with porosities between 75% to 85% [30], and reported that the fat strut model gives a good agreement and the error values vary between 16% to 23%. Boomsma and Poulikakos [15] proposed a model based on 3-D tetrakaidecahedron geometry with cubic nodes. The experimental values were used to find a non dimensional

fitting parameter $e = \frac{\text{cubic node length}}{\text{ligament length}} = 0.16$. The model is not valid for porosities above 90%. Dietrich et al. [30] proposed a model for effective conductivity of ceramic sponges similar to the sponges that are used in this study. The model was based on the Krischer and Wast model [71]. In the study by Dietrich et al. [30], the microscopic intrinsic solid phase thermal conductivity of the ceramic sponges are measured experimentally, and are used to replace the solid conductivity of the ceramic material. This is a significant difference from all other models that are found in literature, in which the material conductivity of the ceramic or metal at their natural state is considered, neglecting the change in conductivity due the difference in micro structure of the sponge material in comparison to their naturally occurring form. In recent years, the three dimensional simulations based on real structure and Kelvin structure are used to determine the effective thermal conductivity [14, 73]. The calculations are done using simple resistor network model [14, 115] or by using full foam geometry [62, 72]. In this study, the three dimensional foam structures are used to determine the solid thermal conductivity of the solid structure (excluding the saturated fluid medium). This effective solid conductivity is the property that is required in the 1-D solid energy equation (Eq. (5.2)). A term called solid tortuosity is determined for each sponge, and the parallel model (Eq. (5.15)) is used to calculate the 2-phase effective conductivities to compare them with that of experimental results [30].

5.2.1 One dimensional heat conduction

The steady-state one dimensional heat flux due to conduction in any media can be calculated using Fourier's law of heat conduction

$$q'' = -k_s \frac{\mathrm{d}T}{\mathrm{d}x} \tag{5.20}$$

where k is the material thermal conductivity. For a constant thermal conductivity k and for a temperature difference of ΔT, the Fourier's heat equation can be written in terms of resistance to heat flow

$$q'' = -\frac{\Delta T}{R} \tag{5.21}$$

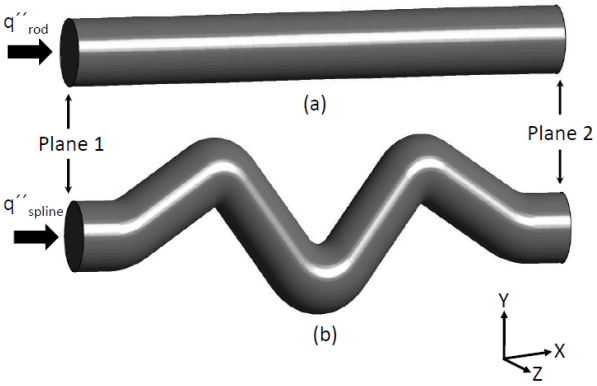

Figure 5.10: Schematic of steady-state heat conduction in solid rods: (a) heat flow in a straight solid, (b) heat flow in a solid rod with bends.

where $R = \Delta x/k_s$ is the thermal resistance. The thermal resistance is proportional to the length parallel to the path taken by the heat flow and is inversely proportional to the thermal conductivity of the material. For a solid rod as shown in Figure 5.10(a), the length x is the distance between the two planes at position 1 and position 2, but for a rod as shown in Figure 5.10(b), though the distance between the two planes remains the same, the path taken by the heat to flow from plane 1 to plane 2 is increased due to the structural profile of the rod. The increase in the path taken by the heat to flow from plane 1 to plane 2 can be accounted into the resistance by use of the term solid tortuosity τ_s

$$\tau_s = \frac{\text{actual distance taken by heat to flow}}{\text{distance between plane 1 and plane 2}} \tag{5.22}$$

The heat resistance R can be expressed in terms of tortuosity τ_s, distance Δx and thermal conductivity k as

$$R = \tau_s \frac{\Delta x}{k} \tag{5.23}$$

With the use of Eq. (5.23), the effective conductivity k_{eff} of the rod in Figure 5.10(b) can now be used in Eq. (5.20)

$$q'' = -k_{eff}\frac{\Delta T}{\Delta x} \tag{5.24}$$

where the effective conductivity $k_{eff} = k/\tau_s$, the effective conductivity depends on the material conductivity of the rod and also on the structural profile of the rod.

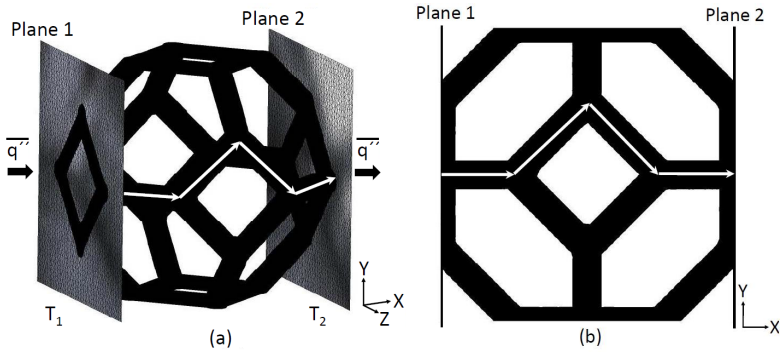

Figure 5.11: Schematic steady-state heat conduction in a Kelvin structure in a particular orientation, with temperature boundary conditions on plane 1 and plane 2, and adiabatic boundary condition on the remaining Cartesian planes.

Similarly, in the case of porous structures the effective conductivity of the solid structure is less than that of the material conductivity due to the increase in the path taken by the heat to flow for a given distance. In order to check the above assumption, a test case was validated using a tetrakaidecahedron structure (ordered Kelvin structure) with equal strut lengths. The tetrakaidecahedron structure is the idealized shape that resembles the reticulated porous structures. The topology of the Kelvin structure that is used for this case is well defined. Figure 5.12 is a schematic representation of a strut of a pore in the case of ordered Kelvin structure. From Figure 5.12 the tortuosity of the strut can be calculated using trigonometry, which is $\sqrt{2}$. Thus, the heat flow path

in the case of ordered Kelvin structure should be approximately equal to $\sqrt{2}$ times the distance.

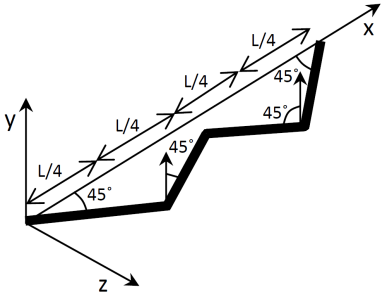

Figure 5.12: Schematic steady-state heat conduction in a Kelvin structure in a particular orientation, with temperature boundary conditions on plane 1 and plane 2, and adiabatic boundary condition on the remaining Cartesian planes.

Direct pore level simulations were performed to determine the effective conductivity of solid phase of the Kelvin structure with the orientation as shown in Figure 5.11. The temperature at plane 1 and 2 are fixed and an adiabatic boundary condition is imposed on all other Cartesian planes. The average heat flux value is obtained from the simulation. For a fixed conductivity k_s, the effective conductivity can be obtained using (5.25).

$$k_{eff} = \frac{k}{\tau_s} \tag{5.25}$$

From the effective conductivity value, the solid tortuosity can be obtained using Eq. (5.23). The calculated value of the solid tortuosity of the simulated Kelvin structure was 1.39, which is slightly less than $\sqrt{2}$, the reason may be that at the nodal points the path taken by the heat to flow may not be as sharp as in Figure 5.11. In the case of the Kelvin structure, the structural tortuosity remains the same for different PPI and the solid tortuosity will also remain nearly the same. The porosity of the Kelvin structure can be increased or decreased only by increasing or decreasing the strut diameter, but the change in strut diameter does

not change the average heat flux $\bar{q}''$, though there is a change in the net heat flow. As the heat flux remains the same and also the solid tortuosity, the effective conductivity should not vary with a change in PPI and porosity.

In order to determine the solid tortuosity of the real sponges, direct pore level simulations were performed with the boundary conditions as mentioned above in the case of Kelvin structure. The schematic diagram of the sponge structure with the employed boundary conditions is shown in Figure 5.13.

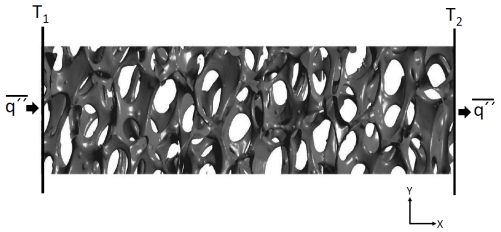

Figure 5.13: Schematic of steady-state heat conduction in a sponge, with temperature boundary conditions on plane 1 and plane 2, and adiabatic boundary condition on the remaining Cartesian planes.

Table 5.1: Solid phase effective conductivities of alumina sponges (considering the alumina material conductivity to be 18 W/mK)

sponge	**Porosity(%)**	$\mathbf{k_{eff}}$	**Tortuosity**(τ_s)
10 PPI Al_2O_3	80	6.50	2.7
20 PPI Al_2O_3	75	8.20	2.2
	80	9.62	1.8
	85	6.09	2.9
30 PPI Al_2O_3	75	6.29	2.8
	80	7.00	2.5
	85	7.01	2.5
45 PPI Al_2O_3	80	6.44	2.8

Table 5.2: Solid phase conduction tortuosity of alumina sponges

RMS	2.6
STD.DEV	0.37

The calculated solid phase effective conductivities are tabulated in Table 5.1 and Table 5.3. From Table 5.1 it is seen that the effective thermal conductivities of alumina sponges are nearly the same for different pore densities and porosities. The slight difference in the magnitudes may be due to the difference in number of nodes because of the difference in pore density and also the structures used may not have exactly similar structure to yield exactly same solid tortuosity.

Table 5.3: Solid phase effective conductivities of SiSiC sponges (considering the SiSiC material conductivity to be 145 W/mK)

Sponge	**Porosity(%)**	$\mathbf{k_{eff}}$	**Tortuosity(τ_s)**
10 PPI SiSiC	85	38.6	3.7
20 PPI SiSiC	85	36.76	3.9

In Table 5.3, the effective thermal conductivities of SiSiC sponges with two different pore densities and with the same porosity are tabulated. In Table 5.2, the RMS of the solid tortuosity values of alumina sponges is tabulated. The solid tortuosity of the two SiSiC sponges is approximately 3.8. The solid tortuosity of alumina sponges and the solid tortuosity of SiSiC sponges differ in their magnitudes, which is due to the structural difference between the alumina and SiSiC sponges. The material and manufacturing process of the sponge have a strong influence on the structure of the sponge and so the solid tortuosity.

5.2.1.1 Two phase stagnant effective conductivity

The two phase effective conductivities are the values that are reported in the literature. So in order to compare the use of solid conduction tortuosity to find the solid effective thermal conductivity of the sponge with that of the experiments, there is a need to find the two phase

stagnant effective conductivity of the sponges, i.e., the conductivity of the sponge including the stagnant fluid phase.

Table 5.4: Comparison of 2-phase phase effective conductivities of alumina sponges with that of experiments [30]

Sponge	$\mathbf{k_{eff(2phase)}}$	**Experimental** $\mathbf{k_{eff(2phase)}}$	**Error(%)**
10 PPI Al_2O_3 80% porosity	1.9	2.6	27.0
20 PPI Al_2O_3 75% porosity	3.0	3.4	10.8
20 PPI Al_2O_3 80% porosity	2.8	2.7	3.7
20 PPI Al_2O_3 85% porosity	1.3	2.0	31.7
30 PPI Al_2O_3 80% porosity	2.1	2.8	21.9
45 PPI Al_2O_3 80% porosity	1.9	2.8	30.7

As the increase in resistance to the flow of heat through the solid phase of the sponge is calculated using the solid tortuosity, and the solid and the fluid phase being continuous, the two phase effective conductivity can be found using the simple parallel model (Eq. (5.15)). In Eq. (5.15), the conductivity k_2, is the solid effective conductivity k_{eff} and k_1 is the fluid conductivity k_f, which is the property of the fluid. The values of k_{eff} and k_f are dependent on the temperature, and so, the two phase stagnant effective conductivity is also a function of temperature. In the case of ceramics, the conductivity increase with increase in temperature and the change in the conductivity of fluid is less in comparison to that of ceramics, while from Eq. (5.15) it can be seen the influence of fluid conductivity on the two phase effective conductivity is less in comparison to that of solid. In general, the two phase effective conductivity increases with an increase in temperature.

In the case of porosity, when there is an increase in porosity the conductivity decreases due to the decrease in the influence of k_2 in Eq. (5.15), which is the same influence that is reported in literature [30].

In this study, the results are compared with those of Dietrich [30]. The value of conductivity k used in Eq. (5.25) to calculate the solid effective conductivity is the intrinsic conductivity of alumina [30] ($k = 26.8W/mK$) at $25°C$. With $k = 26.8W/mK$, $k_f = 0.03W/mK$ and with τ_s from Table 5.4, the two phase effective conductivities using Eq. (5.15) are provided in Table 5.4 along with the experimental results and their relative errors. Though the maximum relative error is about 31.7%, it is expected given the complexity in the structure and the problem in exactly replicating the sponges used in the experimental study. In the literature, the models for ceramic sponges have maximum error values of about 23% [37] and 45% [30]. It is also reported in [30], that even for a small change in the solid material conductivity (about 5 W/mK) the authors model had the error value changed to around 8%.

Chapter 6

Radiative heat transfer

All substances in the universe continuously emit or absorb radiation in the form of electromagnetic waves or photons by virtue of their internal energy. The internal energy is proportional to the temperature of the substance, and thus the radiation is dependent on the temperature. In the case of convection and conduction, the heat transfer between two locations is dependent on the first power of the temperature difference of the locations. But the thermal radiative heat transfer between two bodies depends on the difference between the absolute temperature of the bodies, each raised to the fourth power [89, 108]. Because of this basic difference between the radiation and the other two modes of heat transport, the contribution of radiation is substantial, particularly at very high temperatures. The fundamentals of continuum treatment in a participating media can be found in standard radiative heat transfer texts. In the continuum treatment, the radiation transfer equation (RTE), i.e., Eq. (6.17), is used to quantify the change in the spectral radiative intensity I_λ along a given direction $\hat{s}$ at any location inside a participating medium. In a radiatively participating medium, any radiative beam is continuously attenuated by absorption and scattering while it travels through the medium, as schematically shown in Figure 6.1.

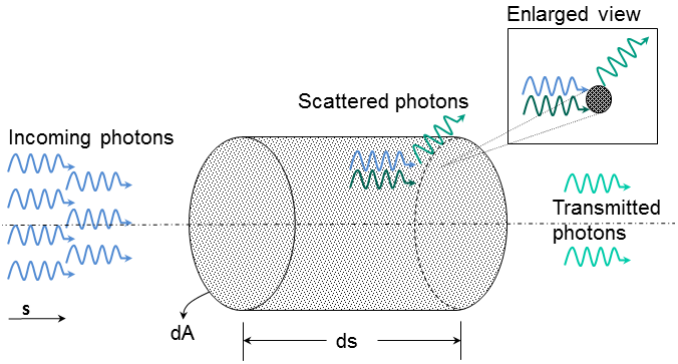

Figure 6.1: Attenuation of radiative intensity by absorption and scattering.

In the case of a medium with constant refractive index, the electromagnetic waves travel in a straight line, and for a stationary, non polarizing medium under thermodynamic equilibrium the absolute amount of absorption of the radiative intensity by the medium is proportional to the incident energy and as well as the distance travelled by the beam

$$(\mathrm{d}I_\lambda)_{abs} = -\kappa_\lambda I_\lambda ds \tag{6.1}$$

where I_λ is the radiative energy flux per unit solid angle and wavelength and κ is the proportionality constant, which is also known as the linear absorption coefficient. Integrating Eq. (6.1) over the geometric path s gives

$$\frac{I_\lambda(0) - I_\lambda(s)}{I_\lambda(0)} = 1 - exp\left(-\int_0^s \kappa_\lambda \mathrm{d}s\right) \tag{6.2}$$

where $I_\lambda(0)$ is the incoming beam intensity. The term $\int_0^s \kappa_\lambda \mathrm{d}s$ in Eq. (6.2) is called the optical thickness of the medium.

Similarly, the incoming beam is also attenuated due to scattering by the medium. Unlike absorption, in which case the incident energy is partially or fully absorbed by the medium and converted to internal energy. In the case of scattering the, the scattered energy is redirected into all other directions, thus augmenting the energy in the scattered direction, which is known as "in-scattering" in the scattered direction.

The reduction of incoming beam intensity traveling in direction s is given by

$$(\mathrm{d}I_\lambda)_{scat} = -\sigma_\lambda I_\lambda ds \tag{6.3}$$

where σ_λ is the proportionality constant, which is the linear scattering coefficient for scattering from the pencil of rays under consideration into all other directions. The total attenuation of the intensity in a pencil of rays by both absorption and scattering is considered as extinction.

$$\frac{I_\lambda(0) - I_\lambda(s)}{I_\lambda(0)} = 1 - exp\left(-\int_0^s \beta_\lambda \mathrm{d}s\right) \tag{6.4}$$

Thus, the extinction coefficient of the medium is defined as

$$\beta_\lambda = \kappa_\lambda + \sigma_\lambda \tag{6.5}$$

The total optical thickness is defined as

$$\tau_\lambda = \int_0^s \beta_\lambda \mathrm{d}s \tag{6.6}$$

The beam travelling into the medium in direction $\hat{s}$ is not only attenuated by the medium, but also augmented by the scattered energy in direction $\hat{s}$ from other directions and also by the emission in direction $\hat{s}$ by the medium itself. The rate of emission from a volume element is proportional to the magnitude of the volume, and so, the emitted intensity along any path is proportional to the length of the path and to the local energy possessed by the medium. In the case of thermodynamic equilibrium, the intensity must be equal to the blackbody intensity, thus

$$(\mathrm{d}I_\lambda)_{em} = \kappa_\lambda I_{b\lambda} ds \tag{6.7}$$

where κ_λ is the proportionality constant which is same as that of absorption. Combining Eq. (6.1) and Eq. (6.7) provides

$$(\mathrm{d}I_\lambda)_{em} = \kappa_\lambda (I_{b\lambda} - I_\lambda) ds \tag{6.8}$$

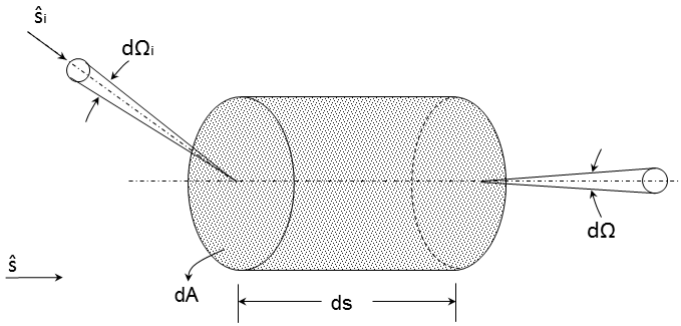

Figure 6.2: Redirection of radiative intensity by scattering.

The total incoming energy in direction $\hat{s}_i$ falling on area $\mathrm{d}A$ in Figure 6.2 is given by

$$I_\lambda(\hat{s}_i)(\mathrm{d}A\hat{s}_i \cdot \hat{s})\mathrm{d}\Omega_i\mathrm{d}\lambda \tag{6.9}$$

As per Eq. (6.3) the total scattered energy while the energy travels through volume $\mathrm{d}V$ for a distance $\mathrm{d}s/(\hat{s}_i \cdot \hat{s})$ is given by

$$\sigma_\lambda(I_\lambda(\hat{s}_i)(\mathrm{d}A\hat{s}_i \cdot \hat{s})\mathrm{d}\Omega_i\mathrm{d}\lambda)\frac{\mathrm{d}s}{\hat{s}_i \cdot \hat{s}} = \sigma_\lambda I_\lambda(\hat{s}_i)\mathrm{d}A\mathrm{d}\Omega_i\mathrm{d}\lambda\mathrm{d}s \tag{6.10}$$

Of this scattered energy, only a portion of it is scattered in direction $\hat{s}$, the probability of which is given by Φ_λ, which is the scattering phase function. The constant 4π is arbitrary, and its importance will be discussed later. The amount of energy scattered in direction $\hat{s}$ is then

$$\sigma_\lambda I_\lambda(\hat{s}_i)\mathrm{d}A\mathrm{d}\Omega_i\mathrm{d}\lambda\mathrm{d}s\left(\frac{\Phi_\lambda(\hat{s}_i, \hat{s})}{4\pi}\right) \tag{6.11}$$

The amount of energy scattered into direction $\hat{s}$ from all incoming directions is given by

$$(\mathrm{d}I_\lambda)_{scat}(\hat{s})\mathrm{d}A\mathrm{d}\Omega\mathrm{d}\lambda = \int_{4\pi} \sigma_\lambda I_\lambda(\hat{s}_i)\mathrm{d}A\mathrm{d}\Omega_i\mathrm{d}\lambda\mathrm{d}s\Phi_\lambda(\hat{s}_i, \hat{s})\frac{d\Omega}{4\pi} \tag{6.12}$$

thus

$$(\mathrm{d}I_\lambda)_{scat}(\hat{s}) = \mathrm{d}s\frac{\sigma_\lambda}{4\pi}\int_{4\pi} I_\lambda(\hat{s}_i)\Phi_\lambda(\hat{s}_i, \hat{s})\mathrm{d}\Omega_i \tag{6.13}$$

From Eq. (6.11) the energy scattered in all directions from solid angle $\mathrm{d}\Omega_i$ is

$$\sigma_\lambda I_\lambda(\hat{s}_i)\mathrm{d}A\mathrm{d}\Omega_i\mathrm{d}\lambda\mathrm{d}s\frac{1}{4\pi}\int_{4\pi}\Phi_\lambda(\hat{s}_i,\hat{s})\mathrm{d}\Omega \tag{6.14}$$

This should be equal to Eq. (6.10), which results in

$$\frac{1}{4\pi}\int_{4\pi}\Phi_\lambda(\hat{s}_i,\hat{s})\mathrm{d}\Omega = 1 \tag{6.15}$$

If an equal amount of energy is scattered in all directions, then $\Phi_\lambda = 1$, and this explains the inclusion of constant 4π in Eq. (6.11)

The augmentation due to scattering in a particular direction has contributions from all directions. The energy flux scattered into the direction $\hat{s}$ from all incoming directions $\hat{s}_i$ is given by

$$(\mathrm{d}I_\lambda)_{scat} = \mathrm{d}s\frac{\sigma_{s\lambda}}{4\pi}\int_{4\pi} I_\lambda(\hat{s}_i)\Phi(\hat{s}_i,\hat{s})\mathrm{d}\Omega_i \tag{6.16}$$

where $\Phi(\hat{s}_i,\hat{s})$ is the scattering phase function, which describes the probability that a ray from one direction $\hat{s}_i$ is scattered into certain other direction $\hat{s}$. The change in intensity for rays traveling in direction $\hat{s}$ within an element as in Figure 6.2 is found by summing the contribution of emission, absorption and scattering. Eq. (6.17) is the radiation transfer equation (RTE)

$$\frac{\mathrm{d}I_\lambda}{\mathrm{d}s} = \hat{s}\cdot\nabla I_\lambda = \kappa_\lambda I_{b\lambda} - \beta_\lambda I_\lambda(\hat{s}) + \frac{\sigma_{s\lambda}}{4\pi}\int_{4\pi} I_\lambda(\hat{s}_i)\Phi(\hat{s}_i,\hat{s})\mathrm{d}\Omega_i \tag{6.17}$$

The augmentation by emission is given by the first term on the right hand side of the equation. The second term quantifies the attenuation of the intensity by extinction. In scattering is taken care by the last term. Radiative heat transfer in porous media can be treated as a continuum at macro level or as a group of particles at pore level. In the case of the macro level, the effective transport properties $(\kappa, \beta, \sigma_s)$ are averaged over a representative elementary volume. The spectral

radiative heat flux vector in the case of radiative heat transport is given by Eq. (6.18) [89, 108]

$$\mathbf{q}_{\mathbf{r},\lambda} = \int_{4\pi} I_\lambda(\hat{s})\hat{s}\mathrm{d}\Omega \tag{6.18}$$

The divergence of the spectral radiative heat flux vector provides the spectral radiative source or the amount of energy stored per differential volume element per unit wavelength. Integrating Eq. (6.17) for all solid angles provide the total radiative source.

$$\int_{4\pi} \hat{s}\cdot\nabla I_\lambda \mathrm{d}\Omega = \int_{4\pi} \left[\kappa_\lambda I_{b\lambda} - \beta_\lambda I_\lambda(\hat{s}) + \frac{\sigma_{s\lambda}}{4\pi}\int_{4\pi} I_\lambda(\hat{s}_i)\Phi(\hat{s}_i,\hat{s})\mathrm{d}\Omega_i\right] d\Omega \tag{6.19}$$

which can be written as

$$\nabla\cdot\int_{4\pi} \hat{s}I_\lambda \mathrm{d}\Omega = 4\pi\kappa_\lambda I_{b\lambda} - \int_{4\pi} \beta_\lambda I_\lambda(\hat{s})d\Omega + \frac{\sigma_{s\lambda}}{4\pi}\int_{4\pi} I_\lambda(\hat{s}_i)\left(\int_{4\pi}\Phi(\hat{s}_i,\hat{s})\mathrm{d}\Omega\right)d\Omega_i \tag{6.20}$$

Since the direction and the space coordinates are all independent from one another [89], in Eq. (6.19) the integral and the direction vector were taken into the gradient. On the right hand side of Eq. (6.20), the order of integration changes by applying the Ω integration only to the part dependent on it, i.e., the scattering phase function Φ_λ. The last integration in brackets is given by Eq. (6.15), thus

$$\nabla\cdot\mathbf{q}_{\mathbf{r},\lambda} = 4\pi\kappa_\lambda I_{b\lambda} - \beta_\lambda\int_{4\pi} I_\lambda(\hat{s})d\Omega + \sigma_{s\lambda}\int_{4\pi} I_\lambda(\hat{s}_i)d\Omega_i \tag{6.21}$$

In order to solve the above equation, knowledge of the intensity I_λ at a point along direction s is required (at the boundaries the intensities are usually specified) and also the medium's effective radiative properties. This study involves in the pore level study of the sponges

to determine the effective transport properties which can be used in continuum approach.

Most of the initial studies on radiative properties of heterogeneous media were done to calculate the heat transport in porous insulating materials with very high porosity. Larkin and Churchill [76] used the two flux method to calculate the radiation heat transport within foam and glass fiber insulations having different bulk density, pore and fiber diameters. The extinction and scattering parameters defined in the two flux equations were obtained by experimental transmittance measurements and also by electromagnetic theory. The obtained radiative parameters were used to find the effective radiative conductivity of the insulating materials. The two flux equations are non linear equations, in order to have an approximated analytical solution, the temperature gradient across the insulation was assumed constant. This assumption is valid only if the rate of heat transfer by radiation is small or otherwise constant. A similar study [23] was made to calculate the heat transfer inside isothermal beds of spheres, cylinders and grains. Yang et al. [120] used the Monte-Carlo technique at a local scale to trace the energy bundle traveling through numerically modeled randomly packed spheres of uniform diameter. The Monte-Carlo simulation was used to obtain the intensity transmission data as a function of bed thickness and sphere surface radiative properties. With the use of two flux equations and transmission data, the effective absorption and scattering coefficients were evaluated. A similar kind of study was reported by Argento and Bouvard [4]. Detail review of experimental and theoretical methods in the determining of thermal radiation properties of dispersed media was done by Baillis et al. [8]. Spectral absorption, scattering coefficients and spectral phase functions were quantified for ceramic sponges by Hendricks and Howell [57, 58]. They used inverse analysis technique based on discrete ordinate radiative models to obtain the radiative properties from the spectral hemispherical reflectance and transmittance measurements. The experimental methods in characterization of radiative properties of foams made of different materials are found in literature [7, 6, 122, 102]. Ray tracing techniques provide a great advantage in replicating the experimental radiation measurements using computer simulations, but it requires a precise knowledge about the porous structure morphology to have accurate results. Tan-

crez and Taine [109] developed a method to identify the absorption coefficient, scattering coefficient and scattering phase function of an Identical Overlapping Opaque Spheres (IOOS) and an Identical Overlapping Transparent Spheres (IOTS) arrangements using Monte-Carlo ray tracing technique. Evolution of 3D visualization techniques such as computer tomography using X-rays scans, magnetic resonance imaging using the effect of Nuclear Magnetic Resonance (NMR) and light microscopy gave a possibility to capture topological heterogeneities typical for porous structures. This provided the prospect of using the ray tracing techniques to identify the radiative properties of reticulated porous structures, which were previously employed only in theoretically simulated randomly packed sphere structures. The theoretical approach obtained by Tancrez and Taine [109] was subsequently used along with the computer tomography (μ-CT) geometrical data by Petrascha et al. [96] to find the radiative properties of a 10 PPI reticulated ceramic sponge. The present work used the theoretical approach mentioned in [109] along with the computational grids generated from the tomography scan data of different high porosity reticulated ceramic sponges to find their extinction coefficients and the scattering phase functions. The effect of the sponge structure on the radiative properties was studied. The scattering phase functions of the sponges were obtained considering the surface to be diffusely and specularly reflecting.

6.1 Radiative Properties identification

The objective of the work was to identify the ceramic porous inert medias' equivalent semi transparent extinction and scattering properties. The structural morphology of the sponges was initially assumed to be isotropic and later was tested for statistical isotropy using the identified equivalent radiative extinction coefficients. The solid strut structure of the porous media was considered as opaque and the vacant space in between the solid strut was considered transparent to radiation. The typical strut thickness of a sponge is much larger than the thermal radiation wavelength range, so the effect of diffraction was neglected and the medium was assumed to follow the laws of geometric optics. By excluding polarization, the scattering depends only on the reflection property of the strut.

6.1.1 Extinction coefficient

An in-house ray tracing algorithm was used to track the rays inside the sponge structure. The ray tracing code is a modified (simplified) version of an in-house Monte-Carlo radiative heat transfer code developed by Brunn [17]. In the case of the Monte-Carlo code developed by Brunn [17], each surface element and volume element emits rays, and the energy contained in each ray depends on the temperature of the element and material/gas radiative property. The emission location for each ray is calculated and assigned. The rays are assigned with a wavelength based on cumulative distribution function of the spectral distribution of the radiative properties of surface and volume elements. The emitted rays are traced and the absorption, scattering of the rays at the wall and in the volume elements are used to calculate the radiative heat flux and the source respectively.

In the modified Monte-Carlo code that is used in this study, the subroutines to allocate individual rays with energy and wavelength are deactivated, and void volume elements are considered to be transparent. The wall emission is made inactive and the ray emission takes place only in the volume elements. The details of selection of emission locations for the rays and the methodology used in assigning random direction and ray tracing are well documented by Brunn [17]. The ray-tracing algorithm [17] can in principle be operated with both tetrahedral meshes as well hexahedral grid. The computational grids are generated using ICEM software, the flow calculation program ANSYS CFX is used to set the boundary conditions during pre-processing, then the grids are then exported with the additional information about the boundary conditions. The grid information is then converted so that all necessary connectivities can be determined. The flowchart of the ray tracing process is shown in Figure 6.3.

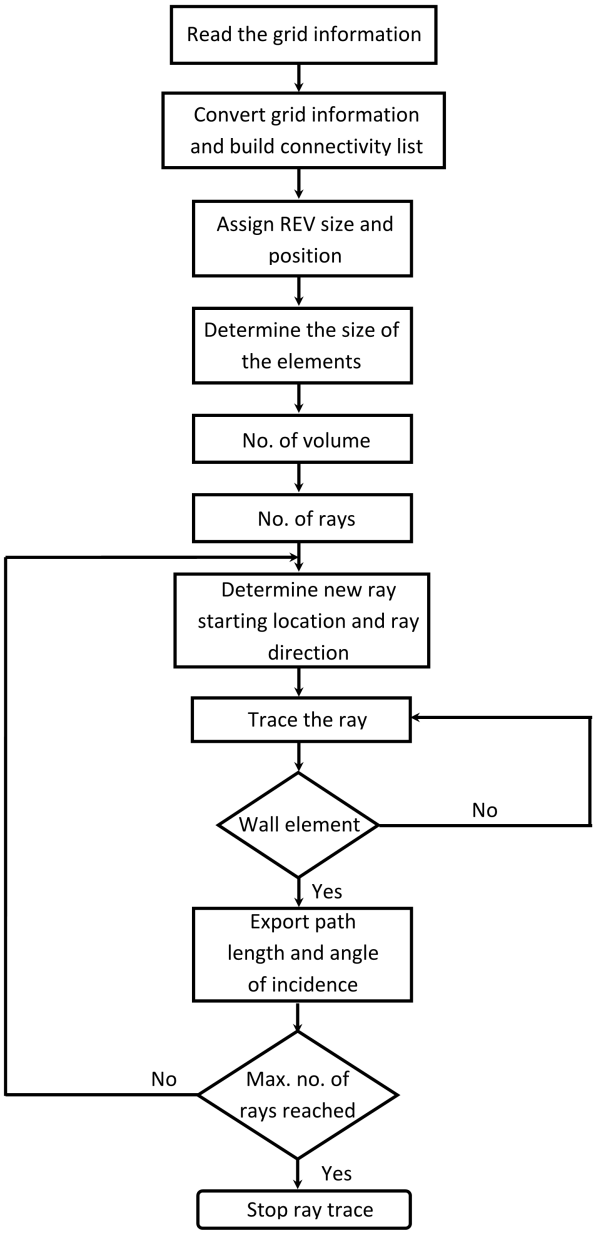

Figure 6.3: Flowchart representing the ray tracing process.

In this study, the emission locations E within the representative elementary volume (REV) are randomly chosen by the ray tracing algorithm and a direction is assigned to each of the rays for its travel. The algorithm then tracks the path of each ray starting from the REV until the ray encounters an opaque strut surface of the sponge. At the point E_0 where the ray encounters the solid opaque strut, a part of each ray is absorbed and the remaining is reflected back in different directions based on the reflective properties of the strut material. When the ray encounters the solid strut it is completely extinguished in that particular direction of its travel (by absorption and scattering) and are not traced further. The rays which cross the total domain length without any interaction with the strut are also not traced further. The extinction of the rays completely depends on the sponge's structural geometry and is independent of the frequency of the ray. The path length L_e traveled by each ray are determined using the ray tracing algorithm. Statistically large numbers of rays $N_{ray} = 10^7$ are traced for their path lengths, which are used to find out a probability based extinction coefficient of the sponge media. A schematic representation of the ray tracing technique is shown in Figure 6.4.

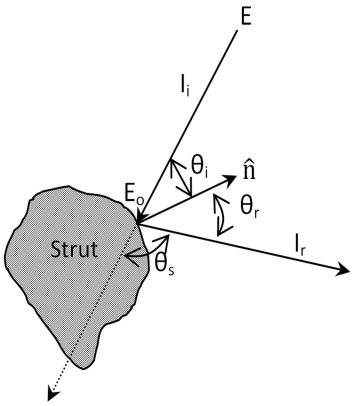

Figure 6.4: Schematic diagram of the ray tracing technique used in the identification of the radiative properties of the porous structure.

Using the ray tracing code, large numbers of rays are traced for their path length of extinction L_e. With the path length of extinction data, the extinction probability of a ray within range $[L,\ L + \mathrm{d}L]$ in the local scale is calculated using

$$P_e(L) = F_e(L)\mathrm{d}L = \frac{1}{N_{ray}} \sum_{j=1}^{N_{ray}} \delta(L - L_{e,j}) \tag{6.22}$$

where $F_e(L)$ is the extinction probability density function at location L and δ is the Dirac delta function. The cumulative probability distribution function of extinction in local scale is given by

$$C_e(L) = \int_0^L F_e(L')\mathrm{d}L' \tag{6.23}$$

In a continuous absorbing and scattering media, the probability density function $f_e(L)$ and the cumulative probability distribution function $c_e(L)$ of extinction are given by Eq. (6.24) and Eq. (6.25). Eq. (6.4) becomes identical to Eq. (6.25), when β in Eq. (6.4) is independent of location within the continuous medium.

$$f_e(L) = \beta e^{-\beta L} \tag{6.24}$$

$$c_e(L) = 1 - e^{-\beta L} \tag{6.25}$$

where β is the extinction coefficient of the continuous media. The equivalent extinction coefficient β of a sponge can be obtained by determining $C_e(L)$ and equating it to Eq. (6.25) and by performing a least square fit.

6.1.2 Absorption coefficient

Similar to extinction, the absorption probability of a ray within range $[L,\ L + \mathrm{d}L]$ in the local scale is given by

$$P_a(L) = F_a(L)\mathrm{d}L = \frac{1}{N_{ray}} \sum_{j=1}^{N_{ray}} \alpha' \delta(L - L_{e,j}) \tag{6.26}$$

where α' is the directional hemispherical absorptance of the strut material. The absorptance α' depends on the angle of incidence θ_i, i.e.,

the angle between the incident ray I_i and the local normal vector $\hat{n}$ at the surface of incidence, as shown in Figure 6.4. The probability of the angle of incidence within range [μ_i, μ_i + dμ_i] is given by the following relation

$$P(\mu_i) = F(\mu_i)\mathrm{d}\mu_i = \frac{1}{N_{ray}} \sum_{j=1}^{N_{ray}} \delta(\mu_i - \mu_{i,j}) \tag{6.27}$$

where μ_i, is the cosine of incident angle θ_i. With the use of $F_e(L)$ and $F(\mu_i)$, Eq. (6.26) can be written as

$$P_a(L) = F_a(L)\mathrm{d}L = F_e(L)\mathrm{d}L \int_0^1 \alpha'(\mu_i)F(\mu_i)\mathrm{d}\mu_i \tag{6.28}$$

For a continuous absorbing media, the probability of absorption of a ray is given by

$$p_a(L) = f_a(L)\mathrm{d}L = \kappa \cdot e^{-\beta L}\mathrm{d}L \tag{6.29}$$

If the reflection by the sponge strut is considered diffuse, the absorptance is independent of the incident cosine, Eq. (6.28) simplifies as below

$$P_a(L) = F_a(L)\mathrm{d}L = \alpha_d \cdot F_e(L)\mathrm{d}L \tag{6.30}$$

For a continuous media, Eq. (6.30) can be simplified to Eq. (6.31), from which the equivalent absorption coefficient of a diffuse reflecting sponge can be obtained

$$\kappa = \beta \cdot \alpha_d \tag{6.31}$$

6.1.3 Scattering phase function

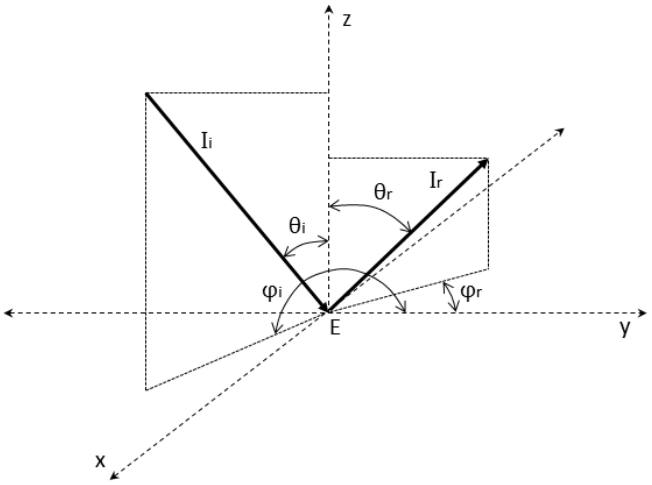

Figure 6.5: A schematic representing incidence and reflection on a surface.

The scattering phase function Φ describes the probability that a ray from one direction will be scattered into a certain other direction [89]. As mentioned previously, in the present study the sponges were assumed to be isotropic, so that the scattering phase function is independent of the incident ray direction and assumed to be only the function of the cosine of scattering angle $(I_i \cdot I_r)$, i.e., the angle between the incident and reflected ray. For any incident ray as shown in Figure 6.5, the x, y and z components of a unit vector I_i representing the direction of incidence are written as

$$I_i = (-sin\varphi_i\sqrt{1-\mu_i^2}, cos\varphi_i\sqrt{1-\mu_i^2}, -\mu_i) \tag{6.32}$$

Similarly, for the reflected ray, the components representing the unit vector I_r for the reflected direction are

$$I_r = (sin\varphi_r\sqrt{1-\mu_r^2}, -cos\varphi_r\sqrt{1-\mu_r^2}, \mu_r) \tag{6.33}$$

The cosine of scattering angle μ_s for all possible incident, reflection and azimuth angles at any point E on a surface is given by

$$\mu_s = I_i \cdot I_r = -\sqrt{(1-\mu_i^2)(1-\mu_r^2)}cos(\varphi_i - \varphi_r) - \mu_i\mu_r \tag{6.34}$$

In the case of specular reflection the reflectance ρ'' depends only on the incident angle and according to the laws of specular reflection, $\theta_\mathrm{i} = \theta_\mathrm{r}$ and φ_r - $\varphi_\mathrm{i} = \pi$, thus

$$\mu_s = 1 - 2\mu_i^2 \tag{6.35}$$

The scattering phase function can be determined using Eq. (6.36) [96, 109].

$$\Phi(\mu_s) = \frac{\int_0^1 \int_0^{2\pi} \int_0^1 \delta(I_i \cdot I_r - \mu_s)\rho'' F(\mu_i)\mu_r \mathrm{d}\mu_r \mathrm{d}(\varphi_i - \varphi_r)\mathrm{d}\mu_i}{\int_0^1 \int_0^{2\pi} \int_0^1 \rho'' F(\mu_i)\mu_r \mathrm{d}\mu_r \mathrm{d}(\varphi_i - \varphi_r)\mathrm{d}\mu_i} \tag{6.36}$$

where the numerator represents the scattered energy for any given μ_s and the denominator represents the total scattered energy in all possible directions. The bidirectional reflectance ρ'' in Eq. (6.36) is a function of the incident angle θ_i and the reflection angle θ_r and it is assumed to be independent of azimuth angles of incidence φ_i and reflection φ_r. For uniform irradiation on a specular surface, the bidirectional reflectance is

$$\rho'' = \rho'/\mu_r \tag{6.37}$$

where ρ' is hemispherical directional reflectance. For a diffuse reflecting surface, the bidirectional reflectance ρ'' is given by Eq. (6.38)

$$\rho'' = \rho'/\pi \tag{6.38}$$

6.1.4 Ray tracing validation

The validation of the ray tracing code was done with IOOS and IOTS computer simulated structural arrangements [109]. The structures were

constructed with randomly packed spheres having diameter of 0.1 cm within a cube of volume 27 cm^3. The porosity of the IOOS structure was 80% and that of the IOTS was 60%. In the case of IOOS structure the rays were traced in the void space filled in between the spheres outer surface and in the case of IOTS structure the rays were traced within the interconnected sphere volume. Due to the change in the volume in which the rays were traced, the definitions of void space in calculating porosity are different for IOOS and IOTS structures.

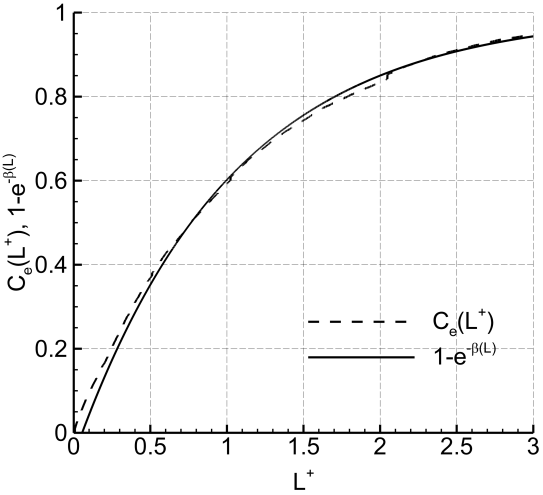

Figure 6.6: The cumulative distribution function of extinction along the normalized side length ($L^+ = L/d_{pore}$) of the IOTS structure.

Figure 6.6 shows the extinction cumulative probability distribution function $C_e(L)$ of the IOTS structure in local scale calculated using Eq. (6.23) and the continuous media cumulative extinction probability distribution of extinction $c_e(L)$. The obtained profiles are similar to the results provided in [109] for a similar case. In the case of the IOOS structure, the arrangement is made of a large number of opaque spheres and the probability density function of incidence cosine is expected to be same as that of a single sphere irradiated by a beam of light [$F(\mu_i)$

$= 2\mu_i]$ as described in [96, 109].

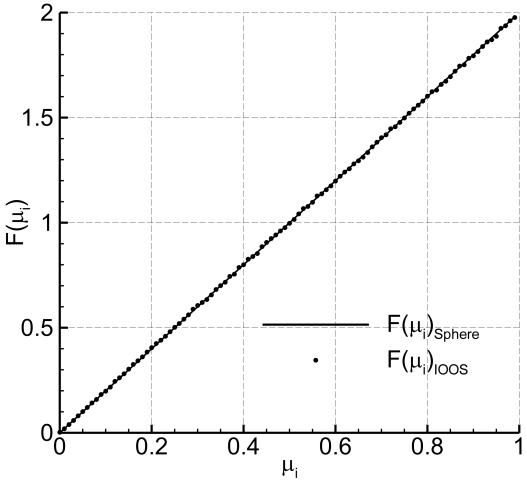

Figure 6.7: Comparison of the probability density functions of incident cosine of the IOOS structure computed by the ray tracing method to the analytical solution for that of a sphere.

Figure 6.7 shows the probability density function of the IOOS structure determined by the ray tracing method matching exactly with that of a single sphere. The scattering phase function of a diffuse sphere is independent of the reflectance [89], but depends on the probability density function of the angle of incidence $F(\mu_i)$. The expression for the scattering phase function of a large opaque diffusely reflecting sphere irradiated by uniform intensity is [89]

$$\Phi(\mu_s)_{Diff.sphere} = \frac{8}{3\pi}[sin(\mu_s) - \mu_s cos(\mu_s)] \tag{6.39}$$

As shown in Figure 6.7, in the case of the IOOS structure, the $F(\mu_i)$ is the same as that of a sphere and for any reflectance value, the scattering phase function of the IOOS structure should also be the same as that

of a large diffusely reflecting sphere. The ray tracing calculation performed with the IOOS structure provided the expected result as shown in Figure 6.8 and thus validates the ray tracing code and procedure used to calculate the scattering phase function for diffuse reflection.

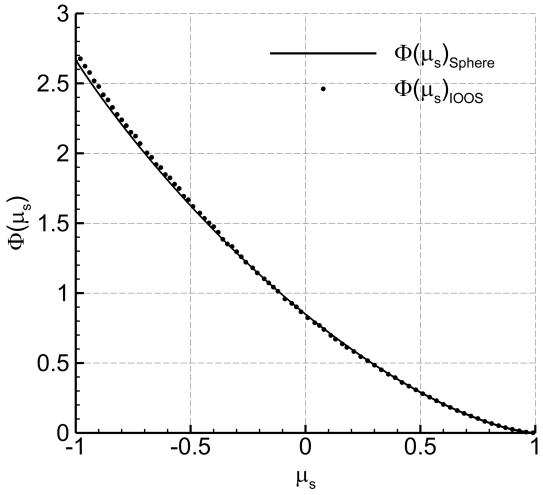

Figure 6.8: Diffuse scattering phase function of the IOOS structure computed using the ray tracing technique and the analytical scattering phase function of a large diffusely reflecting sphere.

In the case of specular reflection, the scattering phase function is dependent on the reflectance of the surface and also on $F(\mu_i)$. The approximate expression as in Eq. (6.40) was used by Tancrez and Taine [109] to calculate the directional hemispherical reflectance in terms of the hemispherical absorbtance α. The same expression is used in this study in order to compare the results with that of Tancrez and Taine [109].

$$\rho' = 1 - (3/2) \cdot \alpha \cdot \mu_i \tag{6.40}$$

Form the definition of scattering phase function

$$\Phi(\mu_s)\mathrm{d}\mu_s = \frac{F(\mu_i)\rho'(\mu_i)\mathrm{d}\mu_i}{\int_0^1 F(\mu_i)\rho'(\mu_i)\mathrm{d}\mu_i} \tag{6.41}$$

For specular reflection, Eq. (6.35) is rearranged as

$$\mu_i = \sqrt{\frac{1-\mu_s}{2}} \tag{6.42}$$

From which

$$\mathrm{d}\mu_i = -\frac{\mathrm{d}\mu_s}{4\sqrt{\frac{1-\mu_s}{2}}} \tag{6.43}$$

μ_i has limits, 0 to 1, for which μ_s has limits, 1 to -1. By reversing μ_s limits, and substituting Eq. (6.43) in Eq. (6.41) provides

$$\Phi(\mu_s)_{Spec} = \frac{F(\mu_s)\rho'(\mu_s)\mathrm{d}\mu_s}{4\sqrt{\frac{1-\mu_s}{2}}\int_0^1 F(\mu_i)\rho'(\mu_i)\mathrm{d}\mu_i} \tag{6.44}$$

For a sphere irradiated with uniform intensity, $F(\mu_i) = 2\mu_\mathrm{i}$, then Eq. (6.41) becomes

$$\Phi(\mu_s)_{Spec.Sphere}\mathrm{d}\mu_s = \frac{2\mu_i\rho'(\mu_i)\mathrm{d}\mu_i}{\int_0^1 2\mu_i\rho'(\mu_i)\mathrm{d}\mu_i} \tag{6.45}$$

Substituting Eq. (6.40) and Eq. (6.43) in Eq. (6.45) and integrating the denominator gives

$$\Phi(\mu_s)_{Spec.Sphere} = \frac{1-\frac{3}{2}\alpha\left(\sqrt{\frac{1-\mu_s}{2}}\right)}{2(1-\alpha)} \tag{6.46}$$

To validate the method for specular reflection, the scattering phase function of the IOOS structure was compared with that of a sphere.

The comparison of the specular phase functions for different values of α is shown in Figure 6.9.

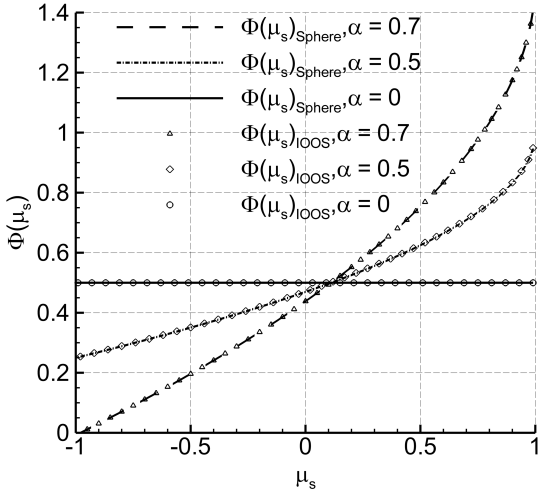

Figure 6.9: Specular scattering phase functions of the IOOS structure compared with those of a sphere with different surface absorbtance values.

6.2 Radiative properties of sponges

6.2.1 Extinction coefficient

The numerical simulations were carried out for grid structures generated from tomographic scans of different sponge structures. Parallel rays were emitted from the chosen REV in each Cartesian direction and were traced for their path length of travel. The path length data obtained in each individual direction was used to find the directional equivalent extinction coefficients (β_x, β_y, β_z) using Eq. (6.23) and Eq. (6.25). The simulations were carried out from three different locations within each sponge structure to avoid any influence of local structural errors and the arithmetic average of the three values was consider as

the directional equivalent extinction coefficient of the sponge in a particular direction. The directional equivalent extinction coefficients of the 30 PPI 80% porosity alumina sponge structure are given in Table 6.1 along with their standard deviation values. Figure 6.10 shows the normalized intensity and its exponential fit values along the normalized path length of the 30 PPI 80% porosity alumina sponge structure. The obtained directional equivalent extinction coefficients (β_x, β_y, β_z) were compared to justify the structure isotropy assumption.

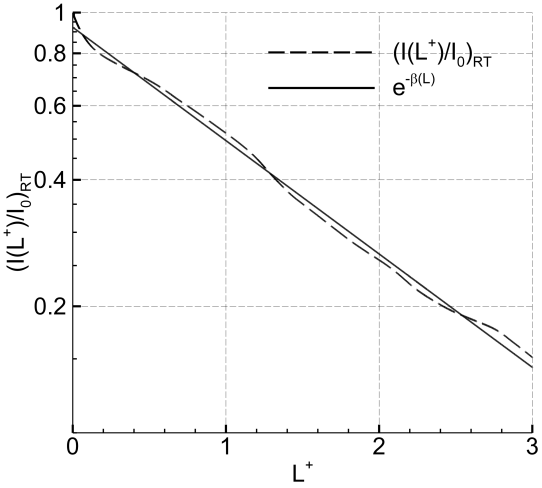

Figure 6.10: Normalized intensity and its exponential curve fit as a function of the normalized path length $L^+ = L/d_{pore}$ of a 30 PPI 80% porosity Al_2O_3 sponge.

Figure 6.11 shows the normalized intensity as a function of normalized length in all the three Cartesian directions of the 30 PPI 80% porosity sponge structure. It can be seen that the normalized intensity in all three directions are similar and have exponential reduction with increase in path length, thus supporting the isotropic assumption. The arithmetic average of the three directional equivalent extinction coefficients (β_x, β_y, β_z) was taken as the equivalent extinction coefficient of

the sponge structures.

Table 6.1: Directional equivalent extinction coefficients with their standard deviation values and the mean extinction coefficient of a 30 PPI 80% porosity alumina sponge.

Al_2O_3 30 PPI 80% porosity	**Directional**			**Equivalent**
Extinction	Dir-x	Dir-y	Dir-z	0.391
coefficient (mm^{-1})	0.377	0.397	0.399	
Standard deviation	0.009	0.013	0.021	0.012

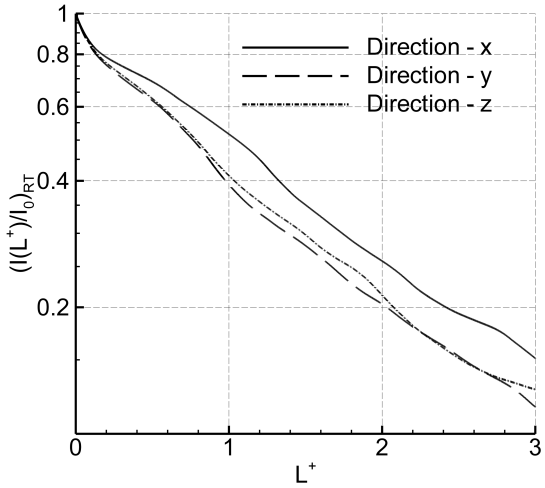

Figure 6.11: Normalized intensities along the normalized path length in all three Cartesian directions of a 30 PPI 80% porosity Al_2O_3 sponge.

The values of the equivalent extinction coefficient obtained for various sponge structures are given in Table 6.2. From Table 6.2, it can be seen that for the same pore density, the extinction coefficient values increase with a decrease in the porosity values. This can be attributed to the fact that the porosity of the sponges having same pore density varies only due to the variation in the strut diameter. Thinner struts provide higher porosity in comparison to thicker struts. As the strut diameter increases, the extinction of rays also increases due to the increase in specific surface area. For the same porosity, with an increase in the pore density, the surface area of the structure increases and so does the extinction coefficient, which is justified with the results given in the Table 6.2. The equivalent extinction coefficient of a SiSiC sponge with 20 PPI 85% porosity was found to be different in comparison to that of an alumina sponge with the same structural properties.

Table 6.2: The mean equivalent extinction coefficient and absorption coefficient values of different sponge structures identified using the ray tracing technique.

Pore density (PPI)	**Porosity(%)**	**Extinction coefficient (mm^{-1})**	**Absorption coefficient (mm^{-1})**
10 (Al_2O_3)	80	0.194	0.058
10 (SiSiC)	85	0.149	0.124
20 (Al_2O_3)	75	0.362	0.109
	80	0.344	0.103
	85	0.313	0.094
20 (SiSiC)	85	0.211	0.175
30 (Al_2O_3)	75	0.504	0.151
	80	0.391	0.117
	85	0.388	0.116
45 (Al_2O_3)	80	0.776	0.233

Hendricks and Howell [57] proposed a correlation for the extinction coefficient based on their experimental results for zirconia and SiC

sponges. The extinction coefficient is related to the porosity and the pore diameter of a sponge using

$$\beta = \frac{4.4}{d_{pore}}(1-\varepsilon) \tag{6.47}$$

For the SiSiC sponges, the correlation proposed by Hendricks and Howell [57] Eq. (6.47), in comparison with the extinction coefficient values in Table 6.2 has a RMSD of 4.7%. For the alumina sponges, a correlation is proposed as in Eq. (6.48)

$$\beta = \frac{3.9}{d_{pore}}(1-\varepsilon) \tag{6.48}$$

which in comparison with the alumina sponge extinction coefficient values in Table 6.2 has a RMSD of 6.3%.

6.2.2 Scattering phase function

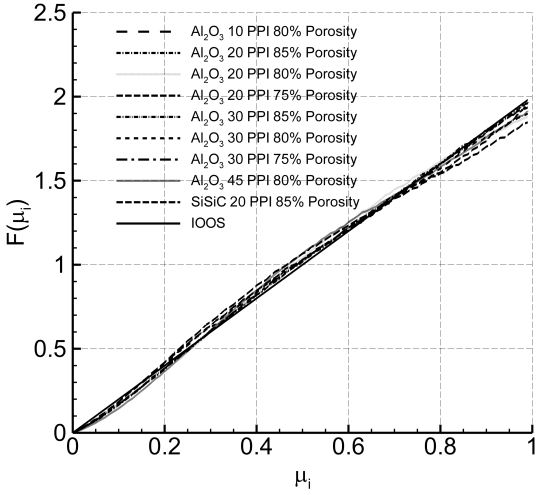

Figure 6.12: Comparison of the probability density functions of incident cosine of various sponge samples to the analytical solution of a sphere.

The sponges used for this study were all made of non metallic materials and have a rough microscopic surface [31]. The surfaces are most probably expected to have a diffuse reflection (though in visible light SiSiC sponges are found to be having some shiny surfaces, predominantly the sponges seem to be diffusive). As mentioned in the code validation section, in the case of diffuse reflection, the scattering phase function is independent of the reflectance property of the material. Thus the phase function is only dependent on the structural tomography and is specific to the probability density function of incidence cosine.

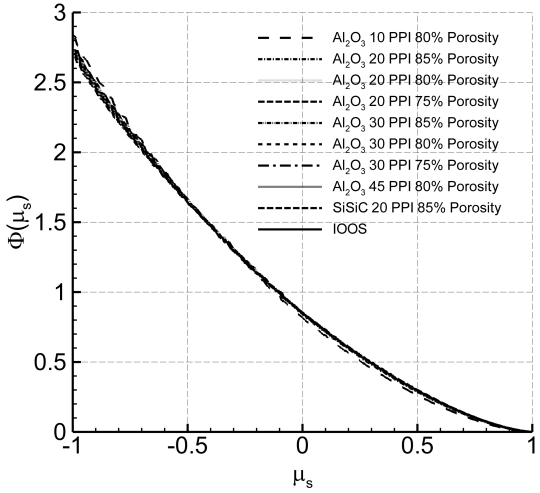

Figure 6.13: Diffuse scattering phase function of different sponge samples and that of the IOOS structure, computed using ray tracing code.

As the struts are cylindrical in nature and are oriented in all the directions within a sponge, the probability density function of incidence cosine have a profile similar to that of a single sphere irradiated by a beam of light. Figure 6.12 shows the $F(\mu_i)$ of all the sponges studied in this work as a function of incidence cosine μ_i. The comparison of the values of $F(\mu_i)$ agrees well with that of a sphere. The slight variation between the $F(\mu_i)$ curves to that of a sphere might be due to

the concave surfaces of the nodes in the sponge structures. The phase function identification was carried out with a hemispherical reflectance value of 0.5 for all the sponges. The value of incident cosine probability density function required for solving Eq. (6.36) was obtained from a fifth degree polynomial curve fit to the curves plotted in Figure 6.12. As the $F(\mu_i)$ are similar to that of the IOOS structure or a sphere, the diffuse scattering phase functions are expected to be similar to that of the IOOS structure as shown in Figure 6.13. The back scattering effect is very strong for all the sponge structures. If metallic sponges were studied, the scattering effect should be predominately forward due to the shiny, polished metallic surface and should be similar to the specular phase functions obtained for the IOOS structure.

6.2.3 Absorption coefficient

The sponges were assumed to be diffuse reflecting due to their rough microscopic surface [31]. Eq. (6.31) was used in determining the equivalent absorption coefficients with the values of equivalent extinction coefficients and the absorptance of the sponges. The absorption coefficient values of different sponges used in this study are given in Table 6.2. The absorptance values ($\alpha_{Alumina} = 0.3$ and $\alpha_{SiSiC} = 0.83$) were taken from [89], with the assumptions that the alumina sponges were made of grains of size 10 μm and working temperature between 1010°C - 1565°C.

Chapter 7

Conclusion

The main objective of this study was to determine the heat transfer and fluid flow properties of the ceramic sponges, and to express them in terms of the known geometric parameters of the sponges. The conventional CFD tools were used in calculating the fluid flow and the heat transfer. The computational volumes required for such analysis were regenerated using three dimensional tomography imaging techniques. The computational grids thus obtained represent the real three dimensional structure of the sponges. The geometric parameters such as porosity, pore diameter and specific surface area were measured using the reconstructed geometries. Sponges made of two different ceramic materials, SiSiC and alumina, were studied. The porosities of the alumina sponge were in the range of 75% to 85% and the pore densities are of 10, 20, 30 and 45 PPI. While in the case of SiSiC sponges, two sponges were studied, one of pore density 10 PPI and other of 20 PPI. Both the sponges had porosities around 87%.

The study involved in the simulation of pressure drop in fluid flow within the sponge structures. For the simulations, air was used as the fluid medium and the simulations were performed for Reynolds numbers ($Re = \rho d_h u_s/\mu$) 10, 100, 500, 1000 and 1500. Using the simulation results, a general correlation (similar to that of the Ergun equation) for the pressure drop in ceramic sponges was proposed. In order to study the influence of the tortuosity on the pressure drop.

The tortuosity value for each sponge was calculated using Lagrangian particle tracking (LPT) method to track the particle in the Eulerian fluid phase. The influence of the solid tortuosity on the pressure drop was included in the general pressure drop correlation.

$$\frac{\Delta p}{\Delta x} = \zeta \cdot \frac{\mu {S_v}^2}{\varepsilon^3} u_s + \frac{\tau}{\tau'} \eta \cdot \frac{\rho S_v}{\varepsilon^3} {u_s}^2$$

The above correlation is able to predict the pressure drop within a root mean square deviation of 21.5%.

In the next step of this work, the direct pore level simulations were performed to determine the axial dispersion coefficient values of gaseous flow in sponge structures. It was found that the spatial velocity variations of the sponges with respect to the bulk flow velocity remain the same irrespective of the sponges' structural parameters. For a given internal bulk velocity, the axial dispersion of a gas flow within a sponge structure is a function of pore diameter of the sponge and its porosity. The axial mixing length is recommended as the characteristic length in calculating the Peclet number, and also a new correlation to determine the characteristic length based on pore diameter and tortuosity of the sponges was formulated.

$$d = d_{pore} \times (-4.4 + 4.5\tau)$$

With the proposed characteristic lengths, the Peclet numbers ($Pe_L = ud/D_L$) of sponges are approximately equal to the value of 2, which is reported in literature as the Peclet number for packed bed.

The convective heat transfer within porous beds are well known to be a function of the pressure drop. The dependency of the convective heat transfer on the pressure drop in porous media is given by the generalize Lévêque equation (GLE). The applicability of the generalized Lévêque equation in the case of reticulated ceramics is studied in recent years. In this study, the heat transfer coefficients for the sponges were calculated for three different fluids with Prandtl numbers 0.7, 2 and 6, respectively. The simulations were performed for Reynolds numbers ($Re = \rho d_h u_s/\mu$) 10, 100, 500, 1000 and 1500. Based on GLE, a correlation for the Nusselt number in terms of non-dimensional pressure drop (Hagen number) was developed. Instead of incorporating correction factors in the GLE to match the experimental results, the axial

mixing length is used as one of the parameter to correlate the Nusselt number and the Hagen number.

$$Nu = 0.17(Prd_h/L_dHg)^{1/3}, \text{where } L_d = l_l$$

The correlation is able to bring down the error values within a range of $\pm 35\%$, which is better than the error range of $\pm 40\%$ found in the literature for ceramic sponges. In the case of heterogeneous models, there is a need to find the solid effective conductivities of the sponges. In this work the solid effective conductivity was related to the solid structure tortuosity. Using the heat transfer simulation results, the solid tortuosity values of the sponges were calculated with the help of one dimensional Fourier's law of conduction. It is found that for a given ceramic sponge, the solid conduction tortuosity is independent of the sponges structure properties such as pore density and porosities etc. The two phase effective conductivity was found by substituting the solid phase effective conductivity in the parallel two phase model.

$$k_{eff(2phase)} = \varepsilon_1 k_1 + (1 - \varepsilon_1)k_2$$

Finally, an in-house ray tracing code was used along with the tomography based computational grids to obtain the equivalent radiative properties of different porous structures. The porous media were found to be isotropic in structure. The extinction coefficient increased with decreasing porosity for the same pore density and decreased with increasing pore density for the same porosity. The diffuse and specular scattering phase functions were found to be independent of structural properties of the porous media, such as the porosity and the pore density. The diffuse scattering phase functions of the porous media were found independent to the surface reflectance and were similar to that of a large diffusely reflecting sphere. The specular phase functions were dependent on the surface reflectance. Similar to the correlation that was found in literature, a correlation for extinction coefficient of the alumina sponges in terms of pore diameter and porosity was formulated.

$$\beta = \frac{3.9}{d_{pore}}(1 - \varepsilon)$$

In conclusion, with the help of direct pore level simulations, the correlations to calculate the heat transfer properties of heterogeneous

reticulated ceramic sponges were proposed. The correlations are based on the readily available sponge properties, so that they can be readily used in the design and the optimization of the processes and applications where the ceramic sponges are widely used, and also to aid in developing new applications.

Future outlook

The major problem in dealing with the reticulated porous structures is that of accurately describing their morphological properties. Though the reconstruction of these structures using computer tomographic images helps in accurately quantifying the properties of a given structure, they may not be the same for any other RPC structure of same material, pore density and porosity. The relation between the properties such as specific surface area and pore diameter with that of easily measurable properties such as porosity or pore density are not well correlated. The problem in defining the morphological properties reflects in the difficulty in studying their flow, heat and mass transfer properties and also in developing reliable correlations. With additive manufacturing technologies such as elective electron beam melting, selective sintering, 3D printing etc., it is now possible to manufacture open cell structures to a predefined geometry with high accuracy [65]. With these technologies, it is now possible to produce open cell structures with required pressure drop, heat and mass transfer properties. Well defined structures can be studied using DPLS simulation even without computer aided reconstruction of these open cell structures. It will greatly help in the study of different well defined morphological structures and will aid in attaining the required properties for specific applications. For example, in case of two step thermochemical solar reactors (step 1: metal oxide reduction at high temperatures, step 2: cooling and oxidation of metal oxide which results in reduction of H_2O and CO_2) that are presently studied for syngas production using sun light [1, 24, 44, 46, 80, 81], the heat transfer process in form of conduction, convection and radiation within RPC plays an important role. The rate of reduction of metal oxide (ceria, ZnO_2, etc.) is greatly dependent on the rate of increase in the temperature of the RPC [44], and also, in the cases of reduction of CO_2 and H_2O into CO and H_2, the specific surface area of the RPC

plays a major role. Increasing the specific surface area of RPC beyond its natural level helps in further increasing the oxidation surface area of the metal oxide. Thus it increases the reduction of H_2O and CO_2 [46]. One of the methods presently studied to increase the specific surface area of the RPC structure is to manufacture the RPC structures with increased micro porosity [46]. The strut structures contain micro pores to increase the specific surface area, but it reduces the overall conductivity of the sponges. With the number of operating cycles there are possibilities that these pores could get closed due to sintering at high temperatures. Another promising possibility is to increase the surface area by imparting projections/fins to the struts. This can be achieved by additive manufacturing technologies. With regular structures such as the ordered kelvin structure and by imparting protrusions on to its struts, it is possible to alter the pressure drop, heat and mass transfer and radiation properties as required. This may be a better way than the complex process of trying to impart randomness to the ordered structures to achieve required results, because the artificially induced randomness imparts similar structural uncertainties as that of the RPC structures manufactured by Schwartzwalder process.

Chapter 8

Annex

8.1 Pressure loss

Table 8.1: Superficial air velocities and the corresponding pressure drops per unit length in the sponge structures.

Structure name	**u_s [m/s]**	**Pressure drop [kPa/m]**
Al_2O_3 10 PPI 80% porosity	0.0185	1.7
	0.1862	28.4
	0.9313	350.6
	1.8626	1149.0
	2.7939	2372.8
SiSiC 10 PPI 85% porosity	0.0196	1.6
	0.1959	27.5
	0.9797	363.3
	1.9595	1223.3
	2.9392	2546.3
Al_2O_3 20 PPI 75% porosity	0.0384	16.8
	0.3841	310.8
	1.9206	4523.4
	3.8412	16193
	5.7618	34970

Al_2O_3 20 PPI 80% porosity	0.0346	6.8
	0.3460	125.4
	1.7297	1745.1
	3.4595	6257.3
	5.1892	13541
Al_2O_3 20 PPI 85% porosity	0.0374	9.1
	0.3736	158.5
	1.8678	2167.3
	3.7356	7712.8
	5.6035	16638
SiSiC 20 PPI 85% porosity	0.0243	2.7
	0.2433	45.2
	1.2163	581.3
	2.4327	1976.3
	3.6491	4163.8
Al_2O_3 30 PPI 75% porosity	0.0496	30.3
	0.4962	613.6
	2.4810	10048
	4.9619	37634
	7.4429	82817
Al_2O_3 30 PPI 80% porosity	0.0501	21.8
	0.5010	380.1
	2.5048	5405.1
	5.0098	19437
	7.5146	42102
Al_2O_3 30 PPI 85% porosity	0.0433	15.9
	0.4329	271.4
	2.1642	3510.1
	4.3286	12283
	6.4928	26322
Al_2O_3 45 PPI 80% porosity	0.0649	66.9
	0.6493	1789
	3.2463	27615
	6.4925	98559
	9.7387	212788

8.2 Axial dispersion coefficients

Table 8.2: Superficial air velocities and the corresponding axial dispersion coefficient values of the sponge structures.

Structure name	**u_s [m/s]**	**Axial dispersion coefficient $\times$ 10^{-3} [m^2/s]**
Al_2O_3 10 PPI 80% porosity	2.85	3.00
	4.28	4.35
	5.70	5.81
SiSiC 10 PPI 85% porosity	4.00	6.50
Al_2O_3 20 PPI 75% porosity	2.66	2.70
	3.99	4.10
	5.33	5.50
Al_2O_3 20 PPI 80% porosity	3.23	2.6
	4.84	3.9
	6.46	5.2
Al_2O_3 20 PPI 85% porosity	3.28	1.68
	4.92	2.76
	6.56	3.65
SiSiC 20 PPI 85% porosity	4.00	6.03
Al_2O_3 30 PPI 75% porosity	2.86	1.80
	4.30	2.92
	5.73	3.90
Al_2O_3 30 PPI 80% porosity	3.37	1.40
	5.06	2.20
	6.75	2.90
Al_2O_3 30 PPI 85% porosity	3.13	1.40
	4.69	2.10
	4.69	2.80
Al_2O_3 45 PPI 80% porosity	2.94	3.10
	4.41	4.80
	5.89	6.50

8.3 Heat transfer coefficients

Table 8.3: Superficial velocities for a fluid of Pr = 0.7 and the corresponding heat transfer coefficient values of the sponge structures.

Structure name	**u_s [m/s]**	**Heat transfer coefficient [W/m²K]**
Al_2O_3 10 PPI 80% porosity	0.0185	8.69
	0.1862	34.97
	0.9313	96.43
	1.8626	125.89
	2.7939	177.71
SiSiC 10 PPI 85% porosity	0.0196	11.69
	0.1959	32.99
	0.9797	79.27
	1.9595	122.13
	2.9392	170.13
Al_2O_3 20 PPI 75% porosity	0.0384	19.03
	0.3841	51.01
	1.9206	166.74
	3.8412	228.78
	5.7618	262.81
Al_2O_3 20 PPI 80% porosity	0.0346	18.35
	0.3460	55.11
	1.7297	101.63
	3.4595	247.05
	5.1892	317.66
Al_2O_3 20 PPI 85% porosity	0.0374	21.53
	0.3736	64.21
	1.8678	171.39
	3.7356	227.80
	5.6035	339.77
SiSiC 20 PPI 85% porosity	0.0243	13.51
	0.2433	29.46
	1.2163	100.13
	2.4327	148.31
	3.6491	174.85

Al_2O_3 30 PPI 75% porosity	0.0496	27.41
	0.4962	71.97
	2.4810	190.98
	4.9619	230.92
	7.4429	466.08
Al_2O_3 30 PPI 80% porosity	0.0501	25.21
	0.5010	56.05
	2.5048	240.48
	5.0098	376.39
	7.5146	483.73
Al_2O_3 30 PPI 85% porosity	0.0433	32.39
	0.4329	85.34
	2.1642	217.34
	4.3286	257.26
	6.4928	460.86
Al_2O_3 45 PPI 80% porosity	0.0649	27.56
	0.6493	85.58
	3.2463	244.44
	6.4925	370.67
	9.7387	509.56

Table 8.4: Superficial velocities for a fluid of Pr = 2 and the corresponding heat transfer coefficient values of the sponge structures.

Structure name	$\mathbf{u_s \times 10^{-3}}$ **[m/s]**	**Heat transfer coefficient** $\mathbf{[W/m^2K]}$
Al_2O_3 10 PPI 80% porosity	0.40	433.79
	4.00	1194.05
	20.02	2282.03
	40.03	3027.26
	60.05	5860.20

SiSiC 10 PPI 85% porosity	0.42	278.88
	4.21	1013.33
	21.06	2487.53
	42.12	3879.97
	63.17	5252.72
Al_2O_3 20 PPI 75% porosity	0.83	667.01
	8.26	2213.26
	41.28	4917.62
	82.56	7635.16
	123.84	9868.63
Al_2O_3 20 PPI 80% porosity	0.74	556.76
	7.44	1651.66
	37.18	3881.17
	74.36	8155.72
	111.53	10523.90
Al_2O_3 20 PPI 85% porosity	0.80	754.01
	8.03	1934.86
	40.14	4295.47
	80.29	6513.20
	120.44	10591.11
SiSiC 20 PPI 85% porosity	0.52	488.50
	5.23	1274.89
	26.14	3014.50
	52.29	5461.18
	78.43	6956.50
Al_2O_3 30 PPI 75% porosity	1.07	796.57
	10.66	1921.86
	53.32	4991.61
	106.65	12935.07
	159.97	15821.44
Al_2O_3 30 PPI 80% porosity	1.08	985.24
	10.77	2712.59
	53.84	5698.78
	107.68	9388.62
	161.51	10579.92

Al_2O_3 30 PPI 85% porosity	0.93	917.80
	9.30	2204.46
	46.52	4380.25
	93.03	7526.26
	139.55	10788.62
Al_2O_3 45 PPI 80% porosity	1.40	1009.08
	13.96	2862.98
	69.77	7677.98
	139.54	9312.47
	209.31	14432.48

Table 8.5: Superficial velocities for a fluid of Pr = 6 and the corresponding heat transfer coefficient values of the sponge structures.

Structure name	$\mathbf{u_s \times 10^{-3}}$ **[m/s]**	**Heat transfer coefficient** $\mathbf{[W/m^2K]}$
Al_2O_3 10 PPI 80% porosity	1.07	458.98
	10.76	1227.77
	53.80	3036.29
	107.60	4594.91
	161.39	6283.98
SiSiC 10 PPI 85% porosity	1.13	341.26
	11.32	941.38
	56.60	2849.23
	113.19	4397.04
	169.79	5657.96
Al_2O_3 20 PPI 75% porosity	2.22	921.44
	22.19	2665.55
	110.94	5806.76
	221.89	10948.47
	332.84	14467.74

Al_2O_3 20 PPI 80% porosity	2.00	636.63
	19.99	1828.61
	99.92	5219.16
	199.84	7981.15
	299.76	8863.51
Al_2O_3 20 PPI 85% porosity	2.16	829.59
	21.58	2155.42
	107.90	5775.61
	215.79	8199.15
	323.69	11635.19
SiSiC 20 PPI 85% porosity	1.40	380.59
	14.05	1361.26
	70.26	3905.05
	140.53	4946.23
	210.79	5683.76
Al_2O_3 30 PPI 75% porosity	2.87	1014.65
	28.66	2659.18
	143.32	8017.54
	286.63	13716.49
	429.95	15289.51
Al_2O_3 30 PPI 80% porosity	2.90	947.45
	28.94	3053.08
	144.70	7811.51
	289.40	11310.23
	434.09	14259.38
Al_2O_3 30 PPI 85% porosity	2.50	892.23
	25.01	2401.57
	125.02	6737.88
	250.05	10129.93
	375.07	12618.77
Al_2O_3 45 PPI 80% porosity	3.75	1188.01
	37.51	3698.52
	187.53	10246.65
	375.05	12115.95
	562.57	19422.89

Bibliography

[1] S. Abanades and H. I. Villafan-Vidales. CO_2 and H_2O conversion to solar fuels via two-step solar thermochemical looping using iron oxide redox pair. *Chem Eng J*, 175:368–375, 2011.

[2] A. Amiri and K. Vafai. Analysis of dispersion effects and non-thermal equilibrium, non-darcian, variable porosity incompressible flow through porous media. *International Journal of Heat and Mass Transfer*, 37:939–954, 1994.

[3] A. Amiri and K. Vafai. Transient analysis of incompressible flow through a packed bed. *International Journal of Heat and Mass Transfer*, 41:4259–4279, 1998.

[4] C. Argento and D. Bouvard. A ray tracing method for evaluating the radiative heat transfer in porous media. *Int J Heat Mass Transf*, 39:3175–3180, 1996.

[5] R. Aris and N. R. Amundson. Some remarks on longitudinal mixing or diffusion in fixed beds. *AIChE J*, 3:280–282, 1957.

[6] D. Baillis, M. Arduini-Schuster, and J. Sacadura. Identification of spectral radiative properties of polyurethane foam from hemispherical and bi-directional transmittance and reflectance measurements. *J Quant Spectrosc Radiat Transf*, 73:297–306, 2002.

[7] D. Baillis, M. Raynaud, and J. Sacadura. Spectral radiative properties of open-cell foam insulation. *J Thermophys Heat Transfer*, 13:292–298, 1999.

[8] D. Baillis and J. F. Sacadura. Thermal radiation properties of dispersed media: theoretical prediction and experimental characterization. *J Quant Spectrosc Radiat Transf*, 67:327–363, 2000.

[9] J. Bear. *Dynamics of Fluids in Porous Media*. Dover Publications, Inc., New York, 1988.

[10] G.S. Beavers, E.M. Sparrow, and D.E. Rodenz. Influence of bed size on the flow characteristics and porosity of randomly packed beds of spheres. *J. Appl. Mech.*, 40:655–660, 1973.

[11] A. Bhattacharya, V. V. Calmidi, and R. L. Mahajan. The effective thermal conductivity of high porosity fibrous metal foams. *Int. J. Heat Mass Transf.*, 45:1017–1031, 2002.

[12] R. Bird. *Transport phenomena*. J. Wiley, New York, 2002.

[13] F. C. Blake. The resistance of packing to fluid flow. *Amer. Inst. Chem. Engrs.*, 14:415–421, 1922.

[14] K. K. Bodla, J. Y. Murthy, and S. V. Garimella. Resistance network-based thermal conductivity model for metal foams. *Computational Materials Science*, 50:622–632, 2010.

[15] K. Boomsma and D. Poulikakos. On the effective thermal conductivity of a three-dimensionally structured fluid-saturated metal foam. *International Journal of Heat and Mass Transfer*, 44:827–836, 1999.

[16] J. P. Boon, E. V. Eijnden, and D. Hanon. A lattice gas automaton approach to 'turbulent diffusion'. *Chaos Solitons Fractals*, 11:187–192, 2000.

[17] Oliver Brunn. *Modellierung des dreidimensionalen Strahlungswärmeaustauschs in Verbrennungsräumen mittels Monte-Carlo-Methode*. KIT Scientific Publ, Karlsruhe, 2010.

[18] S. P. Burke and W. B. Plummer. Gas flow through packed columns. *Ind. Eng. Chem.*, 20:1196–1200, 1928.

[19] V. V. Calmidi and R. L. Mahajan. The effective thermal conductivity of high porosity fibrous metal foams. *J. Heat Transf.*, 121:466–471, 1999.

[20] V. V. Calmidi and R. L. Mahajan. Forced convection in high porosity metal foams. *Journal of Heat Transfer*, 122:557–565, 2000.

[21] R. G. Carbonell and S. Whitaker. Dispersion in pulsed systems-ii. theoretical delvelopments for passive dispersion in porous media. *Chemical engineering science*, 38:1795–1802, 1983.

[22] P. C. Carman. Fluid flow through granular beds. *Transactions of the Institution of Chemical Engineers*, 15:150–166, 1937.

[23] J. C. Chen and S. W. Churchill. Radiant heat transfer in packed beds. *AIChE J*, 9:35–41, 1962.

[24] W. C. Chueh, C. Falter, M. Abbott, D. Scipio, P. Furler, S. M. Haile, and A. Steinfeld. High-flux solar-driven thermochemical dissociation of CO_2 and H_2O using nonstoichiometric ceria. *Sceince*, 330:1797–1801, 2010.

[25] H. Darcy. *Les Fontaines Publiques de la ville de Dijon.* Dalmont, Paris, 1856.

[26] J. M. P. Q. Delgado. A critical review of dispersion in packed beds. *Heat Mass Transfer*, 42:279–310, 2006.

[27] J. M. P. Q. Delgado. Longitudinal and transversal dispersion in porous media. *Trans IChemE Part A, Chemical Engineering Research and Design*, 85:1245–1252, 2007.

[28] B. Dietrich. Pressure drop correlation for ceramic and metal sponges. *Chem. Eng. Sci.*, 74:192–199, 2012.

[29] B. Dietrich, W. Schabel, M Kind, and H. Martin. Pressure drop measurements of ceramic sponges-determining the hydraulic diameter. *Chem. Eng. Sci.*, 64:3633–3640, 2009.

[30] B. Dietrich, G. Schell, E. C. Bucharsky, R. Oberacker, M. J. Hoffmann, W. Schabel, M. Kind, and H. Martin. Determination of the thermal properties of ceramic sponges. *Int. J. Heat Mass Transf.*, 53:198–205, 2010.

[31] Benjamin Dietrich. *Thermische Charakterisierung von keramischen Schwammstrukturen für verfahrenstechnische Apparate*. KIT Scientific Publishing, Karlsruhe, 2010.

[32] N. Djordjevic, P. Habisreuther, and N. Zarzalis. Porous burner for application in stationary gas turbines: An experimental investigation of the flame stability, emissions and temperature boundary condition. *Flow Turbul. Combust.*, 89:261–274, 2012.

[33] J. P. Du Plessis. Analytical quantification of coefficients in the ergun equation for fluid friction in a packed bed. *Transport in Porous Media*, 16:1189–207, 1994.

[34] J. P. Du Plessis and S. Woudberg. Pore-scale derivation of the ergun equation to enhance its adaptability and generalization. *Chem. Eng. Sci.*, 63:2576–2586, 2008.

[35] N. Dukhan and P. Patel. Equivalent particle diameter and length scale for pressure drop in porous metals. *Experimental Thermal and Fluid Science*, 32:1059–1067, 2008.

[36] F. A. L. Dullien. *Porous media : fluid transport and pore structure*. Academic Press, San Diego, 1992.

[37] D. Edouard. The effective thermal conductivity for “slim”and “fat”foams. *AIChE J.*, 57:1646–1651, 2011.

[38] D. Edouard, M. Lacroix, C. P. Huu, and F. Luck. Pressure drop modeling on solid foam: State-of-the art correlation. *Chemical Engineering Journal*, 144:299–311, 2008.

[39] M. F. Edwards and J. F. Richardson. Gas dispersion in packed beds. *Chem Eng Sci*, 23:109–123, 1968.

[40] S. Ergun. Fluid flow through packed column. *Chem. Eng. Prog.*, 48:89–94, 1952.

[41] E. V. Evans and C. N. Kenny. Gaseous dispersion in packed beds at low reynolds numbers. *Trans Instn chem Engrs*, 44:T189–T197, 1966.

[42] T. Fend, B. Hoffschmidt, R. Pitz-Paal, O. Reutter, and P. Rietbrock. Porous materials as open volumetric solar receivers: Experimental determination of thermophysical and heat transfer properties. *Energy*, 29:823–833, 2004.

[43] X. Fu, R. Viskanta, and J. P. Gore. Prediction of effective thermal conductivity of cellular ceramics. *International Communications in Heat and Mass Transfer*, 25:151–160, 1998.

[44] P. Furler, J. Scheffe, M. Gorbar, L. Moes, U. Vogt, and A. Steinfeld. Solar thermochemical CO_2 splitting utilizing a reticulated porous ceria redox system. *Energy & Fuels*, 26:7051–7059, 2012.

[45] P. Furler, J. Scheffe, and A. Steinfeld. Syngas production by simultaneous splitting of H_2O and CO_2 via ceria redox reactions in a high-temperature solar reactor. *Energy & Environmental Science*, 5:6098–6103, 2012.

[46] Philipp Furler. *Solar thermochemical CO_2 and H_2O splitting via ceria redox reactions.* Diss., Eidgenössische Technische Hochschule ETH Zürich.

[47] G. I. Garrido, F. C. Patcas, S. Lang, and B. Kraushaar-Czarnetzki. Mass transfer and pressure drop in ceramic foams: A description for different pore sizes and porosities. *Chemical Engineering Science*, 63:5202–5217, 2008.

[48] Gerardo Garrido. *Mass and momentum transfer upon flow through solid sponges.* Universitätsverlag, Karlsruhe, 2009.

[49] R. Goedecke. *Fluidverfahrenstechnik Grundlagen, Methodik, Technik, Praxis*, volume 1. Wiley-VCH, Weinheim, Bergstr, 2011.

[50] J. Grosse, B. Dietrich, G. I. Garrido, P. Habisreuther, N. Zarzalis, H. Martin, M. Kind, and B. Kraushaar-Czarnetzki. Morphological characterization of ceramic sponges for applications in chemical engineering. *Ind. Eng. Chem. Res.*, 48:10395–10401, 2009.

[51] J. Grosse, B. Dietrich, H. Martin, M. Kind, J. Vicente, and E. H. Hardy. Volume image analysis of ceramic sponges. *Chem. Eng. Technol.*, 31:307–314, 2008.

[52] P. Habisreuther, N. Djordjevic, and N. Zarzalis. Statistical distribution of residence time and tortuosity of flow through open-cell foams. *Chemical Engineering Science*, 64:4943–4954, 2009.

[53] C. L. Hackert, J. L. Ellzey, and O. A. Ezekoye. Combustion and heat transfer in model two-dimensional porous burners. *Combustion and Flame*, 116:177–191, 1999.

[54] C. L. Hackert, J. L. Ellzey, O. A. Ezekoye, and M. J. Hall. Transverse dispersion at high peclet numbers in short porous media. *Experiments in Fluids*, 21:286–290, 1996.

[55] N. Han, J. Bhakta, and R. G. Carbonell. Longitudinal and lateral dispersion in packed beds: effect of column length and particle size distribution. *AIChE J*, 31:277–288, 1985.

[56] J. Happel and H. Brenner. *Low Reynolds Number Hydrodynamics*. Martinus Nijhoff Publishers, 1986.

[57] T. J. Hendricks and J. R. Howell. Absorption scattering coefficients and scattering phase functions in reticulated porous ceramics. *ASME Journal of heat transfer*, 118:79–87, 1996.

[58] T. J. Hendricks and J. R. Howell. New radiative analysis approach for reticulated porous ceramics using discrete ordinates method. *ASME Journal of heat transfer*, 118:911–917, 1996.

[59] J. W. Hiby. Longitudinal dispersion in single-phase liquid flow through ordered and random packings. *Interaction between Fluids and Particles, London Instn Chem Engrs*, pages 312–325, 1962.

[60] W. H. Hsieh, J. Y. Wu, W. H. Shih, and W. C. Chiu. Experimental investigation of heattransfer characteristics of aluminum-foam heat sinks. *Int. J. Heat Mass Transfer*, 47:5149–5157, 2004.

[61] C. T. Hsu, P. Cheng, and K. W. Wong. A lumped parameter model for stagnant thermal conductivity of spatially periodic

porous media. *ASME Transac.: J. Heat Transf.*, 117:264–269, 1995.

[62] J. M. Hugo. Heat transfer in cellular porous medium at high porosity: Application to structural optimization of fin exchangers. *PhD Thesis, Aix-Marseille University*, 2012.

[63] C. Hutter, A. Zenklusen, R. Lang, and Ph.Rudolf von Rohr. Axial dispersion in metal foams and streamwise-periodic porous media. *Chemical Engineering Science*, 66:1132–1141, 2011.

[64] J. J. Hwang, G. J. Hwang, R. H. Yeh, and C. H. Chao. Measurement of interstitial convective heat transfer and frictional drag for flow across metal foams. *Journal of Heat Transfer*, 124:120–129, 2001.

[65] A. Inayat, J. Schwerdtfeger, H. Freund, C. Körner, R. F. Singer, and W. Schwieger. Periodic open-cellfoams:pressure drop measurements and modeling of an ideal tetrakaidecahedra packing. *Chemical Engineering Science*, 66:2758–2763, 2011.

[66] D. B. Ingham. *Transport phenomena in porous media II.* Pergamon, Amsterdam New York, 2002.

[67] Ichimiya K. A new method for evaluation of heat transfer between solid material and fluid in a porous medium. *ASME J. Heat Transfer*, 121:978–983, 1999.

[68] M. Kaviany. *Principles of Heat Transfer in Porous Media.* Springer-Verlag, New York, second edition, 1995.

[69] D. L. Koch and J. F. Brady. Dispersion in fixed beds. *Journal of fluid mechanics*, 154:399–427, 1985.

[70] O. Krischer. *Die wissenschaftlichen Grundlagen der Trocknungstechnik (The Scientific Fundamentals of Drying Technology).* Springer-Verlag, New York, 1963.

[71] O. Krischer and W. Kast. *Die wissenschaftlichen Grundlagen der Trocknungstechnik.* Springer-Verlag, Berlin, 1978.

[72] S. Krishnan, S. Garimella, and J. Y. Murthy. Simulation of thermal transport in opencell metal foams: effects of periodic unit-cell structure. *J. Heat Transf.*, 130:409–414, 2008.

[73] P. Kumar and F. Topin. Simultaneous determination of intrinsic solid phase conductivity and effective thermal conductivity of kelvin like foams. *Applied Thermal Engineering*, 71:536–547, 2014.

[74] M. Lacroix, P. Nguyen, D. Schweich, C. P. Huu, S. Savin-Poncet, and D. Edouard. Pressure drop measurements and modeling on sic foams. *Chemical Engineering Science*, 62:3259–3267, 2007.

[75] R. Landauer. The electrical resistance of binary metallic mixtures. *J. Appl. Phys.*, 23:779–784, 1952.

[76] B. K. Larkin and S. W. Churchill. Heat transfer by radiation through porous insulations. *AIChE J*, 5:467–474, 1959.

[77] K. C. Leong and L. W. Jin. An experimental study of heat transfer in oscillating flow through a channel filled with an aluminum foam. *Int. J. Heat Mass Transfer*, 48:243–253, 2005.

[78] A. Lévêque. Les lois de la transmission de chaleur par convection. *CAnales des Mines*, 13:201–299, 305–362, 381–415, 1928.

[79] J. F. Liu, W. T. Wu, W. C. Chiu, and W. H. Hsieh. Measurement and correlation of friction characteristic of flow through foam matrixes. *Experimental Thermal and fluid Science*, 30:329–336, 2006.

[80] S. Lorentzou, G. Karagiannakis, C. Pagkoura, A. Zygogianni, and A. G. Konstandopoulos. Thermochemical CO_2 and CO_2/H_2O splitting over $NiFe_2O_4$ for solar fuels synthesis. *Energy Procedia*, 49:1999–2008, 2014.

[81] P. G. Loutzenhiser and A. Steinfeld. Solar syngas production from CO_2 and H_2O in a two-step thermochemical cycle via Zn/ZnO redox reactions: thermodynamic cycle analysis. *Int J Hydrogen Energy*, 36:12141–12147, 2011.

[82] W. Lu, C. Y. Zhao, and S. A. Tassou. Thermal analysis on metal-foam filled heat exchangers. Part I: Metal-foam filled pipes. *Int. J. Heat Mass Transfer*, 49:2762–2770, 2006.

[83] I. F. Macdonald, M. S. El-Sayed, K. Mow, and F. A. L. Dullien. Flow through porous media-ergun equation revisited. *Ind. Eng. Chem. Fund.*, 18:199–208, 1979.

[84] R. S. Maier, D. M. Kroll, R. S. Bernard, S. E. Howington, J. F. Peters, and H. T. Davis. Enhanced dispersion in cylindrical packed beds. *Philos Trans R Soc Lond A*, 360:497–506, 2002.

[85] E. Maire, P. Colombo, J. Adrien, L. Babout, and L. Biasetto. Characterization of the morphology of cellular ceramics by 3d image processing of x-ray tomography. *Journal of the European Ceramic Society*, 27:1973–1981, 2007.

[86] H. Martin. The generalized lévêque equation and its practical use for the prediction of heat and mass transfer rates from pressure drop. *Chemical Engineering Science*, 57:3217–3223, 2002.

[87] J. C. Maxwell. *A treatise on electricity and magnetism.* Dover Publications, New York, 1954.

[88] W. J. Minkowycz, A. Haji-Sheikh, and K. Vafai. On departure from local thermal equilibrium in porous media due to a rapidly changing heat source: the sparrow number. *International Journal of Heat and Mass Transfer*, 42:3373–3385, 1999.

[89] M. Modest. *Radiative Heat Transfer.* Academic Press, San Diego, second edition, 2003.

[90] E. A. Moreira and J. R. Coury. The influence of structural parameters on the permeability of ceramic foams. *Brazilian Journal of Chemical Engineering*, 21:23–33, 2004.

[91] E. A. Moreira, M. D. M. Innocentini, and J. R. Coury. Permeability of ceramic foams to compressible and incompressible flow. *Journal of the European Ceramic Society*, 24:3209–3218, 2004.

[92] Donald A. Nield and Adrian Bejan. *Convection in Porous Media.* Springer, third edition, 2006.

[93] M. Özişik. *Heat conduction.* Wiley, New York, 1993.

[94] J. C. F. Pereira, I. Malico, T. C. Hayashi, and J. Raposo. Experimental and numerical characterisation of transverse dispersion at the exit of a short ceramic foam inside a pipe. *Int. J. Heat Mass Transfer*, 48:1–14, 2005.

[95] T. K. Perkins and O. C. Johnston. A review of diffusion and dispersion in porous media. *Society of Petroleum Engineers Journal*, 3:70–84, 1963.

[96] J. Petrasch, P. Wyss, and A. Steinfeld. Tomography-based monte carlo determination of radiative properties of reticulate porous ceramics. *J Quant Spectrosc Radiat Transf*, 105:180–197, 2007.

[97] J. M. Prausnitz. Longitudinal dispersion in a pecked bed. *AIChE J*, 4:14M–22M, 1958.

[98] P. Quadbeck, K. Kümmel, R. Hauser, G. Standke, J. Adler, and G. Stephani. Open cell metal foams-application-oriented structure and material selection. *in:Proceeding Cell Mat*, pages 238–279, 2010.

[99] A. Reitzmann, F. C. Patcas, and B. Kraushaar-Czarnetzki. Keramische schwämme-anwendungspotential monolithischer netzstrukturen als katalytische packungen. *Chemie Ingenieur Technik*, 78:885–898, 2006.

[100] J. T. Richardson, Y. Peng, and D. Remue. Properties of ceramic foam catalyst supports: pressure drop. *Applied Catalysis A: General*, 204:19–32, 2000.

[101] J. T. Richardson, D. Remue, and J. K. Hung. Properties of ceramic foam catalyst supports: mass and heat transfer. *Applied Catalysis A: General*, 250:319–329, 2003.

[102] J. Sacadura and D. Baillis. Experimental characterization of thermal radiation properties of disperse media. *Int J Therm Sci*, 41:699–707, 2002.

[103] M. Sahraoui and M. Kaviany. Slip and no-slip velocity boundary conditions at interface of porous, plain media. *Int. J. Heat Mass Transfer.*, 35:927–943, 1992.

[104] T. Saito and i J. Toriwak. New algorithms for euclidean distance transformation of an n-dimensional digitized picture with applications. *Pattern Recognition*, 27:1551–1565, 1994.

[105] M. Scheffler. *Cellular ceramics structure, manufacturing, properties and applications*. Wiley-VCH John Wiley distributor, Weinheim Chichester, 2005.

[106] L. Schiller and Z. Naumann. A drag coefficient correlation. *Ver. Deutsch. Ing.*, 77:318–320, 1935.

[107] B. V. Setten, J. Bremmer, S. Jelles, M. Makkee, and J. Moulijn. Ceramic foam as a potential molten salt oxidation catalyst support in the removal of soot from diesel exhaust gas. *Catalysis today*, 53:613–621, 1999.

[108] R. Siegel and J. R. Howell. *Thermal Radiation Heat Transfer*. Taylor and Francis, New York, third edition, 1992.

[109] M. Tancrez and J. Taine. Direct identification of absorption and scattering coefficients and phase function of a porous medium by a monte carlo technique. *Int J Heat Mass Transf*, 47:373–383, 2004.

[110] G. Taylor. Dispersion of soluble matter in solvent flowing slowly through a tube. *Proceedings of the Royal Society A*, 219:186–203, 1953.

[111] S. C. Tzeng. Spatial thermal regulation of aluminum foam heat sink using a sintered porous conductive pipe. *Int. J. Heat Mass Transfer*, 50:117–126, 2007.

[112] S. C. Tzeng and T. M. Jeng. Convective heat transfer in porous channels with 90-deg turned flow. *Int. J. Heat Mass Transfer*, 49:1452–1461, 2006.

[113] K. Vafai. *Handbook of porous media*. Taylor & Francis, Boca Raton, 2005.

[114] J. Vicente, F. Topin, and J. V. Daurelle. Open celled material structural properties measurement: From morphology to transport properties. *Materials Transactions*, 47:2195–2202, 2006.

[115] J. Vicente, F. Topin, J. V. Daurelle, and F. Rigollet. Thermal conductivity of metallic foam: simulation on real x-ray tomographied porous medium and photothermal experiments. *in: Proceedings of IHTC 13, Sydney*, 2010.

[116] N. Wakao and S. Noriaki. *Heat and mass transfer in packed beds.* Gordon and Breach Science Publishers, New York, 1982.

[117] J. C. Ward. Turbulent flow in porous media. *J. Hyd. Div. ASCE*, 90:1–12, 1964.

[118] S. Whitaker. *Fundamental principles of heat transfer.* R.E. Krieger Pub. Co, Malabar, 1983.

[119] S. Whitaker. The forchheimer equation: A theoretical development. *Transport in Porous Media*, 25:27–61, 1996.

[120] Y. S. Yang, J. R. Howell, and D. E. Klein. Radiative heat transfer through a randomly packed bed of spheres by the monte carlo method. *ASME Journal of heat transfer*, 105:325–332, 1983.

[121] L. B. Younis and R Viskanta. Experimental determination of the volumetric heat transfer coefficient between stream of air and ceramic foam. *International Journal of Heat and Mass Transfer*, 36:1425–1434, 1993.

[122] C. Zhao, T. Lu, and H. Hodson. Thermal radiation in ultralight metal foams with open cells. *Int J Heat Transfer*, 47:2927–2939, 2002.

[123] A. A. Zukauskas. *Convective heat transfer in cross-flow, in: S. Kakac, R.K. Shah, W. Aung (Eds.), Handbook of Single-Phase Convective Heat Transfer.* Wiley, New York, 1987.